PROCESSING AND SYNTHESIS OF MULTI-METALLIC NANO OXIDE CERAMICS VIA LIQUID-FEED FLAME SPRAY PYROLYSIS

by

José Antonio Azurdia

A dissertation submitted in partial fulfillment
of the requirements for the degree of
Doctor of Philosophy
(Materials Science and Engineering)
in The University of Michigan
2009

Doctoral Committee:

Professor Richard M. Laine, Chair
Professor John W. Halloran
Professor Stephen C. Rand
Associate Research Scientist John F. Mansfield

DEDICATION

Dedicated to my mother and all the friends who have made this part of my journey a most exciting one.

ACKNOWLEDGMENTS

First and foremost I must thank Richard Laine for bringing me into his research group early on as an undergraduate. His confidence, guidance and patience during my graduate years have allowed me to complete this degree. My committee members; John Halloran, Stephen Rand and John Mansfield deserve special thanks for taking on the task of serving on this dissertation committee.

I could not have done this work without the support of my mother, friends here and in Guatemala and fellow graduate students. In particular I would like to express gratitude to the members of the Fafnir team: Dr. Tom Hinklin, Dr. Julien Marchal and Dr. Min Kim who not only worked with me on these experiments but taught me a great deal of what I know. I would also like to thank current and past Laine group members; Dr. Jiwon Choi, Dr. Chad Brick, Mike Asuncion, Mark Roll, and especially Santy Sulaiman.

Stevi's unconditional love and support have given me the courage and inspiration to bring this part of my journey to completion, for this I will always be thankful.

Along the way I have made friends and coworkers, met with collaborators and colleagues that have helped shape my personal and professional life, to those too numerous individuals to name independently I sincerely thank each and every one of you from the bottom of my heart.

TABLE OF CONTENTS

LIST OF FIGURES

LIST OF TABLES

ABSTRACT

PROCESSING AND SYNTHESIS OF MULTI-METALLIC NANO OXIDE CERAMICS VIA LIQUID-FEED FLAME SPRAY PYROLYSIS

by

José Antonio Azurdia

Chair: Richard M. Laine

The liquid-feed flame spray pyrolysis (LF-FSP) process aerosolizes metal-carboxylate precursors dissolved in alcohol with oxygen and combusts them at >1500 °C. The products are quenched rapidly (~10s msec) to < 400 °C. By selecting the appropriate precursor mixtures, the compositions of the resulting oxide nanopowders can be tailored easily, which lends itself to combinatorial studies of systems facilitating material property optimization. The resulting nanopowders typically consist of single crystal particles with average particle sizes (APS) < 35 nm, specific surface areas (SSA) of 20–60 m^2/g and spherical morphology.

LF-FSP provides access to novel single phase nanopowders, known phases at compositions outside their published phase diagrams, intimate mixing at nanometer length scales in multi metallic oxide nanopowders, and control of stoichiometry to ppm levels.

The materials produced may exhibit unusual properties including structural, catalytic, and photonic ones and lower sintering temperatures. Prior studies used LF-FSP to produce $MgAl_2O_4$ spinel for applications in transparent armor and IR radomes. In these studies, a stable spinel structure with a $(MgO)_{0.1}(Al_2O_3)_{0.9}$ composition well outside the known phase field was observed. The work reported here extends this observation to two other spinel systems: Al_2O_3-NiO, Al_2O_3-CoOx; followed by three series of transition metal binary oxides, NiO-CoO, NiO-MoO_3, NiO-CuO. The impetus to study spinels derives both from the fact that a number of them are known transparent ceramics, but also others offer high SSAs coupled with unusual phases that suggest potentially novel catalytic materials.

Because LF-FSP provides access to any composition, comprehensive studies of the entire tie-lines were conducted rather than just compositions of value for catalytic applications. Initial efforts established baseline properties for the nano aluminate spinels, then three binary transition metal oxide sets (Ni-Co, Ni-Mo and Ni-Cu) known for their catalytic properties. These materials then serve as baseline studies for ternary systems, such as Al:(Ni-Co)O, or Al(Ni-Cu)O likely to offer superior catalytic properties because of the relatively high SSA Al_2O_3.

The final chapter returns to photonic materials, in the MgO-Y_2O_3 system targeting transparent ceramics through select compositions along the tie-line. The work presented here builds on the $MgAl_2O_4$ spinel material and continues to develop the processing techniques required to achieve transparent nano-grained ceramic materials. Thus the overall goal of this dissertation was to systematically produce novel nano-oxide materials and characterized their material properties.

The first chapters focus on solid solutions at low Ni or Co amounts that form phase pure spinels outside the expected composition range, at 21-22 mol % NiO and CoO. Additionally, $(NiO)_{0.22}(Al_2O_3)_{0.78}$ was found to be very stable, as it did not convert to α-Al_2O_3 plus cubic-NiO on heating to 1200 °C for 10 h.

The last chapter is a preliminary step toward identifying optimal Y_2O_3-MgO powders that can be transparent ceramics. Ball milling led to much higher adsorption of surface species. Preliminary sintering studies of this system showed that vacuum has the largest effect on lowering the temperature of maximum shrinkage rate by $\leq$ 80 °C.

Chapter 1.

Introduction

The development of high-purity, nanograined ceramics is critical to advancement of many leading technologies which include gas sensors,[1] medical implants,[2] catalytic materials,[3] high powered lasers,[4,5] pigments,[6] phosphors,[7] transparent windows[8,9] and IR radomes[10,11] lighting[12] and ballistic armor.[13,14] Specifically, nanograined ceramics would provide higher strength, hardness, toughness and transparency not readily obtainable in more traditional fine-grained ceramics. These improvements in properties of ceramic materials are very desirable because they allow us meet more demanding performance requirements, such as reductions in weight, or higher efficiency lasers and lights. These improvements may also lead to yet undiscovered uses in current applications. Undoubtedly, the prerequisite for achieving such nanograined ceramics is the development and optimal processing of nano-sized powders.

The main challenges to achieving nanograined ceramics (< 100 nm), are the access to homogenous, high purity (< 25 ppm impurities) nanopowders and sintering with uniform and slow grain growth during densification. The nanopowder material challenges have been addresed by careful selection of starting material and optimization of synthesis methods. The processing challenge can be address through proper control of green body formation and precise heating schedules.

The following sections will discuss general ceramic nanopowder synthesis routes and an overview of particle evolution in the gas phase. Nanopowder processing will follow

with a brief discussion on compaction, and a section on nanopowder sintering. We will conclude with a review of the spinel crystal structure and the overall scope of this dissertation.

1.1. Ceramic Nanopowders Synthesis

Over the past 20 years, the number of methods for synthesis of ceramic nanopowders has increased dramatically.[15] Initially these methods were gas-fed combustion of metal chlorides ($TiCl_4$),[16] or solution precipitation techniques, such as co-precipitation and sol-gel.[17] The main drawback to most precipitation technique is that the products must be calcined to generate the desired oxide.[18] The conventional synthesis for multi-component ceramic powders is solid-state reaction between oxide and/or carbonate, but this method typically produces larger (> 1μm) sized particles.[19] Liquid precursor aerosol routes are hybrid synthesis methods that provide definite advantages over gas techniques, particularly homogeneity in mixed metal chemical compositions, higher production yields and no noxious byproducts are generated.[20] All of these synthesis methods have been reviewed extensively.[21-26]

The flexibility to produce nanopowders with chemical and phase uniformity over a range of compositions is of particular interest, because it enables tailoring of material properties. Liquid-feed flame spray pyrolysis (LF-FSP) is a hybrid synthesis method that combines the high purity advantages of aerosol routes and the higher yields, better stoichiometry control found in solution methods. LF-FSP offers the potential to make a wide variety of single and mixed-metal oxide nanopowders in a single step.[27-36] In LF-FSP, alcohol solutions of dissolved metalloorganic precursors are aerosolized with oxygen and combusted within a quartz chamber at temperatures

≥ 1500 °C. The combustion products are rapidly quenched producing the oxide nanoparticles, which are the collected in electrostatic precipitators or a commercial bag-house. A more detailed description of the LF-FSP apparatus and process are found in Chapter 2.

1.1.1. Gas Phase Evolution of Ceramic Particles

The exact science of determining ceramic particle evolution in flames still remains controversial.[37] Recently Beaucage et.al. report *in-situ* measurements of nanoparticle evolution in laminar flames.[38] They use synchrotron X-ray scattering, to probe the formation of nano SiO_2 from combustion of organometallic $O[Si(CH_3)_3]_2$ in an oxygen/methane diffusion flame. Their direct observation of particle evolution in flames is very important because they suggest that the currently accepted theories of vapor phase particle formation are applicable to flame synthesis.

Extensive experimental and theoretical studies on vapor phase particle formation, show that once nucleation occurs, from oxo ions, there are three characteristic times that determine the final primary particle size and the degree of agglomeration/aggregation.[39-44] Pratsinis[45] and Woolridge[46] review particle nucleation in the gas phase, they conclude that it follows this sequence of events: vapors react forming oxo ions that condense into intermediate/molecules and clusters that quickly grow to nanosize particles by coagulation. The characteristic times used to describe particle evolution once primary particle formation occurs are: (1) collision time, (2) coalescence time and (3) residence time (of particles, but agglomerate/aggregates may be present as discussed below). The times scales for all of characteristic times are typically in the sub-msec range.

Collision time is the average time between encounters of two particles at a given time or distance from flame front. The particle flux, or spatial concentration of oxide particles is the main variable that affects the collision time. The particle flux can be described as the number of particles that flow through an arbitrary unit area per unit time.

Coalescence time is defined as the time necessary for two individual particles to form a single larger one. Coalescence can occur through fusion if the particles remain in a viscous state, or through solid-state diffusion. This characteristic time is dependent on the diffusivity of the atoms present in the particles. Diffusion controls how fast mass transport occurs, therefore the time it takes to eliminate a boundary by lattice diffusion will affect this characteristic time. Diffusion rates are strong functions of temperature profiles and crystallographic defects such as vacancies and impurities. The formation of agglomerates is defined mathematically, when the coalescence and collision times are equal.[47,48] At this point, two single particles no longer come together to form a single larger particle but only undergo partial coalescence. Particles only "stick" to each other forming flocs or loosely branched chains of particles. These flocs are characterized by fractal geometry and may either form agglomerates (characterized by particles weakly connected by attractive forces), or aggregates (particles are joined by a grain boundary).

The residence time is the time that a given particle or floc spends along the axis of the flame or reactor, it is a function of flame velocity, and overall gas flow. The overall flow includes any supplementary or quench gasses that may be added to the reactor. A particle's residence time determines to a large extent the degree to which

aggregates or agglomerates will form and their sizes. Longer residence times expose flocs to higher temperatures that enable grain boundary formation leading to aggregates.

Once high quality un-aggregated homogeneous nanopowders have been produced the formation of a stable green body is required to produce a ceramic monolith. Green body formation plays an important role in the quality of the final ceramic.[49] Various green body formation techniques have been developed which include preparation of the powders, different colloidal processing and ultimately compaction.[50-52]

1.2. Sintering Nanopowders

The first step in effectively sintering nanopowders is in the control or rearrangement of fractal agglomerates. Various authors have stated that the greatest limiting step in achieving homogenous sub-micron ceramic particles is the presence of aggregates.[53-56] The formation of aggregates and agglomerates depends mainly on the residence time of the nanoparticles discussed above, therefore shorter residence times are required in order to limit the formation of aggregates.[57] The reason that aggregates are not desired is that they often have pores much larger than the primary particles, which are responsible for residual porosity in any resulting ceramic monolith. Further discussion on the importance of pore evolution follows.

Pore control during nanopowder processing is imperative to producing fully dense polycrystalline, nano grained ceramic monoliths. Three general types of pores are found during the processing of ceramic nanopowders; interstitial pores, aggregate pores, and pores formed at the interfaces of densification differences.[58-61] The first two pores types

are solely attributed to the nanopowders themselves. The third type of pore arises during the sintering process from local differences in the densification rates.

Interstitial pores are the void spaces between packed particles or agglomerates. These pores are introduced during green body formation. Additionally, pores specific to the manufacture of the green body technique may be present, (processing flaws) such as micron-sized bubbles in casting.[62,63] Aggregate pores are those that exist inside the fractal structure. These pores are much harder to remove because of their hard contact points (necks) from coalesced particles in the flame, as discussed above. Interfacial pores arise from local differences in densification rates during the sintering process. Densification rate differences arise from density gradients, impurities (dopants or intended second phases) and faster densification rates of already dense necks in aggregates.[64]

Broadly the sintering process can be described as consisting of three stages:[65]

(1) Initial Stage: Surface diffusion begins leading to primary particles forming necks at particle-particle contact points.

(2) Intermediate Stage: Most densification occurs during this stage, from microstructural rearrangements by lattice diffusion. These rearrangements result from continuous pore network formation as the grain size becomes homogenous, ideally the pore sizes also become homogenous. Decreasing the free energy of the system is what drives this rearrangement. The decrease in free energy is obtained by the elimination of solid-vapor interfaces, thus decreasing surface free energy and the forming new lower energy solid-solid interfaces. Towards the end of this stage, the average pore size tends to a stable one until pores become pinched.

(3) Final Stage: Coalescence of the pore network and individual pores occurs during this stage. Final densification and coarsening (grain growth) become important mechanisms at this point. These two competing mechanisms will determine to a great extent the final microstructure of the monolith.

The driving force for grain growth is the decrease in free energy by decreasing surface area with the increase the average radius of curvature of the grains. Thus small grains disappear at the expense of large growing ones.[66-68] Exaggerated grain growth may lead to pinning residual pores that are too large, thus too stable for densification to occur in them. Grain size control is therefore a very important aspect in achieving full density and has been studied extensively.[69-73] An effective way to control grain growth is to modify grain boundary mobilities by doping or forming solid solutions.[74,75] Chen. et. al showed that grain growth can effectively be controlled by keeping an open pore structure which hinders grain growth by decreasing grain boundary mobility.[76] Zhao and Harmer also describe similar results, in a set of sintering experiments of un-doped, MgO-doped, and ZrO_2-doped alumina; impregnated with model spherical pores produced by the burnt-out latex sphere method.[77]

The densification process for nanograined materials is not fundamentally different than for larger grained materials. In summary for the ideal case of sintering nanomaterials, the initial stage of sintering, the number of particle contacts increases necks forms occurs and total pore volume decreases. During the intermediate stage smooth continuous pores form and the bulk mass transfer occurs. The final stage, the formation of isolated closed spherical pores and grain coarsening generally occurs. In

nanograined ceramics any feature larger than the resultant grain size will result in a residual flaw, therefore care must be taken to minimize such occurrences.

Having discussed the formation and evolution of nanopowders and the major issues affecting the processing of nano grained ceramics, an overview of an important class of material is presented below.

1.3. Materials Review

In this dissertation we are interested in a number of materials for structural and catalytic applications, among them are spinel-structured materials. The LF-FSP process readily gives access any binary oxide composition that has the spinel structure. Spinels are of long standing interest because they exhibit valuable and/or unusual electronic, magnetic, catalytic, photonic, and structural properties.[78-83] These materials have been studied extensively particularly their crystal structures, phase equilibria and composition ranges, frequently to optimize specific properties.[84-86]

This dissertation reports in chapters 3 and 4 the use of liquid-feed flame spray pyrolysis (LF-FSP) to synthesize phase pure aluminate spinel nanopowders $(MO)_x(Al_2O_3)_{1-x}$ [M = Co, Ni] at compositions well outside the phase stability regions currently known for these materials. These hitherto undiscovered materials offer considerable potential for accessing entirely new catalytic properties with mixed-metal nanopowders that are thermally stable to 1200 °C. The next section describes the spinel crystal structure and its three variants: normal, inverse and intermediate. We discuss the characteristics of the isomorphs because in our studies of the $NiO\text{-}Al_2O_3$ system we unexpectedly observe an inverse spinel, at a composition that lies far beyond the

established phase boundary. Similarly in the CoO-Al_2O_3 system we find a phase pure spinel outside the published phase boundary.

1.3.1. Spinels

Spinels are a common structural arrangement shared by many transition metals oxides of the general formula ($A^{2+}B^{3+}{}_2O_4$). They all consist of a cubic close packed (face centered) sub-lattice of oxygen atoms with 1/8 of the tetrahedral sites and 1/2 of the octahedral sites occupied by the cations. These structures can be further divided into three types: normal, inverse and intermediate spinels.[87-88] The distinction between normal and inverse lies in which atoms occupy which positions.

In normal spinels, the tetrahedral (A sites) are occupied exclusively by divalent cations and octahedral (B sites) by trivalent cations. In an inverse spinel, half of the trivalent cations replace the divalent cations so that divalent cations now occupy octahedral sites giving rise to the formula $B^{3+}(A^{2+}B^{3+})O_4$. The intermediate spinels have partial normal and partial inverse character and are normally labeled in terms of the percent inverse character they exhibit.[89,90]

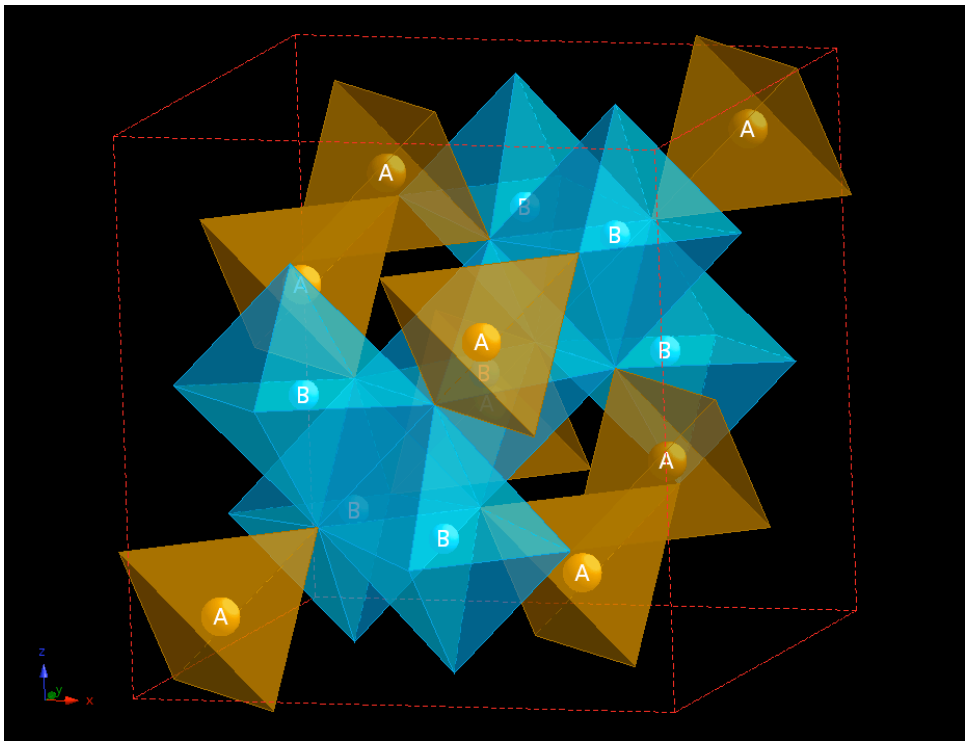

Figure 1-1. Normal spinel structure (oxygen lattice missing)

1.4. Scope of Dissertation

LF-FSP provides access to complex mixed-metal oxide materials including $Y_3A_5O_{12}$ and β"Al_2O_3, controlled mixed phase materials such as NiO-MoO_3, and materials with unusual phase compositions[91] and phases.[92]It is the overall goal of this dissertation to demonstrate the versatility of liquid-feed spray flame pyrolysis (LF-FSP) to produced mixed metal-oxide nanopowders with specific stoichiometries for structural, catalytic and optical ceramic materials. The wide variety of potential metal oxide precursors allows the synthesis of multiple chemical compositions, phase and unique particle morphologies in the resulting nanopowders.

The potential to rapidly explore any significant ceramic oxide material system is of great academic, scientific and technological importance, because it provides the possibility to discover entirely new materials' properties of mixed-metal oxides. This

dissertation will also discuss synthesis and characterization of six different binary oxide phase spaces. Some basic processing of these nanopowders into green bodies and their subsequent sintering into ceramic monoliths will be discussed as-well.

1.5. Bibliography

1. T. Wagner, T. Waitz, J. Roggenbuck, M. Fröba, C.-D. Kohl, M. Tiemann "Ordered Mesoporous ZnO for Gas Sensing," *Thin Solid Films,* 515 [23] 8360-8363 (2007).
2. M. E. Roy, L. A. Whiteside, B. J. Katerberg, J. A. Steiger "Phase Transformation, Roughness, and Microhardness of Artificially Aged Yttria- and Magnesia-stabilized Zirconia Femoral Heads," *J. Biomed. Mater. Res. A,* 83A [4] 1096-1102 (2007).
3. M. Richter, M. Langpape, S. Kolf, G. Grubert, R. Eckelt, J. Radnik, M. Schneider, M. M. Pohl, R. Fricke "Combinatorial Preparation and High-throughput Catalytic Tests of Multi-component deNO_x Catalysts," *Appl. Catal. B-Environ.,* 36 [4] 261-277 (2002).
4. S. Patterson, P. Leisher, K. Price, K. Kennedy, W. Dong, M. Grimshaw, S. Zhang, J. Patterson, S. Das, S. Karlsen, R. Martinsen, J. Bell "High-power Diode Lasers Operating Around 1500-nm for Eyesafe Applications," *Laser Source Technology for Defense and Security IV Laser Source Technology for Defense and Security IV Proc. SPIE,* 6952(1) [1] 69520W-695207 (2008).
5. D. C. Brown, J. M. Singley, E. Yager, J. W. Kuper, B. J. Lotito, L. L. Bennett "I - Innovative High-power Cw Yb:YAG Cryogenic Laser," *Laser Source Technology for Defense and Security III Laser Source Technology for Defense and Security III Proc. SPIE,* 6552(1) [1] 65520D-655209 (2007).
6. Z. Z. Chen, E. W. Shi, W. J. Li, Y. Q. Zheng, W. Z. Zhong "Hydrothermal Synthesis and Optical Property of Nano-sized $CoAl_2O_4$ Pigment," *Mater. Lett.,* 55 [5] 281-284 (2002).
7. Y. H. Zhou, J. Lin, M. Yu, S. M. Han, S. B. Wang, H. J. Zhang "Morphology Control and Luminescence Properties of YAG:Eu Phosphors Prepared by Spray Pyrolysis," *Mater. Res. Bull.,* 38 [8] 1289-1299 (2003).
8. R. Apetz, M. P. B. Bruggen "Transparent Alumina: A Light-scattering Model," *J. Am. Ceram. Soc.,* 86 [3] 480-486 (2003).
9. U. Peuchert, Y. Okano, Y. Menke, S. Reichel, A. Ikesue "Transparent Cubic-ZrO_2 Ceramics for Application as Optical Lenses," *J. Eur. Ceram. Soc.,* 29 [2] 283-291 (2009).
10. M. Patterson, J. E. Caiazza, D. W. Roy "Transparent Spinel Development," *Inorganic Optical Materials II Proc. SPIE,* 4102(1) [1] 59-68 (2000).
11. B. G. Pazol, P. T. McGuire, R. L. Gentilman, J. W. Locher, J. Askinazi "Large-area Flat and Curved Sapphire Window Blanks," *Inorganic Optical Materials II Proc. SPIE,* 4102(1) [1] 52-58 (2000).
12. G. C. Wei "Transparent Ceramics for Lighting," *J. Eur. Ceram. Soc.,* 29 [2] 237-244 (2009).
13. A. Krell, J. Klimke, T. Hutzler "Advanced Spinel and Sub-µm Al_2o_3 for Transparent Armour Applications," *J. Eur. Ceram. Soc.,* 29 [2] 275-281 (2009).
14. P. J. Patel, G. A. Gilde, P. G. Dehmer, J. W. McCauley "Transparent Armor," *AMPTIAC Newsletter,* Fall (2000).
15. O. Masala, R. Seshadri "Synthesis Routes for Large Volumes of Nanoporticles," *Annu. Rev. Mater. Res.,* 34 41-81 (2004).

16. M. K. Akhtar, Y. Xiong, S. E. Pratsinis "Vapor Synthesis of Titania Powder by Titanium Tetrachloride Oxidation," *J. Aerosol Sci.,* 22 [Supplement 1] S35-S38 (1991).
17. J.-G. Li, T. Ikegami, J.-H. Lee, T. Mori, Y. Yajima "Co-precipitation Synthesis and Sintering of Yttrium Aluminum Garnet (YAG) Powders: the Effect of Precipitant," *J. Eur. Ceram. Soc.,* 20 [14-15] 2395-2405 (2000).
18. H. G. Thomson "The Effect of Particle Size of Zinc Oxide on the Consistency of Glaze Slips," *J. Am. Ceram. Soc.,* (1929).
19. B. Yan, C. V. McNeff, P. W. Carr, A. V. McCormick "Synthesis and Characterization of Submicron-to-micron Scale, Monodisperse, Spherical, and Nonporous Zirconia Particles," *J. Am. Ceram. Soc.,* 88 [3] 707-713 (2005).
20. M. K. Wu, R. S. Windeler, C. K. R. Steiner, T. Bors, S. K. Friedlander "Controlled Synthesis of Nanosized Particles by Aerosol Processes," *Aerosol Sci. Tech.,* 19 [4] 527 - 548 (1993).
21. M. Nyman, J. Caruso, M. J. Hampden-Smith, T. T. Kodas "Comparison of Solid-state and Spray-pyrolysis Synthesis of Yttrium Aluminate Powders," *J. Am. Ceram. Soc.,* 80 [5] 1231-1238 (1997).
22. R. M. Young, E. Pfender "Generation and Behavior of Fine Particles in Thermal Plasmas,-A Review," *Plasma Chem. Plasma P.,* 5 [1] 1-37 (1985).
23. G. D. Ulrich "Flame Synthesis of Fine Particles," *Chem. Eng. News,* 62 [32] 22-29 (1984).
24. R. Strobel, S. E. Pratsinis "Flame Aerosol Synthesis of Smart Nanostructured Materials," *J. Mater. Chem.,* 17 4743-4756 (2007).
25. D. Segal "Chemical Synthesis of Ceramic Materials," *J. Mater. Chem.,* 7 [8] 1297-1305 (1997).
26. A. Gurav, T. Kodas, T. Pluym, y. Xiong "Aerosol Processing of Materials," *Aerosol Sci. Tech.,* 19 [4] 411 - 452 (1993).
27. "*Ultrafine Metal Oxide Powders By Flame Spray Pyrolysis*," R. M. Laine, C. R. Bickmore, D. R. Treadwell, K. F. Waldner; Regents of the University of Michigan, United States, **5,958,361**.
28. C. R. Bickmore, K. F. Waldner, D. R. Treadwell, R. M. Laine "Ultrafine Spinel Powders by Flame Spray Pyrolysis of a Magnesium Aluminum Double Alkoxide," *J. Am. Ceram. Soc.,* 79 [5] 1419-1423 (1996).
29. A. C. Sutorik, S. S. Neo, D. R. Treadwell, R. M. Laine "Synthesis of Ultrafine β"-alumina Powders via Flame Spray Pyrolysis of Polymeric Precursors," *J. Am. Ceram. Soc.,* 81 [6] 1477-1486 (1998).
30. R. M. Laine, R. Baranwal, T. R. Hinklin, D. R. Treadwell, A. C. Sutorik, C. R. Bickmore, K. F. Waldner, S. S. Neo "Making Nanosized Oxide Powders from Precursors by Flame Spray Pyrolysis," *Novel Synthesis and Processing of Ceramics,* 159-1 17-24 (1999).
31. R. Baranwal, M. Villar, R. Garcia, R. M. Laine "Flame Spray Pyrolysis of Precursors as a Route to Nano-mullite Powder: Powder Characterization and Sintering Behavior," *J. Am. Ceram. Soc.,* 84 [5] 951-961 (2001).

32. T. R. Hinklin, B. Toury, C. Gervais, F. Babonneau, J. Gislason, R. W. Morton, R. M. Laine "Liquid-Feed Flame Spray Pyrolysis of Metalloorganic and Inorganic Alumina Sources in the Production of Nanoalumina Powders," *Chem. Mater.,* 16 [1] 21-30 (2004).
33. R. M. Laine, J. C. Marchal, H. P. Sun, X. Q. Pan "A New $Y_3Al_5O_{12}$ Phase Produced by Liquid-Feed Flame Spray Pyrolysis (LF-FSP)," *Adv. Mater.,* 17 [7] 830 (2005).
34. J. A. Azurdia, J. C. Marchal, R. M. Laine "Synthesis and Characterization of Mixed-metal Oxide Nanopowders Along the CoO_x-Al_2O_3 Tie Line Using Liquid-Feed Flame Spray Pyrolysis," *J. Am. Ceram. Soc.,* 89 [9] 2749-2756 (2006).
35. J. A. Azurdia, J. C. Marchal, P. Shea, H. P. Sun, X. Q. Pan, R. M. Laine "Liquid-feed Flame Spray Pyrolysis as a Method of Producing Mixed-metal Oxide Nanopowders of Potential Interest as Catalytic Materials. Nanopowders Along the NiO-Al_2O_3 Tie Line Including $(NiO)_{0.22}(Al_2O_3)_{0.78}$, a New Inverse Spinel Composition," *Chem. Mater.,* 18 [3] 731-739 (2006).
36. J. A. Azurdia, A. McCrum, R. M. Laine "Systematic Synthesis of Mixed-metal Oxides in NiO–Co_3O_4, NiO–MoO_3, and NiO–CuO Systems via Liquid-Feed Flame Spray Pyrolysis," *J. Mater. Chem.,* 18 3249-3258 (2008).
37. P. Stamatakis, C. A. Natalie, B. R. Palmer, W. A. Yuill "Research Needs in Aerosol Processing," *Aerosol Sci. Tech.,* 14 [3] 316 - 321 (1991).
38. G. Beaucage, H. K. Kammler, R. Mueller, R. Strobel, N. Agashe, S. E. Pratsinis, T. Narayanan "Probing the Dynamics of Nanoparticle Growth in a Flame Using Synchrotron Radiation," *Nat. Mater.,* 3 [6] 370-373 (2004).
39. G. D. Ulrich, N. S. Subramanian "III. Coalescence as a Rate-controlling Process," *Combust. Sci. Technol.,* 17 [3] 119-126 (1977).
40. F. S. Lai, S. K. Friedlander, J. Pich, G. M. Hidy "The Self-preserving Particle Size Distribution for Brownian Coagulation in the Free-molecule Regime," *J. Colloid Interface Sci.,* 39 [2] 395–405 (1972).
41. S. Tsantilis, S. E. Pratsinis "Evolution of Primary and Aggregate Particle-size Distributions by Coagulation and Sintering," *AIChE J.,* 46 [2] 407-415 (2000).
42. H. K. Kammler, L. Madler, S. E. Pratsinis "Flame Synthesis of Nanoparticles," *Chem. Eng. Technol.,* 24 [6] 583-596 (2001).
43. R. L. Coble "Initial Sintering of Alumina and Hematite," *J. Am. Ceram. Soc.,* 41 [2] 55-62 (1958).
44. P. Vergnon, M. Astier, D. Beruto, G. Brula, S. J. Teichner "Sintering of Very Finely Divided Particles, II. Flash Heating Technique and Kinetic Study of Shrinkage in Titanium Oxide and Aluminum Oxide Compacts," *Rev. Int. Hautes Temp. Refract,* 9 271 (1972).
45. S. E. Pratsinis "Flame Aerosol Synthesis of Ceramic Powders," *Prog. Energ. Combust.,* 24 [3] 197-219 (1998).
46. M. S. Wooldridge "Gas-phase Combustion Synthesis of Particles," *Prog. Energ. Combust.,* 24 [1] 63-87 (1998).
47. R. S. Windeler, S. K. Friedlander, K. E. J. Lehtinen "Production of Nanometer-sized Metal Oxide Particles by Gas Phase Reaction in a Free Jet. I: Experimental System and Results," *Aerosol Sci. Tech.,* 27 [2] 174-190 (1997).

48. T. Lesniewski, S. K. Friedlander "The Effect of Turbulence on Rates of Particle Formation by Homogeneous Nucleation," *Aerosol Sci. Tech.,* 23 [2] 174-182 (1995).
49. N. Shinohara, M. Okumiya, T. Hotta, K. Nakahira, M. Naito, K. Uematsu "Formation Mechanisms of Processing Defects and Their Relevance to the Strength in Alumina Ceramics Made by Powder Compaction Process," *J. Mater. Sci.,* 34 [17] 4271-4277 (1999).
50. S. Baklouti, T. Chartier, J. F. Baumard "Binder Distribution in Spray-dried Alumina Agglomerates," *J. Eur. Ceram. Soc.,* (1998).
51. C. Herring "Effect of Change of Scale on Sintering Phenomena," *J. Appl. Phys.,* 21 301 (2004).
52. S. J. Lukasiewicz "Spray-drying Ceramic Powders," *J. Am. Ceram. Soc.,* 72 [4] 617-624 (1989).
53. W. H. Rhodes "Agglomerate and Particle Size Effects on Sintering Yttria-stabilized Zirconia," *J. Am. Ceram. Soc.,* 64 [1] 19-22 (1981).
54. M. F. Yan "Microstructural Control in the Processing of Electronic Ceramics," *Mater. Sci. Eng.,* (1981).
55. R. M. Cannon, W. C. Carter "Interplay of Sintering Microstructures, Driving Forces, and Mass Transport Mechanisms," *J. Am. Ceram. Soc.,* 72 [8] 1550-1555 (1989).
56. A. Krell, P. Blank, H. Ma, T. Hutzler, M. P. B. Bruggen, R. Apetz "Transparent Sintered Corundum With High Hardness and Strength," *J. Am. Ceram. Soc.,* 86 [1] 12-18 (2003).
57. W. Peukert, H. C. Schwarzer, F. Stenger "Control of Aggregation in Production and Handling of Nanoparticles," *Chem. Eng. Process.,* 44 [2] 245-252 (2005).
58. W. A. Yarborough, R. Roy "Microstructural Evolution in Sintering of AlOOH Gels," *J. Mater. Res.,* 2 [4] 494-515 (1987).
59. M. Kitayama, J. A. Pask "Formation and Control of Agglomerates in Alumina Powder," *J. Am. Ceram. Soc.,* 79 [8] 2003-2011 (1996).
60. N. Chantaramee, S. Tanaka, K. Uematsu "The Effect of Packing Structure of Powder Particles on Warping During Sintering," *J. Eur. Ceram. Soc.,* 28 [1] 21-25 (2008).
61. F. F. Lange "Sinterability of Agglomerated Powders," *J. Am. Ceram. Soc.,* 67 [2] 83-89 (1984).
62. T. J. Vogler, M. Y. Lee, D. E. Grady "Static and Dynamic Compaction of Ceramic Powders," *Int. J. Solids Struct.,* 44 [2] 636-658 (2007).
63. S. W. Sofie, F. Dogan "Freeze Casting of Aqueous Alumina Slurries With Glycerol," *J. Am. Ceram. Soc.,* 84 [7] 1459-1464 (2001).
64. W. C. Johnson, R. L. Coble "A Test of the Second-phase and Impurity-segregation Models for MgO-Enhanced Densification of Sintered Alumina," *J. Am. Ceram. Soc.,* 61 [3-4] 110-114 (1978).
65. R. L. Coble "Sintering Crystalline Solids. I. Intermediate and Final State Diffusion Models," *J. Appl. Phys.,* 32 787 (1961).
66. P. L. Chen, I. W. Chen "Sintering of Fine Oxide Powders: I, Microstructural Evolution," *J. Am. Ceram. Soc.,* 79 [12] 3129-3141 (1996).

67. J. Kanters, U. Eisele, J. Rödel "Effect of Initial Grain Size on Sintering Trajectories," *Acta Mater.,* 48 [6] 1239-1246 (2000).
68. J. R. Groza "Nanosintering," *Nanostruct. Mater.,* 12 [5-8] 987-992 (1999).
69. H. Hahn, J. Logas, R. S. Averback "Sintering Characteristics of Nanocrystalline TiO_2," *J. Mater. Res.,* 5 [3] 609-614 (1990).
70. O. Sudre, F. F. Lange "Effect of Inclusions on Densification: I, Microstructural Development in an Al_2O_3 Matrix Containing a High Volume Fraction of ZrO_2 Inclusions," *J. Am. Ceram. Soc.,* 75 [3] 519-524 (1992).
71. F. F. Lange, B. J. Kellett "Thermodynamics of Densification: II, Grain Growth in Porous Compacts and Relation to Densification," *J. Am. Ceram. Soc.,* 72 [5] 735-741 (1989).
72. J. Ma, L. C. Lim "Effect of Particle Size Distribution on Sintering of Agglomerate-free Submicron Alumina Powder Compacts," *J. Eur. Ceram. Soc.,* 22 [13] 2197-2208 (2002).
73. E. A. Olevsky "Theory of Sintering: From Discrete to Continuum," *Mater. Sci. Eng,* 23 41–100 (1998).
74. B. J. Kellett, F. F. Lange "Thermodynamics of Densification: I, Sintering of Simple Particle Arrays, Equilibrium Configurations, Pore Stability, and Shrinkage," *J. Am. Ceram. Soc.,* 72 [5] 725-734 (1989).
75. H. Erkalfa, Z. Misirli, T. Baykara "The Effect of TiO_2 and MnO_2 on Densification and Microstructural Development of Alumina," *Ceram. Int.,* 24 [2] 81-90 (1998).
76. P. L. Chen, I. W. Chen "Sintering of Fine Oxide Powders: II, Sintering Mechanisms," *J. Am. Ceram. Soc.,* 80 [3] 637-645 (1997).
77. J. Zhao, M. P. Harmer "Effect of Pore Distribution on Microstructure Development: II, First-and Second-generation Pores," *J. Am. Ceram. Soc.,* 71 [7] 530-539 (1988).
78. C. Pacurariu, I. Lazau, Z. Ecsedi, R. Lazau, P. Barvinschi, G. Marginean "New Synthesis Methods of $MgAl_2O_4$ Spinel," *J. Eur. Ceram. Soc.,* (2007).
79. N. Russo, D. Fino, G. Saracco, V. Specchia "N_2O Catalytic Decomposition Over Various Spinel-type Oxides," *Catal. Today,* 119 [1-4] 228-232 (2007).
80. D. J. Singh, R. C. Rai, J. L. Musfeldt, S. Auluck, N. Singh, P. Khalifah, S. McClure, D. G. Mandrus "Optical Properties and Electronic Structure of Spinel $ZnRh_2O_4$," *Chem. Mater.,* 18 [11] 2696-2700 (2006).
81. S.-D. Mo, W. Y. Ching "Electronic Structure of Normal, Inverse, and Partially Inverse Spinels in the $MgAl_2O_4$ System," *Phys. Rev. B,* 54 [23] 16555-16560 (1996).
82. H. Zhang, R. Qi, D. G. Evans, X. Duan "Synthesis and Characterization of a Novel Nano-scale Magnetic Solid Base Catalyst Involving a Layered Double Hydroxide Supported on a Ferrite Core," *J. Solid State Chem.,* 177 [3] 772-780 (2004).
83. E. L. Foletto, R. W. Alves, S. L. Jahn "Preparation of Ni/Pt Catalysts Supported on Spinel ($MgAl_2O_4$) for Methane Reforming," *J. Power Sources,* 161 [1] 531-534 (2006).
84. D. R. Parker, M. A. Green, S. T. Bramwell, A. S. Wills, J. S. Gardner, D. A. Neuman "Crossover From Positive to Negative Magnetoresistance in a Spinel," *J. Am. Chem. Soc.,* 126 [9] (2004).

85. H. S. C. O'Neill, A. Navrotsky "Simple Spinels; Crystallographic Parameters, Cation Radii, Lattice Energies, and Cation Distribution," *Am. Mineral.,* 68 [1-2] 181-194 (1983).
86. H. S. C. O'Neil, A. Navrotsky "Cation Distributions and Thermodynamic Properties of Binary Spinel Solid Solutions," *Am. Mineral.,* 69 [7-8] 733-753 (1984).
87. S. S. Ata-Allah, M. K. Fayek, H. S. Refai, M. F. Mostafa "Mössbauer Effect Study of Copper Containing Nickel-Aluminate Ferrite," *J. Solid State Chem.,* 149 [2] 434-442 (2000).
88. L. Li, G. Li, R. L. Smith, H. Inomata "Microstructural Evolution and Magnetic Properties of $NiFe_2O_4$ Nanocrystals Dispersed in Amorphous Silica," *Chem. Mater.,* 12 [12] 3705-3714 (2000).
89. Z. Wang, S. K. Saxena, P. Lazor, H. S. C. O'Neill "An in Situ Raman Spectroscopic Study of Pressure Induced Dissociation of Spinel $NiCr_2O_4$," *J. Phys. Chem. Solids,* 64 [3] 425-431 (2003).
90. M. A. Gabal "Non-isothermal Decomposition of NiC_2O_4-FeC_2O_4 Mixture Aiming at the Production of $NiFe_2O_4$," *J. Phys. Chem. Solids,* 64 [8] 1375-1385 (2003).
91. T. R. Hinklin, J. A. Azurdia, M. Kim, J. C. Marchal, S. Kumar, R. M. Laine "Finding Spinel in All the Wrong Places," *Adv. Mater.,* 20 [7] 1373-1375 (2008).
92. T. R. Hinklin, R. M. Laine "Systematic Synthesis of Metastable Phases in the Magnesium Spinel – Alumina System," *Chem. Mater.,* 20 [2] 553-558 (2008).

Chapter 2.

Experimental

2.1. Introduction

This chapter details the general experimental techniques used in this thesis to synthesize all of the nanopowders described herein. The analytical techniques used to characterize the as-produced nanopowders and the ceramic pellets made from these nanopowders are also described in detail. Selected experimental descriptions are provided in the following chapters, specific to work conducted in those particular chapters. The syntheses of the metalloorganic precursors used in LF-FSP to produce the nanopowders described in this thesis are described in detail in the experimental section of each chapter.

2.2. Liquid-Feed-Flame Spray Pyrolysis

Liquid-feed flame spray pyrolysis (LF-FSP) is a method invented by the Laine group in the early 1990's.[1-5] The main synthesis principles and techniques have remained unchanged, but the apparatus has undergone some changes. In the past 15 years there have been significant modifications to each of the major components of the system. Most of the modifications were done to improve production rates. A schematic diagram of the current apparatus is shown in Figure 2-1. Figure 2-2 is an image of the current headplate assembly.

The apparatus consists of three main components: a fine spray generator, a combustion chamber and a nanopowder collection system. The fine spray (see below) is generated using a commercial nozzle, such as the BETE XA-PR, (Greenfield, MA) and a

valve-less rotating piston liquid pump, such as a FMI Q1, (Syosset, NY). The nozzle system uses compressed O_2, typically between 0.40 and 0.55 MPa (60–80 psig) to produce highly atomized sprays, (droplet sizes of 20 to 45 μm) of the precursor solution being fed by the pump.

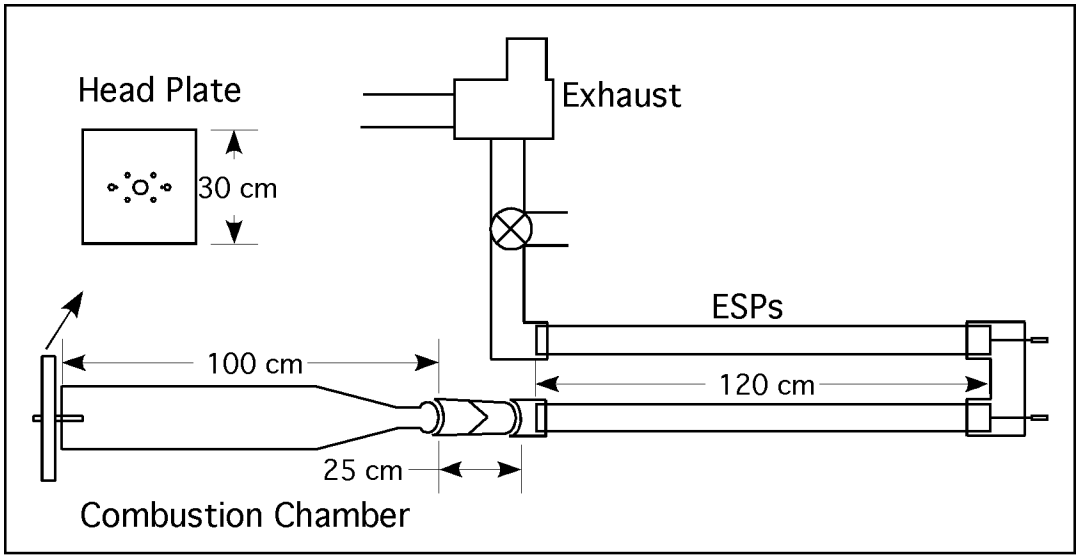

Figure 2-1. Schematic diagram of LF-FSP apparatus

A number of parameters affect the final nanopowder characteristics. Production rates can be controlled by adjusting two variables, precursor concentrations and pumping rates. Pumping rates can be adjusted in the range of 0–120 ml/min of precursor. Precursor concentrations can be varied between 1 and 25 wt. % ceramic in the form of dissolved precursor, concentrations are typically 3.5 wt. %. The ceramic yield of a precursor is the weight percent of the precursor that forms a particular metal oxide when fully combusted. The ceramic yield is determined by thermogravimetric analysis (see description below).

Combustion occurs in a 0.8 – 1 m long quartz chamber where two methane-oxygen premixed pilot torches ignite the fine spray generated by the nozzle. Typical flow rates are 35 and 25 ml/min respectively for the methane and oxygen. The nozzle is set in the

center of a water cooled, aluminum head-plate and the two torches are set 3 cm to either side of the nozzle at a 30° angle.

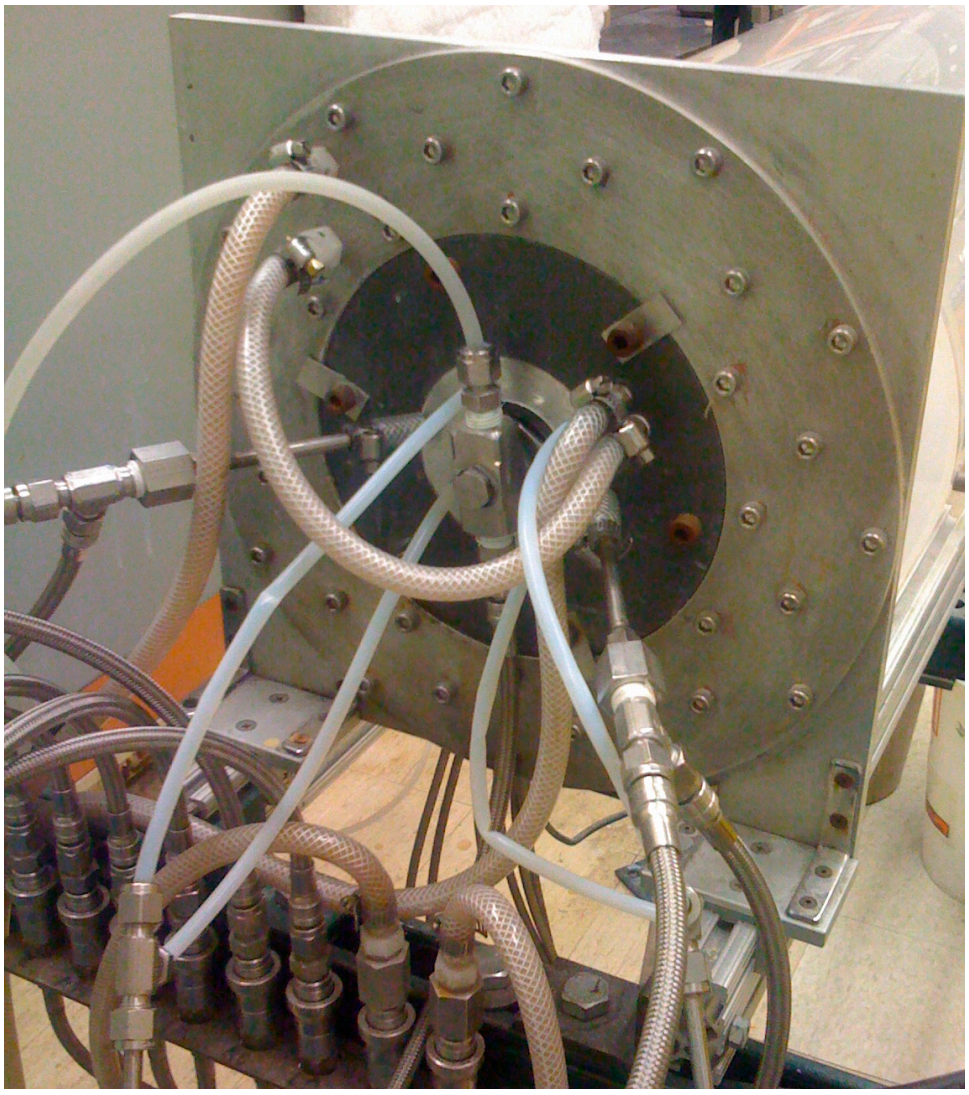

Figure 2-2. Head-plate image, showing gas, liquid and cooling connections

Depending on the material being synthesized, one of two different chamber configurations are used, a smaller diameter chamber (17.8 cm O.D.; 100 cm long) has a closed connection to direct flow into the collection system. This configuration allows for extra air intake at the head-plate. The extra air cools combustion gases and allows for a

degree of control over the flow rates throughout the apparatus. The larger diameter chamber (24.8 cm O.D.; 85 cm long) is not directly connected to the collection system allowing two air intakes; one at the head-plate and at the junction to the collection system. Figure 2-3 is a schematic of the two chambers used in LF-FSP.

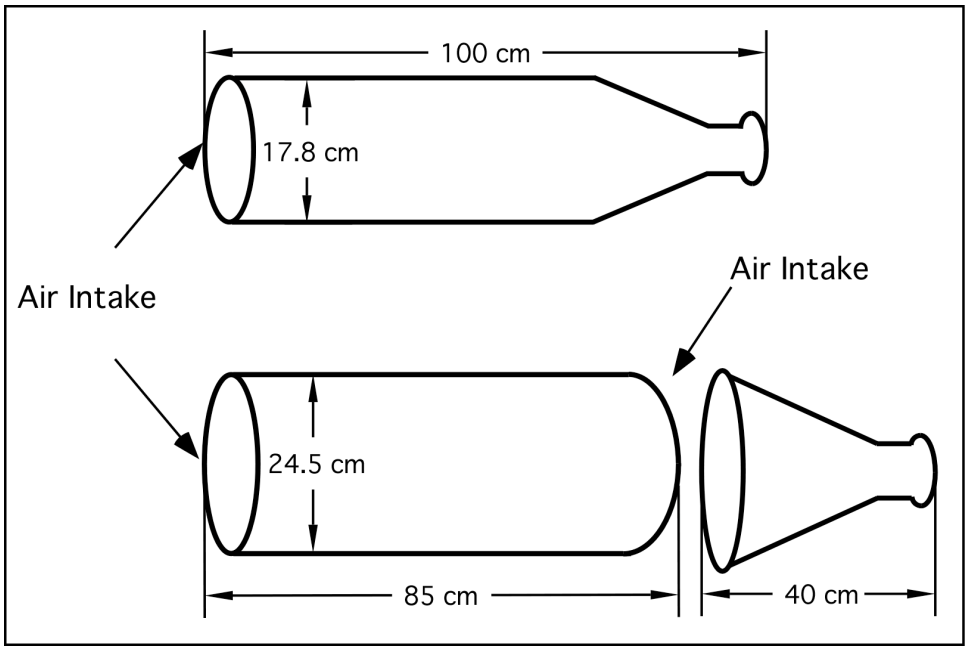

Figure 2-3. Schematic diagram of the reaction chambers

The larger diameter chamber is used to re-process nanopowders previously produced. These nanopowders are dispersed in ethanol and the dispersion is used as a precursor, this techniques is called solution-feed flame spray pyrolysis (SF-FSP). Although SF-FSP is currently being used, there is no further discussion of it in the present document because non of the materials involved were processed using this technique.

Combustion can produce temperatures in excess of 2000 °C but temperatures can vary significantly depending on a series of adjustable variables. The pumping rate and choice of solvent have the greatest effect on the temperature. The heat of combustion of the precursor will also affect the temperature. Table 2-1 shows the heats of combustion of

the more common solvents used in LF-FSP. The gas flows including supplementary oxygen, air intake and overall exhaust rates affect the temperature in the chamber to a lesser degree.

Table 2-1. Heats of combustion of solvents typically used in LF-FSP [6,7]

	Methanol	Ethanol	Butanol	THF
ΔH_C° (kJ/mol)	-725.7	-1367.6	-2677.4	-2505.8
50:50 mol with EtOH	-1046.6		-2022.5	-1936.7

The nanopowders and combustion byproducts are drawn downstream from the combustion chamber by a radial pressure exhaust blower (19.8 m^3/min) into the collection system and finally to the exhaust. The powders are collected typically in a pair of electrostatic precipitators (ESP) maintained at a 10 kV pseudo DC potential. The ESP are simple aluminum tubes (7.5 cm O.D. by 120 cm long) with a braided inconel wire in the middle. Alternately, powder can be collected in a custom built, commercial bag-house by SLY Inc., (Strongsville, OH). In order to use the bag house, the ESPs are moved aside and the chamber is connected via a reducing funnel directly to the inlet of the bag house. The bag house is equipped with 16 Nomex bags providing, 13.4 m^2 of filter area and is outfitted with an external blower that operates at 24.4 m^3/min. Once the apparatus has cooled below 40 °C, the nanopowders are recovered manually from either the ESPs or the bag-house.

2.3. General Analytical Methods

2.3.1. Specific surface area analyses

A Micromeritics ASAP 2010 sorption analyzer (Norcross, GA) was used to obtain specific surface areas (SSAs) and pore size distribution information. The

nanopowders were loaded into sample holders (350 mg) and degassed at 350 °C until a degass rate less than 0.6 Pa/min (5 mTorr/min) was achieved. A sorption technique with N_2 as the adsorbate gas at -196 °C (77 K) was used to perform the analysis. The SSAs were calculated using the Brunner-Emmet-Teller (BET) multipoint method (10 points) on the adsorption isotherm with relative pressures of 0.01 to 0.3. The average particle diameter or size (APS) was determined by:

$$d_{BET} = \frac{6}{\rho \times SSA} \qquad \textbf{Equation 2-1}$$

where ρ is the theoretical density of the nanopowders. The theoretical density for mixed metal nanopowders is determined using a simple rule of mixtures of the two pure oxides.

2.3.2. Diffuse reflectance infrared Fourier transform spectrometry

Diffuse reflectance infrared Fourier transform spectrometry (DRIFTS) is used to determine what surface species may be present on the nanopowders. FTIR probes molecules that have specific frequencies at which they rotate or vibrate corresponding to discrete energy levels. The spectra were collected and recorded on two different instruments: a Mattson Galaxy Series FTIR 3000 spectrometer (Mattson Instruments, Inc., Madison, WI) and a Nicolet 6700 FT-IR Spectrometer (Thermo Scientific, Waltham, MA). The sample preparation for both instruments was the same. First, the sample chamber was continuously flushed with N_2 to remove atmospheric CO_2 and moisture. Background scans of optical grade KBr were prepared by finely grinding ~400 mg and firmly packing the powder into a sample holder and leveling it to provide a smooth surface. The samples were prepared in a similar method as the background, ~4 mg of nanopowder were added to the ground KBr and then packed

into a sample holder. Spectra were collected continuously in the range 4000–400 cm^{-1}. The resolution of the Galaxy instrument was ±4 cm^{-1} while the resolution of the Nicolet instrument was ±2 cm^{-1}, each spectrum in both instruments was an average of 156 scans.

2.3.3. Thermogravimetric and differential thermal analyses

Studies were performed on a SDT 2960 simultaneous DTA-TGA instrument (TA Instruments, Inc., New Castle, DE). Sample pellets (~40 mg, 3.0 mm dia.) were prepared using a dual action hand press and loaded into either a platinum or alumina sample pan, depending on reactivity of sample. An α-Al_2O_3 pellet was used in a reference platinum or alumina pan. The instrument was heated at ramp rates between 5 and 15 °C/min to temperatures up to 1400 °C. A continuous flow of 60 ml/min of either synthetic air or inert gas (N_2 or Ar) was used to exhaust any evolved gases; data was collected only on heating. The instrument was allowed to cool to room temperature under constant gas flow.

2.3.4. X-ray diffractometry

X-ray diffraction patterns (XRD) were collected on two different instruments; a Rigaku Miniflex diffractometer (Rigaku, The Woodlands, TX) and a Rigaku Rotating Anode Goniometer (Rigaku Denki Co. Ltd., Tokyo, Japan). Cu Kα radiation (λ= 1.5406 Å) was used for both instruments. The Miniflex has a working voltage of 30 kV and current of 15 mA. Scans were acquired from 20° to 80° (2θ) with increments of 0.03° and an acquisition time of 1.2 sec (1.5°/min). The Rotating Anode Goniometer has a Ni filter and was operated with a working voltage and current of 40 kV and 100 mA, respectively. Scans were continuous from 10° to 90° (2θ) with a

scan rate of 2° 2θ/min in increments of 0.01° 2θ. The nanopowder samples were prepared by packing ~100 mg into an amorphous silica holder and loaded into the diffractometer. Scan data were analyzed using Jade software versions 3.5 to 8.5 (Materials Data, Inc, Livermore, CA) to determine phases present, average crystallite sizes (XSs) and unit cell parameters.

2.3.5. Scanning electron microscopy

Scanning electron micrographs (SEM) were taken using two instruments, namely a Field Emission Gun Scanning Electron Microscope, FEG XL-30, (Phillips, now FEI, Netherlands) or a Nova 600 Nanolab Focused Ion Beam Workstation and Scanning Electron Microscope FIB/SEM (FEI Company, Hillsboro, OR). An operating voltage between 5-30 kV was used for either of the two instruments. The operating voltage range varied because of sample conditions, some materials are more conductive than others. Samples with different phases require a range of voltages to display enough contrast when the materials have similar compositions. The nanopowder samples (~1 mg each) were dispersed in 5 ml of de-ionized water using an ultrasonic horn (Vibra-cell, Sonics and Materials Inc., Newton, CT) for 10 min. A drop of the dispersion was placed on a SEM sample stub, and allowed to dry on a covered hot plate.

Ceramic pellets and green body morphologies were also studied by SEM. All micrographs are either from fractured or polished surfaces. All pellet samples were mounted in epoxy and prepared by grinding to a flat surface and polishing using subsequent finer media (last step was 0.025 μm colloidal silica). To enhance particle resolution and avoid charging effects samples were sputter coated with ~20 nm of

Au-Pd using a Technics Hummer VI sputtering system (Anatech, Ltd., Alexandria, VA).

2.3.6. Transmission electron microscopy

Two transmission electron microscopes (TEM) were used to study individual particle morphologies. One was a JEOL 2100 XL operating with an accelerating voltage of 200kV and an analytical high resolution TEM 3011 JEOL, (Hikashima, Japan) operating at an accelerating voltage of 300 kV. Samples were held in a Gatan double tilt goniometer, and standard microscopy procedures where followed. Samples were prepared by immersing a holey carbon grid in an ultrasonicated solution of ~0.5 mg of nanopowder in methanol and allowing them to dry at ambient temperature.

2.3.7. Dilatometric Studies

Constant heating rate sintering curves were obtained using a Dilatronics 6548 (Theta Industries Inc., Port Washington, NY). Small sections cut from green bodies were loaded into a single push-rod holder and placed under a constant load (20 mg). Heating rates were varied from 2 to 10 °C/min. Samples were run in stagnant air and in vacuum (-99.99 kPa). Data were acquired using a National Instruments DAC and recorded using a custom built virtual instrument (commonly known as VI) using LabView 8.0 software (National Instruments Corporation, Austin, TX).

2.4. General processing techniques

2.4.1. Heat treatment and density equipment

Heat treatments of nanopowders, green bodies and ceramic pellets were conducted in two types of furnaces. For temperatures above 850 °C a Lindberg/Blue tube furnace Model No. 58114, (Watertown WI), and for temperatures up to 850 °C a

Thermolyne Type 6000 Furnace was used. Both furnaces are equipped with the same type of controller, a Eurotherm microprocessor, Model No. 818P (Northing, England). The atmosphere in the tube furnace was either synthetic air, pure O_2, N_2, Ar or regen gas (10 wt. % H in Ar) or vacuum, typical flow rates for the gases range between 80 and 150 ml/min. Pellets were placed on either alumina or zirconia plates or boats and heated at ramp rates between 3 and 20 °C/min to temperatures between 1000 and 1400 °C. Typical dwelling times were 0–10 h. A geometric technique was used to determine ceramic pellet densities. For compacts > 95% dense, the Archimedes method was employed. This method uses the pellets' buoyancy and the known density of a liquid to calculate the solid's density.

2.4.2. Standard nanopowder post treatment

Powders were dispersed in ethanol using a Vibra-cell VCX 500 ultrasonic horn (Sonics and Materials Inc., Newton, CT). Pre-dissolved surfactants (2 wt. % bicine or 2 wt. % stearic acid in water; oxide basis) were added as needed. The nanopowders were then sequentially sieved using nylon mesh sieves (-200 and -400). A settling period between sieving steps was used to remove larger particles or aggregates. This processing resulted in the removal of up to 60% of the initial mass. The nanopowders were re-dispersed in ethanol. If needed, up to 2 wt. % pre-dissolved binders (PVA, PEG, PMA) were added and then the nanopowders were dried in a convection oven at 90 °C overnight. The dried powders were ground in an alumina mortar and pestle and sieved (-400) one last time.

2.4.3. Pellet formation and pressing

A laboratory Carver Press (model 3912) was used to form pellet compacts. The nanopowders were loaded into a polished tungsten carbide double-action die (dia. 12.75 mm) and pressed for 60 to 180 s to pressures between 30 and 180 MPa. The formed pellets typically had green densities between 40% and 60% of the theoretical density.

2.4.3.1. Cold Isostatic Pressing

An Autoclave Engineers cold isostatic press (Erie, PA) (now Avure Technologies, Kent, WA) was used to further increase the green density of the pellets by pressing them to pressures between 70 and 300 MPa. The previously pressed pellets were placed in individual latex gloves and evacuated using a vacuum pump, prior to loading them into the press to prevent any contamination or liquid infiltration. A typical run consisted of a pressurizing rate 5 MPa/min and a dwell time of 30 min, the pressure was typically released at 10 MPa/min.

2.4.3.2. Hot Isostatic Pressing

A MiniHIPer hot isostatic press MIH 3.1 (Autoclave Engineers: Erie, PA), (now Avure Technologies, Kent, WA) with a 7.6 by 15.24 cm cylindrical Molybdenum hot zone, was used to achieve full density of the compacts. Pellets were loaded on zirconia crucibles (McDanel, Beaver Falls, PA) and the press evacuated to ~7 Pa to remove atmospheric moisture and O_2. The press was operated at temperatures in the range of 1250 to 1450 °C, and pressures between 170 and 210 MPa with dwell times of 1 to 8 h.

2.5. Bibliography

1. "*Ultrafine Metal Oxide Powders by Flame Spray Pyrolysis*," R. M. Laine, C. R. Bickmore, D. R. Treadwell, K. F. Waldner; Regents of the University of Michigan, United States, **5,958,361**.
2. K. F. Waldner, R. M. Laine, S. Dhumrongvaraporn, S. Tayaniphan, R. Narayanan "Synthesis of a Double Alkoxide Precursor to Spinel ($MgAl_2O_4$) Directly From $Al(OH)_3$, MgO, and Triethanolamine and Its Pyrolytic Transformation to Spinel," *Chem. Mater.,* 8 [12] 2850-2857 (1996).
3. C. R. Bickmore, K. F. Waldner, D. R. Treadwell, R. M. Laine "Ultrafine Spinel Powders by Flame Spray Pyrolysis of a Magnesium Aluminum Double Alkoxide," *J. Am. Ceram. Soc.,* 79 [5] 1419-1423 (1996).
4. R. Narayanan, R. M. Laine "Synthesis and Characterization of Precursors for Group II Metal Aluminates," *Appl. Organomet. Chem.,* 11 [10-11] 919-927 (1997).
5. A. C. Sutorik, S. S. Neo, D. R. Treadwell, R. M. Laine "Synthesis of Ultrafine β"-Alumina Powders Via Flame Spray Pyrolysis of Polymeric Precursors," *J. Am. Ceram. Soc.,* 81 [6] 1477-1486 (1998).
6. J. Chao, F. D. Rossini "Heats of Combustion, Formation, and Isomerization of Nineteen Alkanols," *J. Chem. Eng. Data,* 10 [4] 374-379 (1965).
7. R. C. Cass, S. E. Fletcher, C. T. Mortimer, H. D. Springall, T. R. White "Heats of combustion and molecular structure. Part V. The mean bond energy term for the C–O bond in ethers, and the structures of some cyclic ethers," *J. Chem. Soc.,* 1406-1410 (1958).

Chapter 3.

Nanopowders Along the $NiO-Al_2O_3$ Tie-Line

3.1. Introduction

Numerous single and mixed-metal oxides, both pure and in supported forms, play important roles in commercial catalytic processes ranging from petroleum refining, to environmental control, to processing fine chemicals, to components in fuel cells. Of the many catalyst systems studied extensively, nickel spinel and alumina supported nickel catalysts are among those that have widespread commercial value in catalytic applications ranging from methane/steam and methanol reforming,[1-4] to hydrocarbon cracking, dehydrogenation, hydrodesulfurization and hydrodenitrogenation.[5-8] Most recently, nickel spinel has received attention as an electrode material in high temperature carbonate based fuel cells.[9,10]

Catalysts are prepared via a wide variety of methods including solid-state reactions, sol-gel processing, and incipient wetness and related support coating approaches.[11-15] Despite extensive studies designed to optimize synthetic methods in terms of surface areas, compositions, oxidation states, etc; there remains a need for general methods of preparing high surface area sinter-resistant catalysts that are easily manipulated for applications ranging from fluidized bed catalysis to simple supported liquid-solid and gas-solid catalysis. Such problems continue to exist for nickel spinel and alumina supported nickel catalysts.[16]

Phase pure nickel spinel with controlled stoichiometries are very difficult to synthesize by traditional methods because of the very high temperatures required to obtain sufficient solid state diffusion to drive the reaction to completion.[17-19] Liquid-feed flame spray pyrolysis (LF-FSP) provides a simple route to nanopowders of all compositions along the NiO-Al_2O_3 tie-line with excellent control of both stoichiometry, phase and high surface areas without microporosity. LF-FSP of $Ni(O_2CCH_2CH_3)_2$ and $Al(OCH_2CH_2)_3N$ ethanol solutions at selected ratios provides mixed-metal oxide nanopowders with compositions covering much of Al_2O_3-NiO phase space. This work extends the utility of LF-FSP as a means of producing a wide variety of mixed-metal oxide nanopowders with: limited agglomeration, complete control of stoichiometry, selected control of phase purity, no microporosity and good-to-excellent handling characteristics.[20-27]

These studies provide the background for efforts initiated here to develop new types of single-phase catalyst systems using LF-FSP. Complimentary work on the use of LF-FSP to synthesize phase-segregated catalyst materials has been described by Sotiris and Baiker.[28-31] This chapter details the work done for materials in the NiO-Al_2O_3 phase space, with the goal of demonstrating that LF-FSP offers the potential to generate novel, single-phase forms of catalytic materials, which contrasts with earlier efforts in this field which suggest that it is difficult to form phase pure nickel spinels.[32-34] Compositions near 20:80 mol NiO:Al_2O_3 generate an inverse spinel structure, per XRD with peaks shifted ≈ 0.4° 2θ to higher values from those of pure $NiAl_2O_4$. This contrasts with the published phase diagram, which suggests a mixture of $NiAl_2O_4$ spinel and corundum should form at

this composition. This material is indeed a single stable phase, which contrasts with the known phase diagram, and therefore is a new material in NiO-Al_2O_3 phase space.

3.2. Experimental

This section details the synthesis of the individual metalloorganic precursors used in LF-FSP to produce the nanopowders described in this chapter.

3.2.1. Materials

Nickel nitrate hexahydrate [$Ni(NO_3)_2$•$6H_2O$, 99.9%], anhydrous ethanol and n-butanol, propionic acid [$C_2H_5CO_2H$, 99$^+$%] and triethanolamine [$N(CH_2CH_2OH)_3$ 98%] were purchased from Aldrich and used as received. Aluminum tri-(*sec*-butoxide) [$(C_2H_5CH(CH_3)O)_3Al$ 97%] was purchased from Chattem Chemical Company and also used as received.

3.2.1.1. Aluminum precursor

Alumatrane was produced by adding an equimolar amount of aluminum tri-(*sec*-butoxide) drop-wise into a 5 L mechanically stirred flask containing triethanolamine. The specific steps of this reactions are described in much greater detail elsewhere.[24-27] The reaction product (a viscous yellow solution) was then diluted in ethanol such that the solution's TGA ceramic yield was 7 wt.%.

3.2.1.2. Nickel precursor

$Ni(NO_3)_2 \cdot 6H_2O$ powder (75.0 g, 0.2579 mole) was placed in a 500 mL flask equipped with a still head, addition funnel, and an N_2 sparge. Propionic acid (250 mL, 3.40 moles) was added rapidly and the resulting solution heated to ~150 °C for 4h to distill off ~140 mL of liquid (water/propionic acid) and

coincidentally remove NO_x gas. The remaining liquid product was placed in a clean 500 mL Nalgene® bottle. The ceramic yield of the solution was determined by TGA to be 9.7 wt. %. This procedure was repeated twice to produce ~450 mL $Ni(O_2CCH_2CH_3)_2$, sufficient to produce all of the samples.

The solid nickel propionate was isolated by first washing the liquid precursor with ~450 mL (1.75 mol) of tetrahydrofuran (THF). The solution was slowly heated to distill off excess solvent and reactant. After the solution was reduced to ~200 mL of a viscous green liquid it was transferred to a rotary evaporator (Buchi RE-111, Postfach, Switzerland) where it was dried to a solid under a dynamic vacuum at 70 °C. The TGA of this precursor is discussed in the results and discussion section.

Eight different precursor formulations presented in Table 3-1 were prepared to study the $NiO\text{-}Al_2O_3$ phase space. Thus, precise amounts of alumatrane solution and nickel propionate solutions where mixed and diluted in ethanol to produce 4 wt. % ceramic yield solutions. The samples produced where pure Al_2O_3, 3, 5, 22, 43, 63, 78 mol % NiO, and pure NiO. The production rates are for this particular set of experiments where typically 30–50 g/h.

Table 3-1. $NiO\text{-}Al_2O_3$ Precursors formulations

Sample	Mol% NiO	Moles Al_2O_3	Moles NiO
1	0.0	0.098	0.000
2	3.2	0.954	0.029
3	5.3	0.933	0.051
4	22.2	0.806	0.228
5	43.5	0.622	0.475
6	62.8	0.446	0.717
7	77.9	0.270	0.955
8	100.00	0.000	0.133

3.2.2. Specific analytical methods

Elemental analysis using X-Ray Fluorescence (XRF) was performed on all samples. Bombarding with high-energy X-rays generates emission of characteristic elemental "secondary" (or fluorescent) X-rays, accurate to ppm levels. The samples were prepared by mixing 0.50g of sample into 10.0g of $Li_2B_4O_7$ glass flux. The sample and glass flux were mechanically stirred for 5 minutes in a methacrylate vial with three methacrylate balls using a SPEX 6000 ball mill (SPEXCertiPrep, Metuchen, NJ). The mixtures were fused into glass beads by placing them in an oven held at 1000 °C for 10 min. The samples were analyzed using a Panalytical PW2400 X-Ray Fluorescence spectrometer (formerly Philips), equipped with a WDS detection system (wavelength dispersive).

Inductively Coupled Plasma – Atomic Emission Spectroscopy (ICP-AES) was performed on all samples. An Ar plasma torch was used to produce excited atoms and ions that emit electromagnetic radiation at wavelengths characteristic of a particular element. The intensity of this emission is indicative of the concentration of the element within the sample.

3.3. Results and discussion

The objective of the work reported here is to demonstrate that LF-FSP processing can provide high surface area (>40 m^2/g), mixed-metal oxide nanopowders without microporosity, along the NiO-Al_2O_3 tie-line with the goal of generating materials with compositions known to offer good catalytic properties with atomic mixing of the precursor ions.[1-5] The absence of microporosity is important given that many high surface area catalysts (>50 m^2/g) made using sol-gel techniques and/or by impregnation of micro-

porous supports suffer from aging processes wherein the micro-pores are removed during aging by sintering processes, which in turn remove active metal initially deposited within the micro-pores. Furthermore, because the high surface area is achieved by making catalyst particles with very small diameters, much of the catalyst material is at the particle surface, in principle, ensuring that the major portion of the metal species that could be active can in fact contribute to catalyst activity.

The downside to this approach is that in some instances, catalyst recycling may be difficult because of the difficulty in recovering the catalyst particles. However, where high activity is obtained, it may not be necessary to recover the catalyst if it used in small amounts. Alternately, many applications involve gas or liquid phase reactions where the gaseous reactants and/or products may be separated even from fine particulates. One potential solution to this problem is to very lightly sinter (promote limited necking between particles) these active species to retain the high surface area of the primary particles while limiting their mobility. However, such issues are not an immediate concern of the work reported here.

Spinels are a common structural arrangement shared by many transition metal oxides of the general formula AB_2O_4. These structures can be further divided into three types: normal, inverse and intermediate spinels.[32,33] They all consist of a cubic close packed (face centered) sub-lattice of oxygen atoms with 1/8 of the tetrahedral sites and 1/2 of the octahedral sites occupied by the cations. The distinction between normal and inverse lies in which atoms occupy which positions.

In normal spinels, the tetrahedral (A sites) are occupied exclusively by divalent cations and octahedral (B sites) by trivalent cations. In an inverse spinel, half of the

trivalent cations replace the divalent cations so that divalent cations now occupy octahedral sites giving rise to the formula $B^{3+}(A^{2+}B^{3+})O_4$. The intermediate spinels have partial normal and partial inverse character and are normally labeled in terms of the percent inverse character they exhibit.[34]

The ability to predict formation of normal or inverse spinels has been of considerable interest since the 1930's when both structures were first observed. O'Neil and Navrotsky[35,36] have published a set of studies that examine factors such as electrostatic interactions, ligand field effects, and atomic radii on spinel cation distribution patterns. Cormack *et al.*[37] found through simulations based on electrostatic and short-range contributions, ion size, site preference energies (SPE) and coordination number that Ni^{2+} strongly prefers to occupy octahedral positions.

These findings are supported by studies on $NiCr_2O_4$[38,39] and $NiFe_2O_4$[40] that show that Ni^{2+} tends to force formation of inverse spinel phases. The results presented here show that the inverse spinel phase can "saturate" at high Ni contents, with the divalent cation driving formation of intermediate spinels. Furthermore at very low Ni^{2+} contents (LF-FSP produced samples with 22 and 43 mol % NiO) a single-phase intermediate spinel forms. The former composition forms an entirely inverse spinel per XRD, where the phase diagram suggests that a single phase should not form. Hence, the 22 % NiO material represents a new phase composition along the $NiO\text{-}Al_2O_3$ tie-line.

The basic formulations of the catalyst precursor solutions is first discussed, then a brief comparison of fuel/solvent systems used is presented The discussion of the characterization by BET, SEM, TEM, XRD, TGA-DTA and diffuse reflectance FTIR of the LF-FSP products follows.

3.3.1. Precursor synthesis and formulations

A detailed characterization of nickel propionate from thermogravimetric analysis (TGA) was performed because this was the first time that the precursor was synthesized in our labs. The nickel propionate, which has a thermal decomposition pattern similar to other metal carboxylate precursors previously examined,[21] was isolated and crystallized following the experimental procedure described above. Figure 3-1 is a TGA trace which shows an initial mass loss (≈14 %) event commensurate with the loss of ≈ 0.5 equivalents of propionic acid of recrystallization.

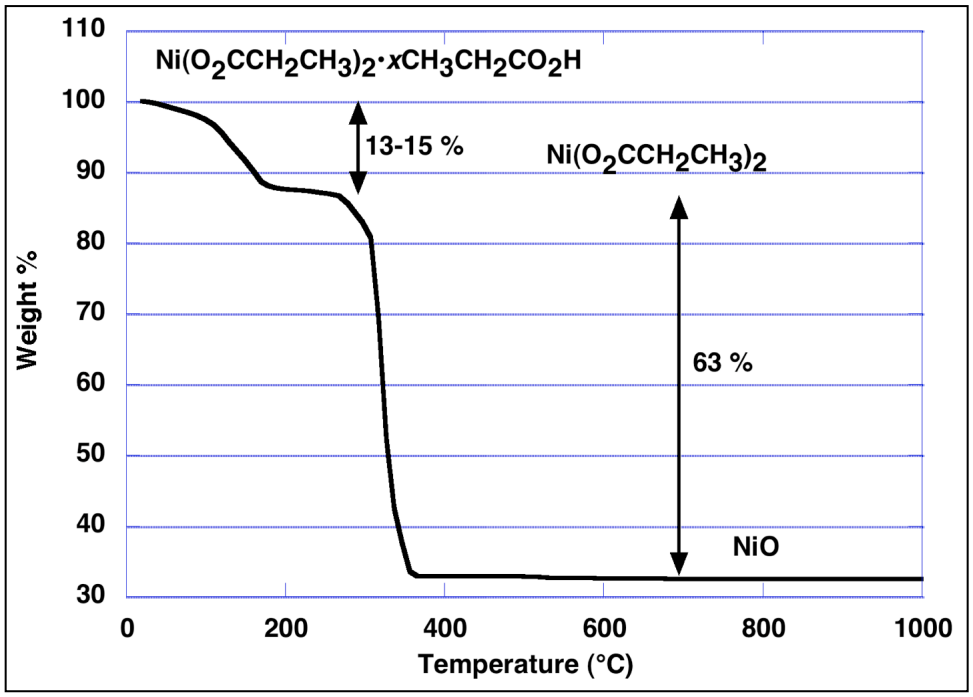

Figure 3-1. TGA of $Ni(O_2CH_2CH_3)_2$ ramped at 10 °C/min in synthetic air

The second mass loss between 250 and 300 °C is attributed to decomposition of the propionate ligands. The residue is 37.2 % of the total mass at this point and within experimental error of the calculated value (36.5%) for decomposition of $Ni(O_2CCH_2CH_3)_2$ to NiO and is expected based on previous studies on the thermal decomposition of metal carboxylates.[24-27]

The final TGA product was verified by XRD (not shown) to be NiO, confirming the suggested thermally promoted fragmentation of the two propionate ligands. The initial loss, attributed to propionic acid, indicates that the precursor prepared as described in the experimental section is $Ni(O_2CCH_2CH_3)_2 \cdot xCH_3CH_2CO_2H$ where x = 0.4 to 0.5.

Eight different precursor compositions were prepared to study the $NiO\text{-}Al_2O_3$ system, Table 3-1 lists the various compositions studied. Measured amounts of precursor/ethanol solutions were prepared such that the total ceramic loading (as precursor) in solution was 2.0–4.0 wt. %, typically 3 wt. %. All precursor systems thus formulated exhibited viscosities close to those of ethanol thereby minimizing potential problems with aerosolization. The compositions of all eight LF-FSP Samples were corroborated by Galbraith Laboratories (Knoxville, TN) using ICP and by XRF as detailed above.

3.3.2. Solvents-fuel effects

Three different batches of Sample 2 (3 mol % NiO in Al_2O_3) were produced using different solvent/fuel combinations. The first used pure ethanol, the second a 50:50 mol % methanol:ethanol and the last 50:50 mol % n-butanol:ethanol. The object was to control the flame temperature by changing the fuel's heats of combustion (Table 3-2)[41] in an effort to affect APSs and morphologies.

Table 3-2. Heat of combustion of solvent vehicles used

	Methanol	Ethanol	n-Butanol
Heat of combustion (kJ/L)	-17930	-23600	-29260
50:50 vol with ethanol (kJ/L)	-20760	-23600	-26430
Heat of combustion (kJ/mol)	-730	-1370	-2670
50:50 mol with ethanol (kJ/mol)	-1050	-1370	-2020

The different solvent/fuel combinations produce nearly identical powders as determined by XRD powder patterns and particle morphologies (SEM, TEM). Likewise, TGA and DTA data show no significant difference between the samples. The SSAs are, within error limits, all the same. Hence, efforts to change particle morphology via variations in flame temperatures appear not to make a difference for LF-FSP. This suggests that it is the rapid quenching process and overall gas flows in LF-FSP that defines particle morphologies.

In general, the temperatures at the exit to the 1.25 m (0.20 m dia.) quartz combustion chamber are 400–500 °C, corresponding to a drop of 1000–1500 °C in a 1 meter length depending on the processing conditions. At these quenching rates, the gas phase ions produced during combustion have, as has been discussed elsewhere,[20-27] microseconds to cool and condense. Thus, the time for these species to form nuclei is very limited. Indeed the time is sufficiently limited that uniform stoichiometries reflecting the original solution stoichiometries are almost always observed. Furthermore, the time for collisions between growing nuclei at temperatures that produce particle necking that in turn would lead to hard agglomerates is also limited. Thus, the product powders are typically single particles with very few necks. Surprisingly, this quenching rate rarely leads to glassy products.

3.3.3. Powder characterization.

All LF-FSP powders were characterized by BET, SEM, TEM, XRD, TGA-DTA and diffuse reflectance FTIR spectroscopy (DRIFTS) as discussed in the following sections. These characterization tools allow us to better understand particle

morphologies, sizes and distributions, phase composition, surface areas and chemistries.

3.3.3.1. Surface area analyses

Specific surface areas of the as-produced powders were obtained by BET method (see experimental) and used along with XRD peak broadening to estimate particle sizes, see Table 3-3. No microporosity was expected nor detected by t-plot method. With the exception of the pure NiO powders, the SSAs at all compositions exceed 45 m^2/g. It is important to note that with advances in optimization of synthesis techniques a later batch of NiO had a surface area of 39 m^2/g. At some compositions along the NiO-Al_2O_3 tie-line, the observed SSAs are up to 30% greater than pure δ-Al_2O_3 (80 vs. 60 m^2/g). Consequently, the average particle sizes decrease with the addition of NiO as compared to pure alumina, because particle nucleation and growth must be influenced by the materials composition such that growth is inhibited.

The melting temperature (T_m) for NiO•Al_2O_3 is ≥ 2100 °C whereas T_m for Al_2O_3 is < 2000 °C. If the boiling points and/or sublimation, or condensation temperatures for these materials follow suit, one might argue that under identical LF-FSP conditions, NiO•*x*Al_2O_3 nuclei will form from the gas phase and/or cease growing, nucleating, or coalescing at higher temperatures than pure Al_2O_3. This is one possible explanation for the higher average surface areas/smaller particle sizes.

Table 3-3. Surface areas and average particle sizes of all samples

Sample		SSA (m^2/g)	Theoretical Density (g/cm^3)	BET APS (nm) ±1	XRD APS (nm) ±2
1	Al_2O_3	57	3.65	29	29
2	3 mol% NiO	60	3.74	27	23
3	5 mol% NiO	77	3.77	21	19
4	22 mol% NiO	60	4.16	24	18
5	43 mol% NiO	69	4.76	18	20
6	63 mol% NiO	58	5.33	19	22
7	78 mol% NiO	45	5.86	23	20
8	NiO	7	6.72	134	62

3.3.3.2. Scanning electron microscopy

Scanning electron micrographs of as-prepared nano-powders were used to assess the overall particle distribution and morphology of each sample. All the powders exhibit similar spherical and homogeneous morphologies. The APSs are all < 80 nm, with a significant population of particles < 60 nm. Figure 3-2 provides an overview of the general particle population that allows one to conclude that no micron size primary particles are produced during LF-FSP of these materials. However, Figure 3-3, indicates the presence of electrostatically agglomerated particles, as seen with pure δ-Al_2O_3, which disperses fully despite the presence of these same types of agglomerates. [42]

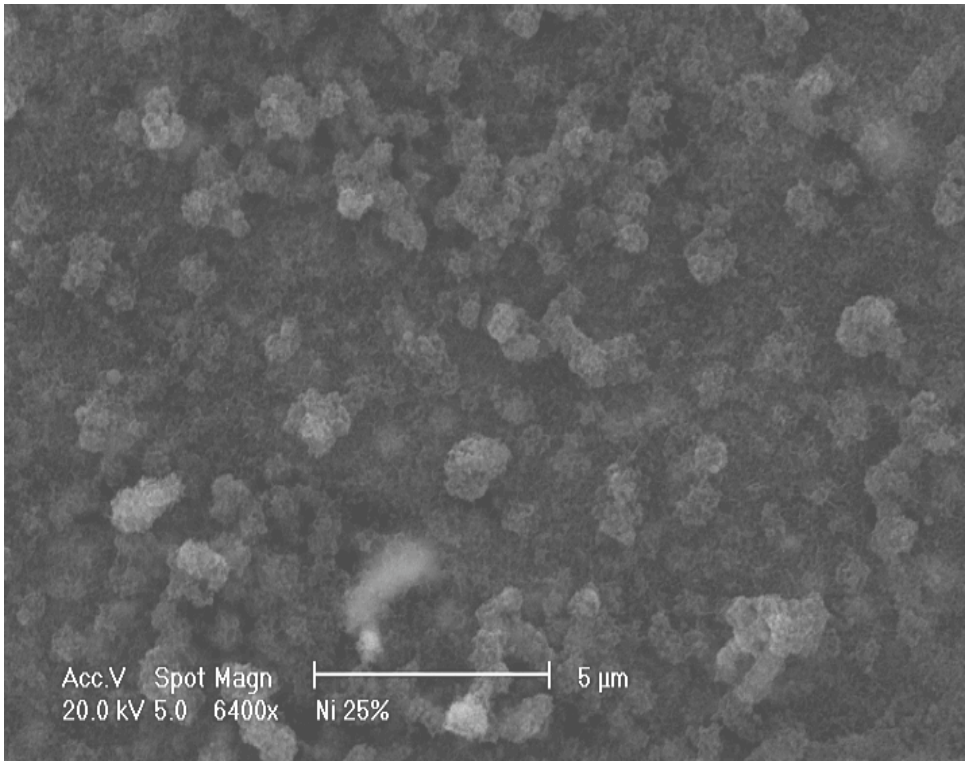

Figure 3-2. SEMs of sample 4, 22 mol % NiO

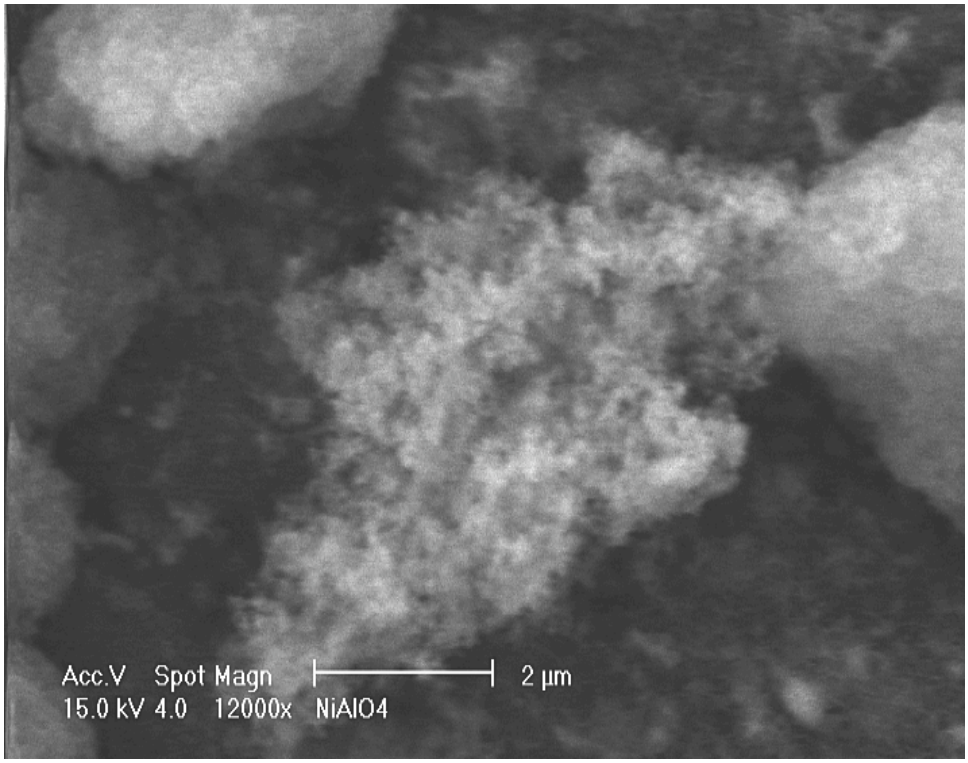

Figure 3-3. SEMs of sample 5, 43 mol % NiO

3.3.3.1. Transmission electron microscopy

HR-TEM images of Sample 4, 22 mol% NiO, Figures 4 and 5, are representative of all other powder samples. Figure 3-4 captures the appearance of the general particle population at a different length scale than seen by SEM. As stated above all of the particles are spherical, ≤ 80 nm in diameter with the majority < 30 nm. Moreover most particles are multi-faceted (Figure 3-5), suggesting a high degree of crystallinity. Particle necking while evident is not a major morphological feature for the reasons discussed above. Figure 3-5 does not reveal any obvious microporosity, as expected from the t-plot results.

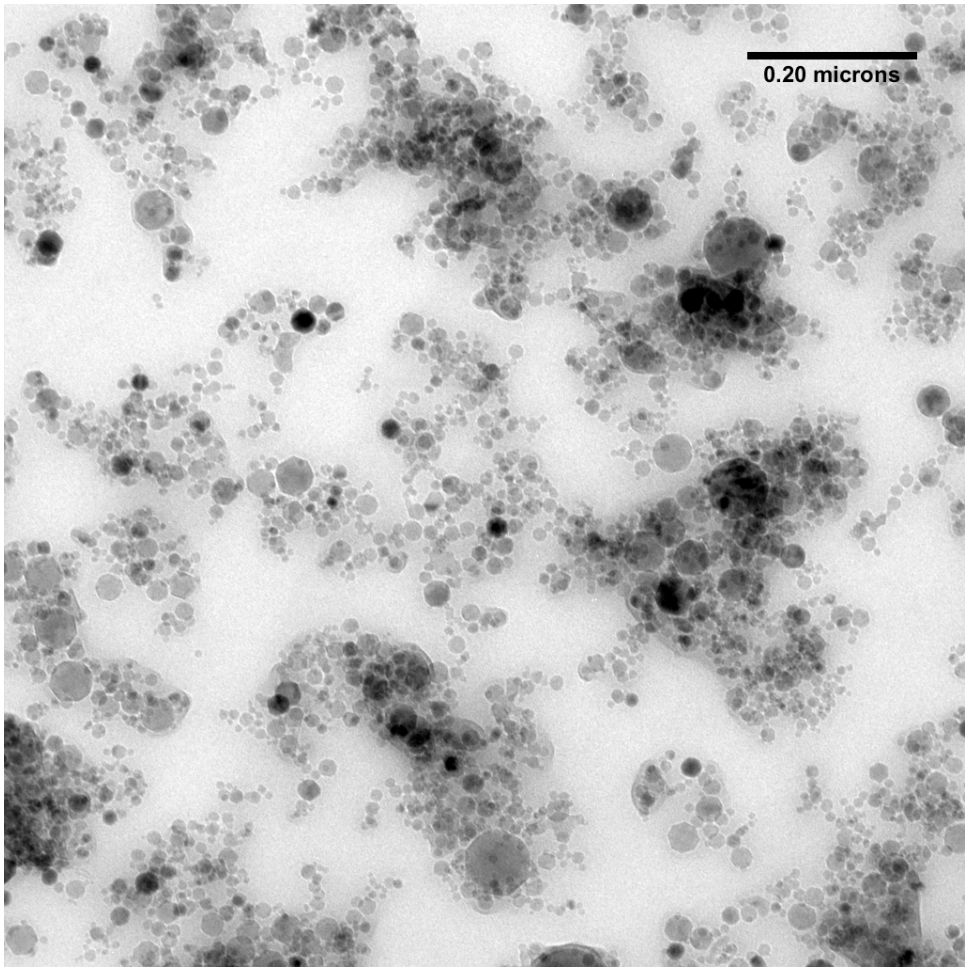

Figure 3-4. HRTEM showing distribution of particles throughout the sample

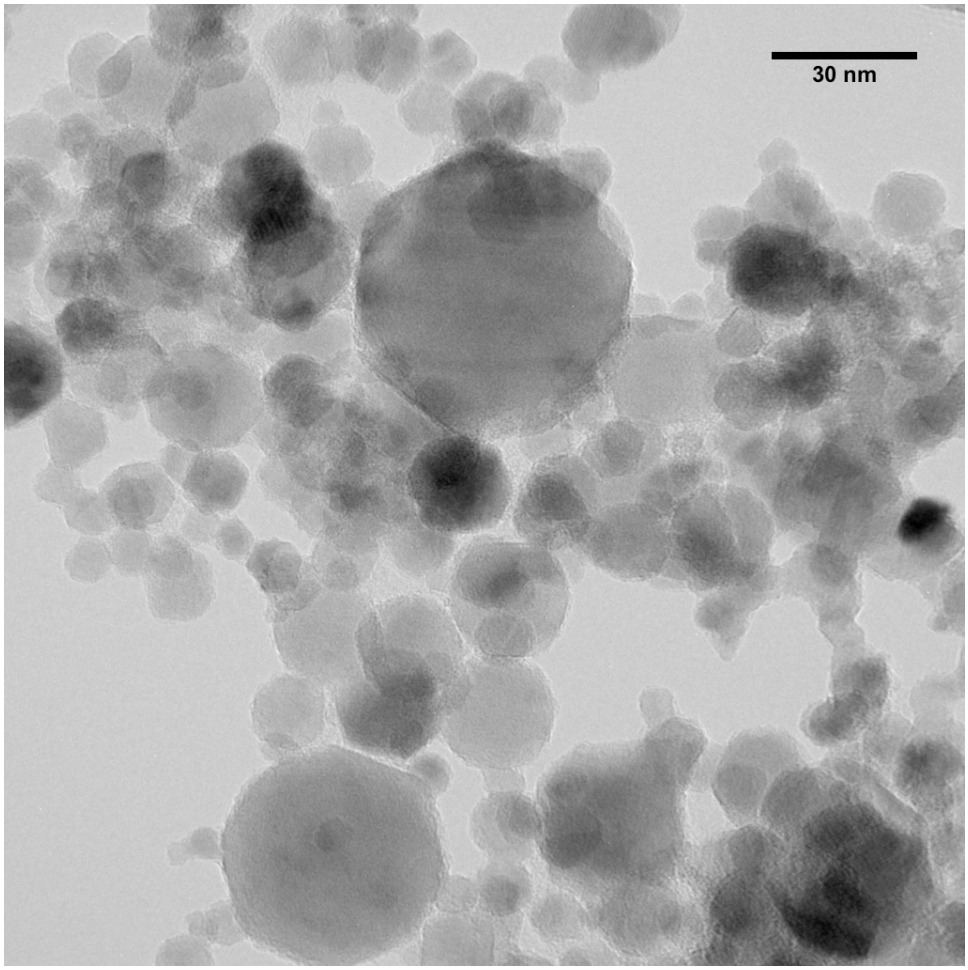

Figure 3-5. HRTEM showing specific weak agglomerate and APS < 30 nm

3.3.3.1. X-ray powder diffraction

XRD patterns for the as-processed samples are given in Figure 3-6. Figure 3-7 shows the relevant ICDD powder patterns for NiO, $NiO{\bullet}Al_2O_3$ and δ–Al_2O_3 and δ*-Al_2O_3 (44-1159, 10-0339, 46-1215 and 46-1131 respectively). Debye-Scherrer XRD line-broadening analyses give average particle sizes (APSs) consistent with the BET analyses (see Table 3-3). Samples with up to 5 mol % NiO show at most traces of crystalline $NiAl_2O_4$. These powders exhibit a blue cast that increases in intensity with increasing Ni^{2+} content associated with the

formation of inverse nickel spinel. As more NiO is added, the three main peaks at 37°, 45°, 66° 2θ for cubic spinel phase $NiO•Al_2O_3$ (ICDD 10-0339) gradually increase in intensity as $NiO•Al_2O_3$ spinel becomes the sole phase near the correct stoichiometry. At very high nickel contents of 63 and 78 mol % NiO, LF-FSP finally generates powders with mixed phases of $NiO•Al_2O_3$ and NiO.

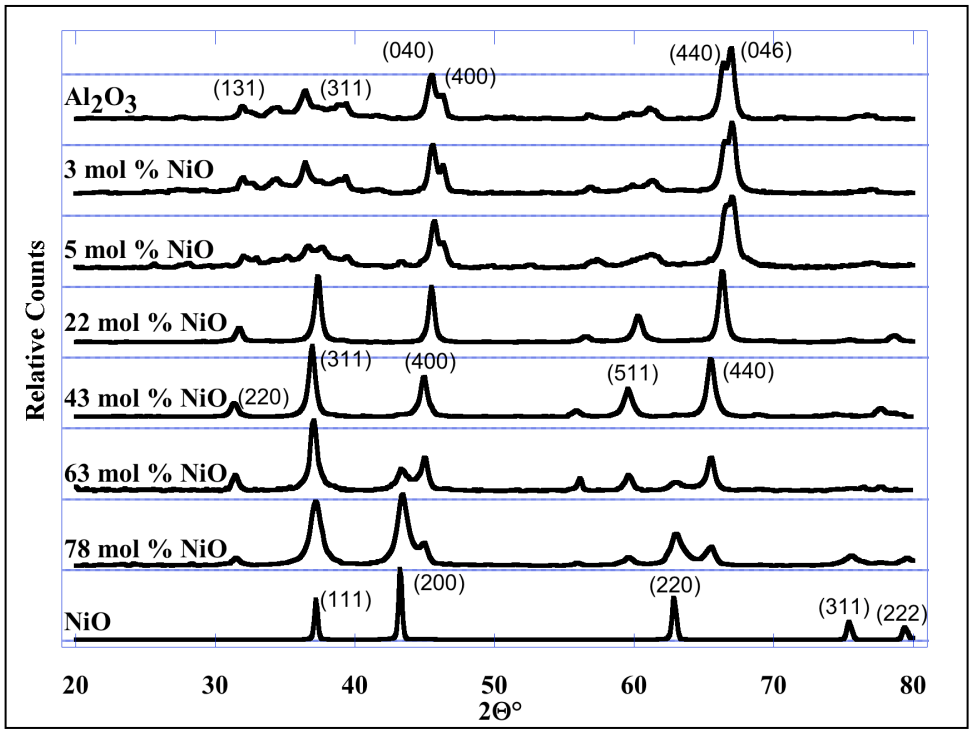

Figure 3-6. XRD patterns of all samples, showing the appearance of $NiO•Al_2O_3$

Sample 4, with 22 mol % NiO, does not exhibit the XRD powder pattern expected based on the phase diagram which is a mixture of corundum (α-alumina) and phase pure $NiO•Al_2O_3$, nickel spinel.[43] Initially, an experimental mistake in formulating the precursor might have caused this, making it closer to phase pure nickel spinel; however, chemical analyses by ICP and XRF were reproducible, as 22 mol % NiO. The use of a Si standard confirmed the unusual

0.4° 2θ shifts. Five separate samples were made at this composition to ensure reproducibly.

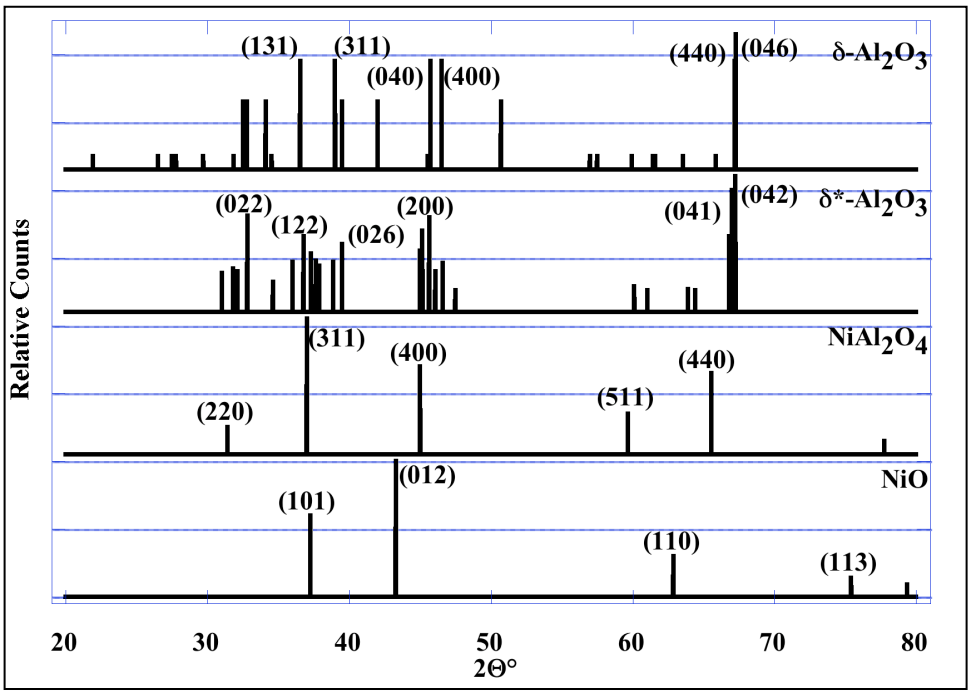

Figure 3-7. ICDD powder diffraction patterns for NiO, $NiAl_2O_4$ and Al_2O_3

Vegard's Law was used to calculate unit cell parameters for the Sample 4 materials (see experimental). By taking the pure species as the end compounds, Sample 4 (22 mol % NiO), with 37 mol % excess Al_2O_3 should have a cubic cell parameter of 0.7996 nm vs. 0.8011 nm found here. Thus this material exhibits a positive deviation from Vegard's Law.

Vegard's law is an empirical method of assessing the changes in unit cell parameters associated with vacancies in mixed-metal, metal-oxide and recently semiconductor materials. There are numerous ways to interpret this data, none of which appear to be completely satisfactory.[44-46] The simplest explanation is that the presence of Al^{3+} ions in positions normally filled by Ni^{2+} ions implies

that there are cation vacancies amidst the oxygen FCC lattice resulting in an electrostatic repulsion that leads to the somewhat larger unit cell parameters. However, this will require more work to confirm.

More interesting is the single phase present. According to Phillips et.al,[42] Sample 4: 22 mol % NiO should exhibit two phases, the spinel structure and α-Al_2O_3. Rietveld refinement (see Figure 3-8) of Sample 4 shows that indeed it is a single phase inverse spinel, with Al occupying all A sites and the B site have a 13% Ni and 87% Al occupancy. The formula for this material from crystallographic information gives rise $Al_{1.0}(Al_{1.74}Ni_{0.26})O_4$. Silicon 20 wt. % was added as internal standard accounting for a 103% recovery in the refinement. This is used to verify the position of the background trace to screen for phases that lack long-range order. Alumina and γ-Ni accounted for 87 wt. % (novel spinel phase) with an average crystallite size of 17 nm, an amorphous phase was detected and accounted for 13 wt. % of the sample. Furthermore, TGA-DTA studies designed to observe the expected phase segregation process did not lead to any observed changes in the XRD pattern after heating to 1400 °C, see below.

Thus, LF-FSP processing appears to offer access to a new stable inverse spinel along the NiO-Al_2O_3 tie-line. These results suggest that LF-FSP not only offers an excellent method of making high quality mixed-metal oxide nanopowders, it also offers the opportunity to create new phases (materials) or novel extensions of known phases.

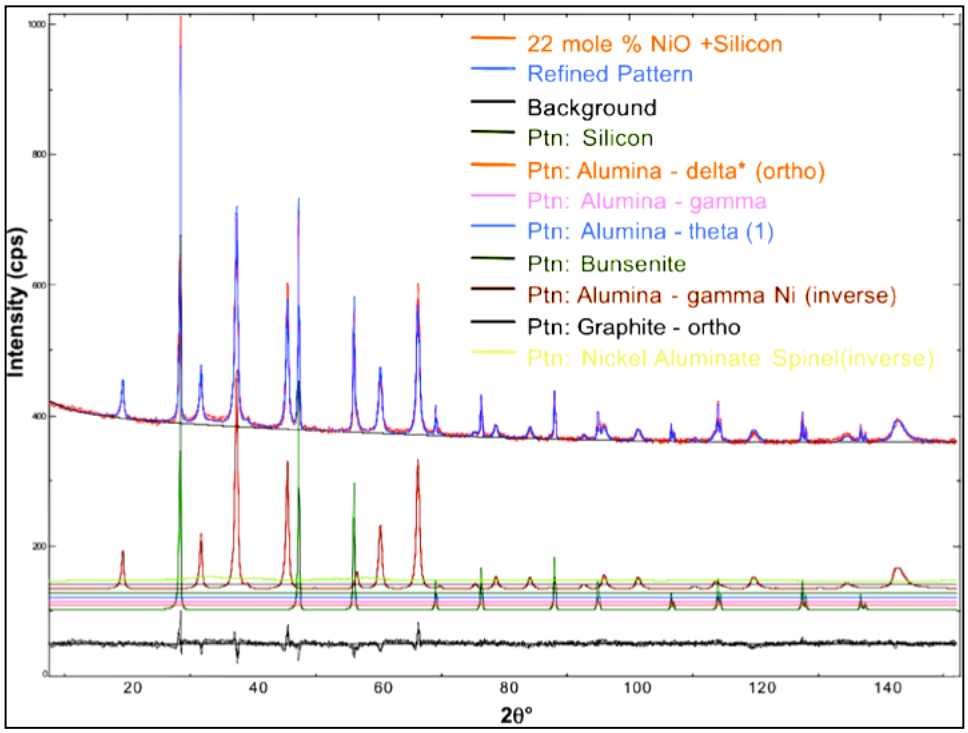

Figure 3-8. Rietveld refinement plot for sample 4

The most likely explanation for the formation of the new phase is that the high homogeneity of atomic mixing in the flame coupled with extremely fast formation and quenching of particles leads to unusual kinetic phases. However, atomic mixing in the flame is insufficient to produce high quality powders, the chemistry of the precursor is very important in the quality and type of nanopowder produced.[20-27]

3.3.3.2. Thermal gravimetric analyses

Thermo gravimetric analyses (TGA) of the eight as-prepared powders were run to determine the relative quantities of various surface species including physisorbed and chemisorbed water, carbonate species and possibly hydrocarbons synthesized perhaps by steam reforming during LF-FSP (see

FTIR data). All powders exhibit typical[20-27] 1-4 wt. % mass-losses over the 1200 °C range as seen in Figure 3-9.

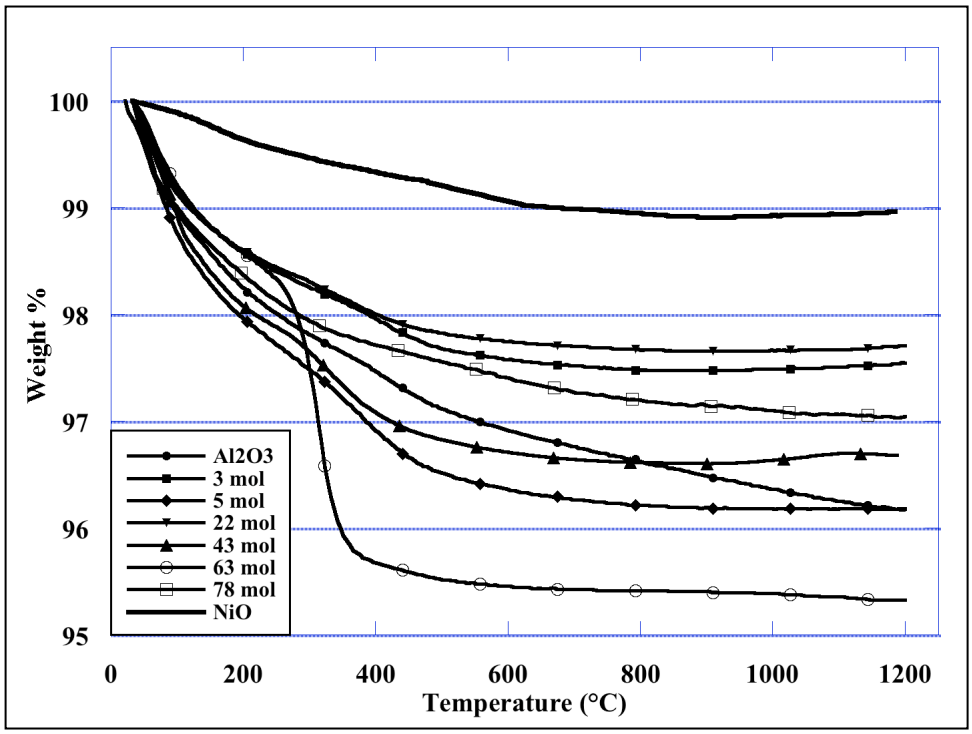

Figure 3-9. TGA traces of all samples

As noted above, nitrogen adsorption analyses do not indicate the presence of micro-porosity for any of the powders produced. One consequence of this is that they exhibit far less hydration than microporous powders.[24,47] The majority of this mass loss is due to thermal elimination of both physi- and chemisorbed water on the particle surfaces that arises from the combustion process. Likewise, smaller mass losses are in general attributed to loss of CO_2 from the surfaces of the powders entrained during combustion.

All samples behave very similarly with gradual mass losses over the 100 to 500 °C range that, within the error limits of the analysis of these high SSA powders, are all similar to pure δ-Al_2O_3. The two exceptions are Sample 8, pure

NiO, which has a relatively low SSA of 7 m^2/g and an associated mass loss of ≤ 1 wt. %, and Sample 6. At 63 mol % NiO, Sample 6 has the highest surface area per metal content and exhibits a distinct 3 wt. % mass loss at ≈ 300 °C. This may simply be a consequence of sample handling. However, there appear to be residual organic species (see FTIR below) for some of the higher NiO content samples that may result from steam reforming leading to hydrocarbon formation during LF-FSP. In pure δ-Al_2O_3 samples of the same SSA, no such peaks are observed for samples produced over a five-year period.

3.3.3.3. Differential thermal analyses

Differential thermal analyses (DTA) show no major phase transformations up to 1200 °C (see Figure 3-10).

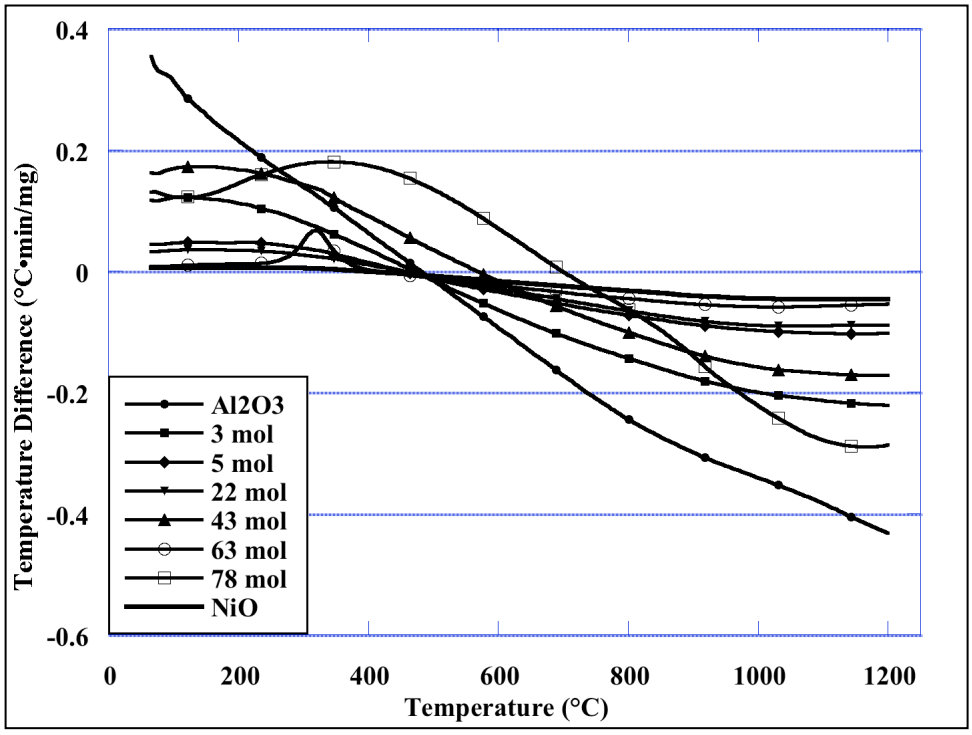

Figure 3-10. DTA traces for all samples

All sample traces show little variance, indicating the excellent thermal stability of considerable value for electrode and catalytic applications. Added NiO delays phase transformation to α-Al_2O_3 usually seen at ~ 1200 °C. Samples 4, 5 and 6 (22, 43 and 63 mol % NiO respectively) do not transform to α-Al_2O_3 even on heating to 1400 °C.

3.3.3.4. Fourier transform infrared spectroscopy

Diffuse reflectance infrared Fourier transform (DRIFT) spectra of as-prepared powders are presented in Figure 3-11. The spectra generally follow those observed for pure δ-Al_2O_3.

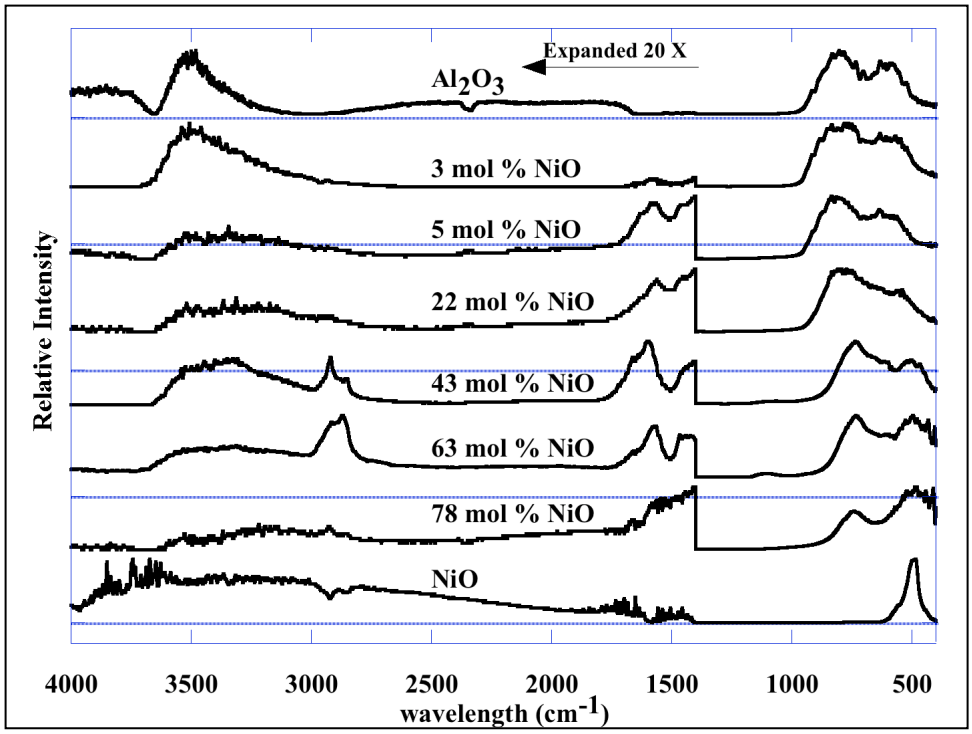

Figure 3-11. FTIR spectra of all samples.

In the 3900–2700 cm^{-1} region, weak νOH bands are observed, attributable to surface hydroxyls on alumina[48,49] arising from both physi- and chemi-sorbed water. In the 2900-2700 cm^{-1} region small νCH bands are observed primarily

for the 43 and 63 wt. % materials indicating some surface organic species. These bands are associated with a 2 % mass loss seen at > 300 °C for Sample 6. In the 1800–1200 cm^{-1} region, weak bands due to carbonate species[50] are observed again in accord with those seen for pure δ-Al_2O_3.[24] The 1000-400 bands are typical for νM-O band. δ-Al_2O_3 has two νAl-O bands at 810 and 610 cm^{-1}.[51] Nickel oxide has a well-defined νNi-O centered around 500 cm^{-1}.[52] Figure 3-11 shows a steady decline in the νAl-O band intensities and broadening and increase of the band attributed to νNi-O.

3.4. Conclusions

Liquid-feed flame spray pyrolysis offers the opportunity to produce mixed-metal oxide nanopowders with exceptional control of stoichiometry, phase and phase purity. LF-FSP also provides the potential to access entirely new phases heretofore not observed by standard catalyst and nanopowder synthesis techniques. LF-FSP provides access to materials with what appears to be atomic mixing within nanometer length scales. Prior to this work, this has proven to be very difficult to do for materials along the NiO-Al_2O_3 tie-line.[17-19] The probable explanation is that the thermal stability of the materials produced is so high (no phase transformations seen at 1400 °C) that once partially formed, further diffusion of atomic species is so slow that equilibration to thermodynamically favored phases is very slow without special heat treatments to very high temperatures. This then greatly reduces surface areas making the resulting materials of reduced value for catalyst applications. The addition of NiO reduces the final particle sizes for Al_2O_3 doped with up to 22 mol % NiO, considerably as evidenced by increases in SSAs by as much as 30% (from 60 to 80 m^2/g). The increase in SSA is likely a consequence of the higher thermal

stability of the solid that nucleates out of the gas phase during the rapid cooling in the LF-FSP process.

Because LF-FSP involves rapid quenching of the combustion species, it appears to offer access to new, kinetic phases not accessible by standard processing techniques. The observation of a new composition for an inverse spinel at $(NiO)_{0.22}(Al_2O_3)_{0.78}$ far outside the currently accepted stable spinel compositions for this system supports this idea. However, $NiO)_{0.22}(Al_2O_3)_{0.78}$ nanopowders are surprisingly robust and survive heating in air to 1400 °C where, based on the phase diagram,[51] this material might be expected to be metastable. As stated above, one might argue that the very high T_ms for these systems make it difficult if not impossible to actually reach thermodynamic equilibrium for these materials.

3.5. Bibliography

1. A. A. Lemonidou, M. A. Goula, I. A. Vasalos "Carbon Dioxide Reforming of Methane Over 5 Wt.% Nickel Calcium Aluminate Catalysts - Effect of Preparation Method," *Catal. Today,* 46 [2-3] 175-183 (1998).
2. L. B. Avdeeva, O. V. Goncharova, D. I. Kochubey, V. I. Zaikovskii, L. M. Plyasova, B. N. Novgorodov, S. K. Shaikhutdinov "Coprecipitated Ni-alumina and Ni-Cu-alumina Catalysts of Methane Decomposition and Carbon Deposition. II. Evolution of the Catalysts in Reaction," *Appl. Catal., A,* 141 [1-2] 117-129 (1996).
3. Y. Matsumura, T. Nakamori "Steam Reforming of Methane Over Nickel Catalysts At Low Reaction Temperature," *Appl. Catal., A,* 258 [1] 107-114 (2004).
4. M. Levent, D. J. Gunn, M. A. El-Bousiffi "Production of Hydrogen-Rich Gases From Steam Reforming of Methane in an Automatic Catalytic Microreactor," *Int. J. Hydrogen Energy,* 28 [9] 945-959 (2003).
5. S. Chokkaram, R. Srinivasan, D. R. Milburn, B. H. Davis "Conversion of 2-Octanol Over Nickel-alumina, Cobalt-alumina, and Alumina Catalysts," *J. Mol. Catal. A: Chem.,* 121 [2-3] 157-169 (1997).
6. P. Salagre, J. L. G. Fierro, F. Medina, J. E. Sueiras "Characterization of Nickel Species on Several γ-alumina Supported Nickel Samples," *J. Mol. Catal. A: Chem.,* 106 [1-2] 125-134 (1996).
7. J. C. Rodríguez, A. J. Marchi, A. Borgna, A. Monzón "Effect of Zn Content on Catalytic Activity and Physicochemical Properties of Ni-based Catalysts for Selective Hydrogenation of Acetylene," *J. Catal.,* 171 [1] 268-278 (1997).
8. S. Kaewpuang-Ngam, K. Inazu, T. Kobayashi, K.-I. Aika "Selective Wet-air Oxidation of Diluted Aqueous Ammonia Solutions Over Supported Ni Catalysts," *Water Res.,* 38 [3] 778-782 (2004).
9. A. Wijayasinghe, C. Lagergren, B. Bergman "New Cathode Materials for Molten Carbonate Fuel Cells," *Fuel Cells,* 2 [3-4] 181-188 (2002).
10. L. Kou, J. R. Selman "Electrical Conductivity and Chemical Diffusivity of $NiAl_2O_4$ Spinel Under Internal Reforming Fuel Cell Conditions," *J. Appl. Electrochem.,* 30 [12] 1433-1437 (2000).
11. Y. S. Han, J. B. Li, X. S. Ning, X. Z. Yang, B. Chi "Study on NiO Excess in Preparing $NiAl_2O_4$," *Mater. Sci. Eng. A,* 369 [1-2] 241-244 (2004).
12. C. Otero Areán, M. Peñarroya Mentruit, A. J. López López, J. B. Parra "High Surface Area Nickel Aluminate Spinels Prepared by a Sol-Gel Method," *Colloids Surf., A,* 180 [3] 253-258 (2001).
13. W. Schmidt, C. Weidenthaler "Nanosized Transition Metal Spinels With High Surface Areas From Zeolite Precursors," *Chem. Mater.,* 13 [2] 607-612 (2001).
14. P. Jeevanandam, Y. Koltypin, A. Gedanken "Preparation of Nanosized Nickel Aluminate Spinel by a Sonochemical Method," *Mater. Sci. Eng. B,* 90 125-132(8) (2002).
15. A. Mohammadpour, M., L. Torkian "Preparation of Nickel Aluminate Spinel By Microwave Heating," *Mater. Lett.,* 57 [3] 639-642 (2002).
16. F. Mariño, G. Baronetti, M. Jobbagy, M. Laborde "Cu-Ni-K γ-Al_2O_3 Supported Catalysts for Ethanol Steam Reforming: Formation of Hydrotalcite-type Compounds as a Result of Metal-support Interaction," *Appl. Catal., A,* 238 [1] 41-54 (2003).

17. Y. S. Han, J. B. Li, X. S. Ning, B. Chi "Effect of Preparation Temperature on the Lattice Parameter of Nickel Aluminate Spinel," *J. Am. Ceram. Soc.,* 87 [7] 1347-1349 (2004).
18. R. Subramanian, M. Higuchi, R. Dieckman "Growth of Nickel Aluminate Single Crystals By the Floating Zone Method," *J. Cryst. Growth,* 143 [3-4] 311-316 (1994).
19. R. F. Cooley, J. S. Reed " Equilibrium Cation Distribution in $NiAl_2O_4$ $CuAl_2O_4$ and $ZnAlO_4$ Spinels," *J. Am. Ceram. Soc.,* 55 [8] 395-398 (1972).
20. A. C. Sutorik, S. S. Neo, D. R. Treadwell, R. M. Laine "Synthesis of Ultrafine β"-alumina Powders via Flame Spray Pyrolysis of Polymeric Precursors," *J. Am. Ceram. Soc.,* 81 [6] 1477-1486 (1998).
21. J. C. Marchal, T. John, R. Baranwal, T. R. Hinklin, R. M. Laine "Yttrium Aluminum Garnet Nanopowders Produced by Liquid-Feed Flame Spray Pyrolysis (LF-FSP) of Metalloorganic Precursors," *Chem. Mater.,* 16 [5] 822-831 (2004).
22. R. Baranwal, M. P. Villar, R. Garcia, R. M. Laine "Flame Spray Pyrolysis of Precursors as a Route to Nano-Mullite Powder: Powder Characterization and Sintering Behavior," *J. Am. Ceram. Soc.,* 84 [5] 951-961 (2001).
23. S. Kim, J. Gislason, R. W. Morton, X. Q. Pan, H. P. Sun, R. M. Laine "Liquid-Feed Flame Spray Pyrolysis of Nanopowders in the Alumina-Titania System," *Chem. Mater.,* 16 [12] 2336-2343 (2004).
24. T. R. Hinklin, B. Toury, C. Gervais, F. Babonneau, J. Gislason, R. W. Morton, R. M. Laine "Liquid-Feed Flame Spray Pyrolysis of Metalloorganic and Inorganic Alumina Sources in the Production of Nanoalumina Powders," *Chem. Mater.,* 16 [1] 21-30 (2004).
25. C. R. Bickmore, K. F. Waldner, R. Baranwal, T. R. Hinklin, D. R. Treadwell, R. M. Laine "Ultrafine Titania by Flame Spray Pyrolysis of a Titanatrane Complex," *J. Eur. Ceram. Soc.,* 18 [4] 287-297 (1998).
26. K. F. Waldner, R. M. Laine, S. Dhumrongvaraporn, S. Tayaniphan, R. Narayanan "Synthesis of a Double Alkoxide Precursor to Spinel ($MgAl_2O_4$) Directly From $Al(OH)_3$, MgO, and Triethanolamine and Its Pyrolytic Transformation to Spinel," *Chem. Mater.,* 8 [12] 2850-2857 (1996).
27. R. M. Laine, J. C. Marchal, H. P. Sun, X. Q. Pan "A New $Y_3Al_5O_{12}$ Phase Produced by Liquid-feed Flame Spray Pyrolysis (LF-FSP)," *Adv. Mater.,* 17 [7] 830 (2005).
28. W. J. Stark, S. E. Pratsinis "Aerosol Flame Reactors for Manufacture of Nanoparticles," *Powder Technol.,* 126 [2] 103-108 (2002).
29. R. Strobel, F. Krumeich, W. J. Stark, S. E. Pratsinis, A. Baiker "Flame Spray Synthesis of Pd/Al_2O_3 Catalysts and Their Behavior in Enantioselective Hydrogenation," *J. Catal.,* 222 [2] 307-314 (2004).
30. M. Maris, T. Mallat, E. Orglmeister, A. Baiker "On the Role of Modifier Structure in the Palladium-Catalyzed Enantioselective Hydrogenation of Furan-2-Carboxylic Acid," *J. Mol. Catal. A: Chem.,* 219 [2] 371-376 (2004).
31. S. S. Ata-Allah, M. K. Fayek, H. S. Refai, M. F. Mostafa "Mössbauer Effect Study of Copper Containing Nickel-Aluminate Ferrite," *J. Solid State Chem.,* 149 [2] 434-442 (2000).
32. L. Li, G. Li, R. L. Smith, H. Inomata "Microstructural Evolution and Magnetic Properties of $NiFe_2O_4$ Nanocrystals Dispersed in Amorphous Silica," *Chem. Mater.,* 12 [12] 3705-3714 (2000).

33. Z. Wang, S. K. Saxena, P. Lazor, H. S. C. O'Neill "An in Situ Raman Spectroscopic Study of Pressure Induced Dissociation of Spinel $NiCr_2O_4$," *J. Phys. Chem. Solids,* 64 [3] 425-431 (2003).
34. M. A. Gabal "Non-isothermal Decomposition of NiC_2O_4-FeC_2O_4 Mixture Aiming At the Production of $NiFe_2O_4$," *J. Phys. Chem. Solids,* 64 [8] 1375-1385 (2003).
35. H. S. C. O'Neill, A. Navrotsky "Simple Spinels; Crystallographic Parameters, Cation Radii, Lattice Energies, and Cation Distribution," *Am. Mineral.,* 68 [1-2] 181-194 (1983).
36. H. S. C. O'Neill, A. Navrotsky "Cation Distributions and Thermodynamic Properties of Binary Spinel Solid Solutions," *Am. Mineral.,* 69 [7-8] 733-753 (1984).
37. A. N. Cormack, G. V. Lewis, S. C. Parker, C. R. A. Catlow "On the Cation Distribution of Spinels," *J. Phys. Chem. Solids,* 49 [1] 53-57 (1988).
38. V. V. Ivanov, V. M. Talanov, N. P. Shabelskaya "Phase Relations in the $NiFe_2O_4$-$NiCr_2O_4$-$CuCr_2O_4$ system," *Inorg. Mater.,* 37 839-845(7) (2001).
39. K. J. D. MacKenzie, C. M. Cardile "The Formation of Nickel Ferrite From Hematite, Magnetite and Spinel Ironsand," *Thermochim. Acta,* 165 [2] 207-222 (1990).
40. F. D. Rossini "Heats of Combustion and of Formation of the Normal Aliphatic Alcohols in the Gaseous and Liquid States, and the Energies of Their Atomic Linkages," *J. Res. NBS,* 13 189-197 (1934).
41. N. S. Bell, M. A. Rodriguez "Dispersion Properties of an Alumina Nanopowder Using Molecular, Polyelectrolyte, and Steric Stabilization," *J. Nanosci. Nanotechnol.,* 4 [3] 283-290 (2004).
42. B. Phillips, J. J. Hutta, I. Warshaw "Phase Equilibria in the System NiO-Al_2O_3-SiO_2," *J. Am. Ceram. Soc.,* 46 [12] 579-583 (1963).
43. V. A. Lubarda "On the Effective Lattice Parameter of Binary Alloys," *Mech. Mater.,* 35 [1-2] 53-68 (2003).
44. U. V. Chhaya, R. G. Kulkarni "Metal-Insulator Type Transition in Aluminium and Chromium Co-Substituted Nickel Ferrites," *Mater. Lett.,* 39 [2] 91-96 (1999).
45. T. Sano, Y. Tamaura "Synthesis of (Li,Mn) Ferrites by Reaction of Ultrafine γ-Fe_2O_3 with $LiMn_2O_4$ Spinel At 650 °C," *Mater. Res. Bull.,* 34 [3] 389-401 (1999).
46. J. M. McHale, A. Navrotsky, A. J. Perrotta "Effects of Increased Surface Area and Chemisorbed H_2O on the Relative Stability of Nanocrystalline γ-Al_2O_3 and α-Al_2O_3," *J. Phys. Chem. B,* 101 [4] 603-613 (1997).
47. D. H. Lee, R. A. Condrate "An FTIR Spectral Investigation of the Structural Species Found on Alumina Surfaces," *Mater. Lett.,* 23 [4-6] 241-246 (1995).
48. J. M. Saniger "Al-O Infrared Vibrational Frequencies of γ-alumina," *Mater. Lett.,* 22 [1-2] 109-113 (1995).
49. A. Fischer, T. Mallat, A. Baiker "Nickel-Catalyzed Amination of 1,3-Propanediols Differently Substituted At C2-position: Influence of Reactant Structure on Diamine Production," *J. Mol. Catal. A: Chem.,* 149 [1-2] 197-204 (1999).
50. A. Surca, B. Orel, B. Pihlar, P. Bukovec "Optical, Spectroelectrochemical and Structural Properties of Sol-Gel Derived Ni-oxide Electrochromic Film," *J. Electroanal. Chem.,* 408 [1-2] 83-100 (1996).
51. P. Tarte "Infra-Red Spectra of Inorganic Aluminates and Characteristic Vibrational Frequencies of AlO_4 Tetrahedra and AlO_6 Octahedra," *Spectrochim. Acta A-M,* 23 [7] 2127-2143 (1967).

52. V. Biju, K. Abdul, M. "Fourier Transform Infrared Spectroscopy Study of Nanostructured Nickel Oxide," *Spectrochim. Acta A-M,* 59 [1] 121-134 (2003).

Chapter 4.

Synthesis and Characterization of Mixed-Metal Oxide Nanopowders Along the Co_3O_4-Al_2O_3 Tie-Line

4.1. Introduction

Cobalt oxides are used as catalysts for hydrocracking fuels,[1] in several selected and complete oxidation processes,[2,3] as well as in steam reforming of ethanol.[4] Co_3O_4 shows good catalytic activity for the low temperature combustion of CO and organics.[5] At higher temperatures, the catalyst becomes reducing, converting CO_2 to CO and O_2 without a reducing reagent.[6]

Supported cobalt is often a co-catalyst for hydrocracking waste gases and contaminated fluids[7] to innocuous gases and NO_x. Traditional *de-NO_x* catalysts usually contain one of several very expensive metals including Pd, Pt, Rh and Ru.[8,9] Supported cobalt systems offer considerable potential as low-cost, selective alternatives to noble metal based materials, for catalytic reduction of NO_x.[10-12]

Cobalt has also been used since prehistoric times as a component in many pigments, particularly for deep blues.[13,14] Typical pigments consist of spinel or olivine phases produced from mixtures of cobalt and SiO_2, ZrO, TiO_2, or Al_2O_3.[15,16] There continues to be considerable active research on cobalt pigment technology to optimize color hues and luminescent properties.[17-19] Cobalt containing powders are also being used in high-end optical filters and magnetic recording media.[20,21]

The literature is replete with synthetic routes to cobalt oxides, and cobalt containing materials especially for compositions along the CoO_x-Al_2O_3 tie-line. The standard method is via solid state reaction of the parent oxides. Other synthesis methods include sol-gel,[22,23] co-precipitation,[24,25] hydrothermal,[26] polymeric precursor[27] and vapor deposition processing.[28]

This chapter demonstrates the use of liquid-feed flame spray pyrolysis (LF-FSP) to systematically produce compositions along the CoO_x-Al_2O_3 tie-line. Spray pyrolysis techniques are well-known and described extensively in literature, and have been used to synthesize simple and complex oxide powders.[29-33] The advantage of LF-FSP over other techniques is that it allows production of up to 15 different compositions in the time span of a single week. This chapter discusses the development of materials with novel phase composition of potential interest to the catalyst and pigment industries.

4.2. Experimental

4.2.1. Materials

Cobalt nitrate hexahydrate [$Co(NO_3)_2 \bullet 6H_2O$, 99.97%], propionic acid [$CH_3CH_2CO_2H$, 99$^+$%], triethanolamine [$N(CH_2CH_2OH)_3$ 98%] and anhydrous ethanol [CH_3CH_2OH, 99$^+$%] were purchased from Alfa Aesar and used as received. Aluminum tris(sec-butoxide), [$Al(OsBu)_3$, 97%] was purchased from Chattem Chemical Co. and also used as received.

4.2.2. Precursor formulations

Cost effective precursors to produce nine different nanopowder samples with compositions along the CoO_x-Al_2O_3 tie-line were synthesized and characterized in terms of their ceramic yield and composition.

4.2.2.1. Aluminum precursor

Alumatrane was synthesized from $Al(OsBu)_3$ and $N(CH_2CH_2OH)_3$ as described elsewhere,[34] then diluted with EtOH to produce ~6 L of solution with a ceramic loading of 21 wt. % by TGA.

4.2.2.2. Cobalt precursor

Cobalt propionate was prepared by adding 200.0 g (0.687 mole) of $Co(NO_3)_2 \cdot 6H_2O$ crystals to a 500 mL flask equipped with a still head and an N_2 sparge. Propionic acid (400 mL, 5.36 moles) was added and the resulting solution heated to ~150 °C for 6 h to distill off ~140 mL of liquid (water/propionic acid) and coincidentally remove NO_x gas. The remaining liquid product was placed in a clean 500 mL Nalgene® bottle. The ceramic loading of the solution was determined by TGA to be 3.3 wt. %. I did not further identity this precursor because it is very volatile and coated our TGA instrument, reacting rapidly with any exposed Al_2O_3 forming a cobalt aluminate spinel.

4.2.3. Specific analytical methods

Elemental analysis using X-Ray Fluorescence (XRF) was performed on all samples. Bombarding with high-energy X-rays generates emission of characteristic elemental "secondary" (or fluorescent) X-rays, which is accurate to ppm levels. The samples were prepared by mixing 0.50 g of sample into 10.0 g of $Li_2B_4O_7$ glass flux. The sample and glass flux were mechanically stirred for 5 minutes in a methacrylate vial with three methacrylate balls using a SPEX 6000 ball mill (SPEX CertiPrep, Metuchen, NJ). The mixtures were fused into glass beads by placing them in an oven

held at 1000 °C for 10 min. The samples were analyzed using a Panalytical PW2400 X-Ray Fluorescence spectrometer (formerly Philips), equipped with a WDS detection system (wavelength dispersive).

4.3. Results and discussion

The materials along the Co_3O_4-Al_2O_3 tie-line, produced in a single-step process, offer advantages over more conventionally prepared materials because LF-FSP provides access to phase compositions that are otherwise hard or impossible to attain. This method is extremely versatile allowing combinatorial alterations of compositions with minimal effort and precise control. Thus, it is possible to produce 40 g samples of 15 different compositions in roughly 5 days or more samples with smaller sample sizes.

All samples exhibit relatively high specific surface areas (SSAs), have no microporosity (from T-plot analyses and TEM micrographs) and have spherical morphologies. These and other properties make them excellent candidates for catalytic or pigment applications.

A discussion on the formulation of the precursors and nanopowder production follows. Particle morphology is then discussed in terms of specific surface areas, morphologies, size and surface species using a variety of characterization methods.

4.3.1. Precursor Formulations

Nine different precursor formulations (see Table 4-1) were used to produce nanopowders along the CoO_x-Al_2O_3 tie line. Precise amounts of alumatrane and cobalt propionate solutions were diluted in ethanol and stirred mechanically prior to use for LF-FSP processing. Solutions used to produce the powders contained 2-4 wt. % ceramic in precursor form by thermogravimetric analysis (TGA), to minimize

rheological complications with the LF-FSP process. The compositions produced are listed in Table 4-1. Forty g samples of all powders at 30-180 g/h rates were produced. XRF was used to obtain elemental analyses of selected samples and the results showed that the compositions were within experimental error of the precursor compositions.

Table 4-1. Precursor compositions

Sample	Mol % Co ± 1.0 %
1	0
2	4
3	8
4	21
5	37
6	50
7	87
8	94
9	100

4.3.2. Powder characterization.

4.3.2.1. Surface area analyses

Specific surface areas (SSAs) of all as-produced samples are shown in Figure 4-1. The SSAs clearly decrease towards the CoO_x rich end of the tie-line, with the exception of the cobalt oxide powder (Co_3O_4). This decrease appears coincident with formation of cobalt spinel phase resulting as Co^{2+} ions are incorporated into the A sites of the spinel structure. The increase in surface area of the last sample results from the oxidation of CoO to Co_3O_4. This change in oxidation state causes a change of phase in the material that brings with it an intrinsic increase in SSA. No microporosity was expected nor detected in any of the samples.

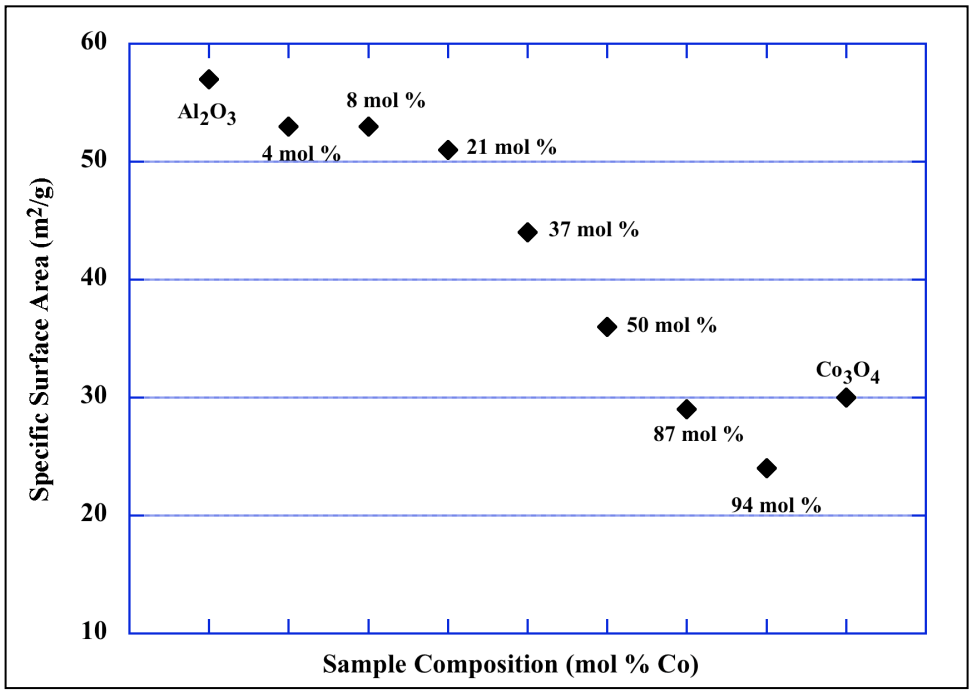

Figure 4-1. Specific surface areas of all powder samples

The average particle sizes were estimated from the SSAs and the theoretical density of the powders, and compared to values obtained by Debye-Scherrer XRD peak-broadening analyses.

Table 4-2. APS from BET and XRD data

Sample	Mol % Co	BET APS (nm) ± 1	XRD APS (nm) ±2
1	Al_2O_3	29	29
2	4%	31	18
3	8%	30	21
4	21%	30	20
5	37%	32	19
6	50%	38	22
7	87%	35	21
8	94%	40	22
9	100%	32	20

The theoretical densities where calculated using the known values of the end members and middle composition of the tie-line, (Al_2O_3, $CoAl_2O_4$ and Co_3O_4)

and interpolating using compositions in mole percent for the various samples. Particle sizes obtained by Debye-Scherrer peak-broadening differ somewhat from those calculated from BET calculations (see Table 4-2). Average particle size values from peak-broadening technique are lower by ~10 to 20 nm, this is possibly due to a difference in actual vs. theoretical densities of the powder, except for the value of pure Al_2O_3 which corresponds well with the value calculated from SSA. The APS of all powders is <40 nm regardless of the technique used to calculate the value, and remains relatively constant for all compositions studied.

4.3.2.2. Scanning electron microscopy

Scanning Electron Micrographs (SEMs) of all samples provide an understanding of particle morphology. Figure 4-3 shows a SEM of the 4 mol % Co sample, which is representative of all other samples. The powders exhibit spherical morphologies throughout and the images suggest relatively narrow particle size distributions. The SEMs show a few particles in the 100–150 nm range and some agglomerates formed via electrostatic interactions. Figure 4-3 shows the 100 mol % Co sample taken at low magnification to provide an overview of the general particle population. This image allows one to conclude that no micron size particles are produced during LF-FSP of these materials.

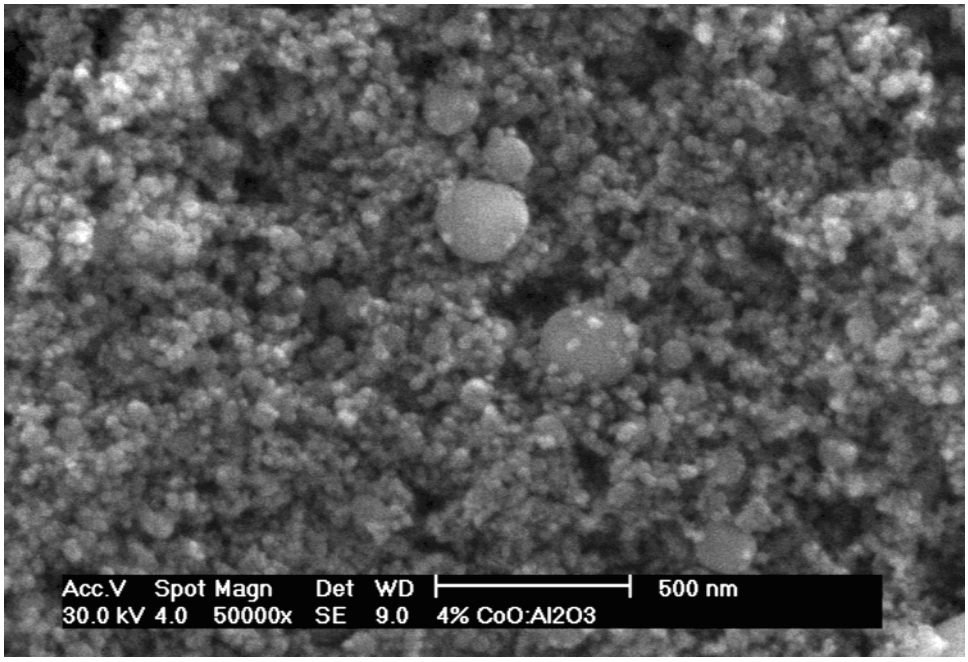

Figure 4-2. Hi magnification of the 4 mol % Co sample

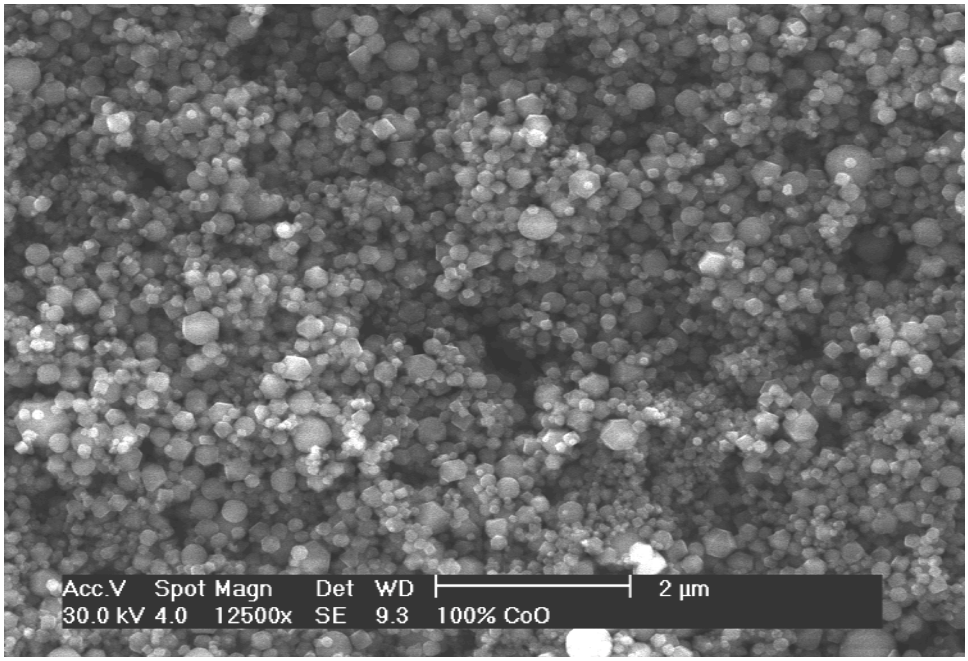

Figure 4-3. SEMs showing homogenous morphology and narrow particle distribution

4.3.2.3. Transmission electron microscopy

Figure 4-4 and Figure 4-5 are transmission electron micrographs (TEMs) from the 8 and 87 mol % Co samples respectively. Most of the particles are spherical and well below 80 nm in diameter with the vast majority <30 nm. Note the change in morphology, which is mostly faceted and spherical for the 8 mol % sample (Figure 4-4), while nearly all of particles in the 87 mol % sample (Figure 4-5) appear rhombic. This is attributed to the formation of the highly crystalline spinel phase coincident with increases in Co content. Particle necks, while occasionally visible in the 8 mol % sample, are not a major morphological feature.

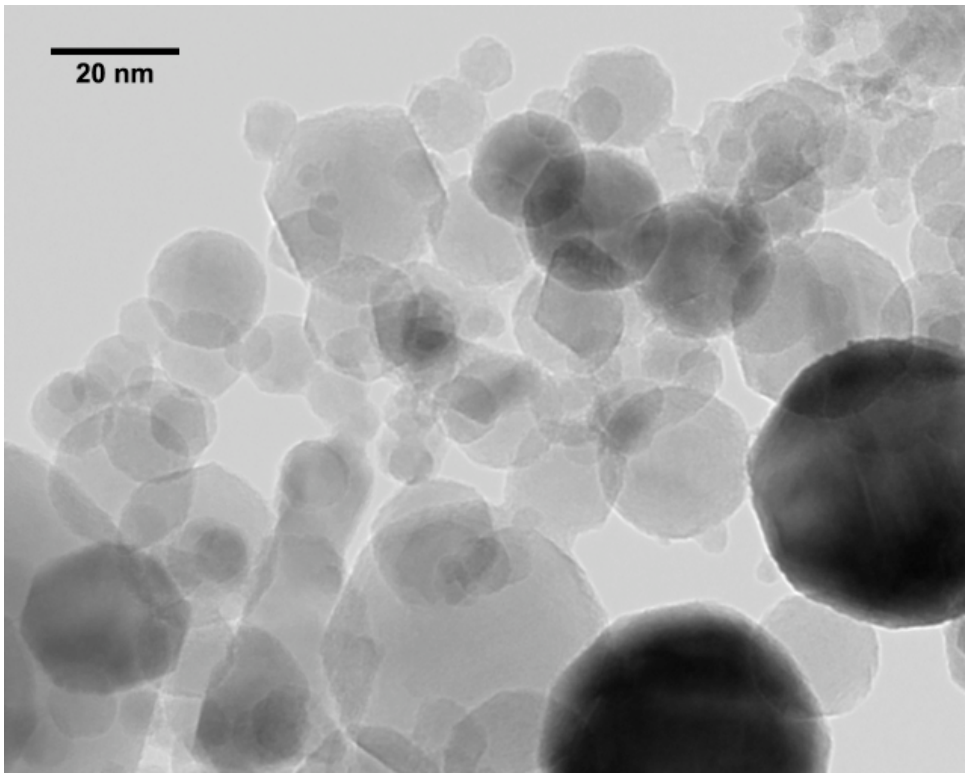

Figure 4-4. TEM micrograph for 8 mol % Co sample, spherical particles

All samples prepared here consist primarily of soft agglomerates created during dispersion or from the strong electrostatic interactions which particles

this size exhibit. There is no evidence for any microporosity, as expected from the t-plot results and surface area analyses.

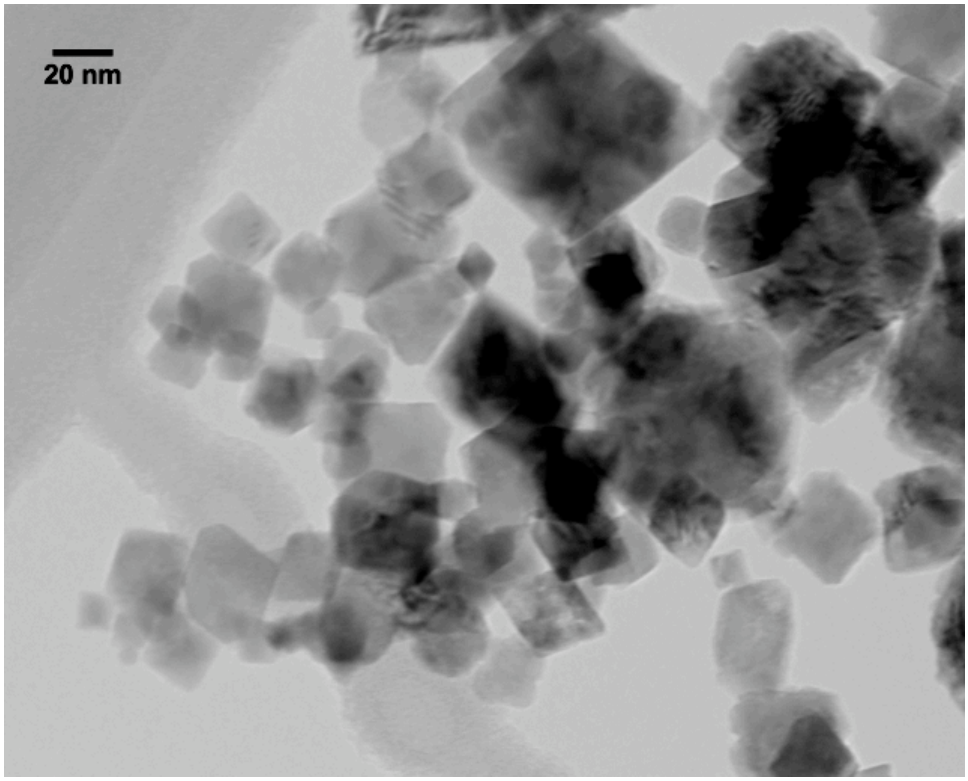

Figure 4-5. TEM micrograph for 87 mol % Co sample, cubic particles

4.3.2.4. X-ray powder diffraction

Figure 4-6 shows the published phase diagram marked with the compositions of this study.[35] The stable phases that are expected to form at these compositions can be determined from the diagram, but the XRD results suggest phases outside the phase boundaries.

XRD patterns for all samples are presented in Figure 4-7. The phase composition changes gradually from δ-Al_2O_3 through the spinel phase to Co_3O_4. The 4 mol % Co sample shows no trace of any Co containing crystalline phase,

thus all of the Co^{3+} seems to substitute for Al^{3+} ions in the δ-Al_2O_3 lattice as expected based on our studies on rare earth doped δ-Al_2O_3.[34]

Samples with higher Co contents exhibit powder patterns corresponding to formation of $CoAl_2O_4$ spinel. These broad peaks first appear at 21 mol % Co and give way to sharper, better-defined peaks as the correct stoichiometry is reached.

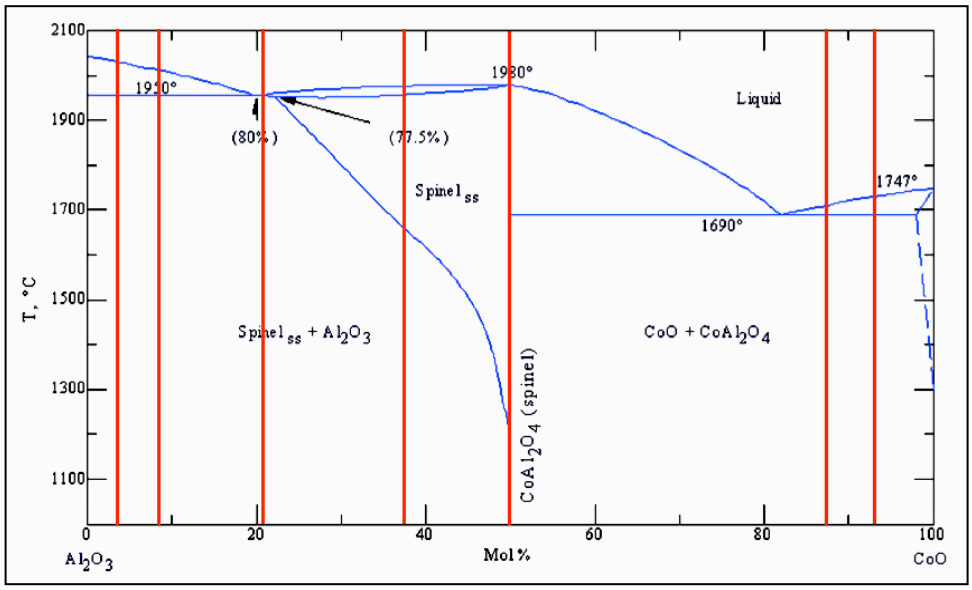

Figure 4-6. Sample compositions marked on the Al_2O_3-CoO phase diagram [35]

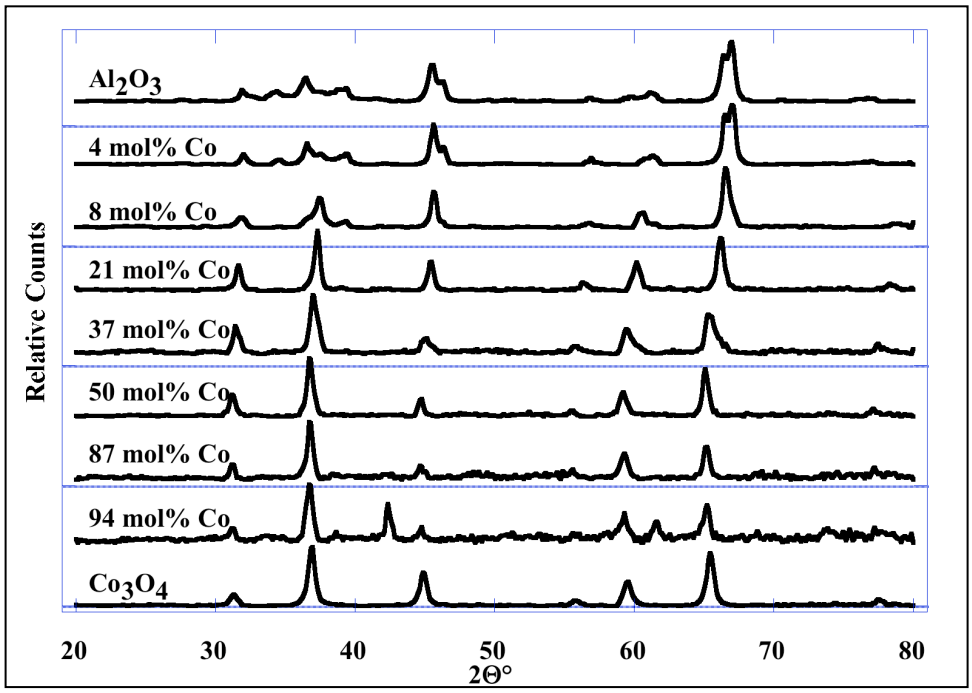

Figure 4-7. XRD patterns of all as-prepared samples

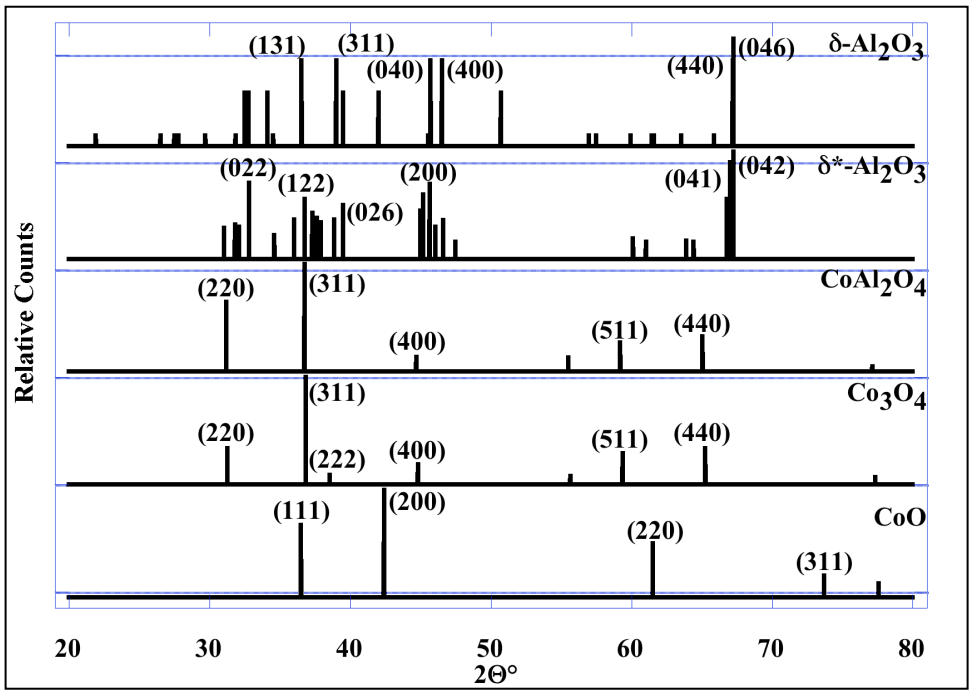

Figure 4-8. Relevant ICDD files for the CoO_x-Al_2O_3 system

Stoichiometric cobalt aluminate shows a phase pure pattern, (ICDD ref.: 44-0160) indicative of the capabilities of LF-FSP. The formation of off-

stoichiometric spinels (21 and 37 mol % samples) is believed to result from the extremely fast quench that these materials undergo in the LF-FSP apparatus. The shifts in the peak positions are indicative of a change in lattice cell parameters, however in order to determine the exact atom positions in these materials further cell refinement studies are required and left for other researchers.

In the 87 mol % Co sample, a CoO phase is detected as the excess Co^{3+} ions have no more sites to replace in the spinel structure. This phase is evident by a shift to higher 2θ°(~0.8θ°) in the 220 reflection, and the emergence of a shoulder on the 400 reflection of $CoAl_2O_4$ and Co_3O_4. In the 97 mol % sample the CoO phase is clearly evident by the emergence of the CoO 200 reflection (~42° 2θ) and the 220 reflection (~62° 2θ).

The 94 mol % Co sample consists of a mixture of two phases, spinel $CoAl_2O_4$ and cubic CoO, as expected based on the elemental composition for this samples and the phase diagram.[35] The pure cobalt oxide XRD corresponds to Co_3O_4, which has a spinel structure from the ICDD card. The thermodynamically expected cubic CoO is not observed because the particular conditions in the LF-FSP syntheses process did not sustain temperatures in excess of 1750 °C that are required to form the thermodynamic CoO, the relatively lower temperatures favor the formation of Co_3O_4.

4.3.2.5. Thermal gravimetric analyses

TGAs were performed on all as-prepared samples to determine the relative amounts of adsorbed surface species (H_2O and carbonate species) and thermal

behavior. The 87, 94 mol % Co and Co_3O_4 show no mass loss events below ~900 °C. At this temperature these materials exhibit a sharp mass loss event that can be attributed to decomposition from Co_3O_4 to CoO:

$$2Co_3O_4 \rightarrow 6CoO + O_2 \qquad (1)$$

The theoretical mass loss for such a reaction is 6.64 %, the observed losses are 6.13, 6.02 and 6.09 respectively for the 87, 94 mol % Co and Co_3O_4. These values are within the error limits of the analysis, given that they contain some CoO (see XRD analyses). The Co_3O_4 end member exhibits the sharpest mass loss event, which broadens at lower Co contents. One possible explanation is that oxygen is more tightly bound to nanopowders with some $CoAl_2O_4$ spinel phase present, although this was not confirmed here.

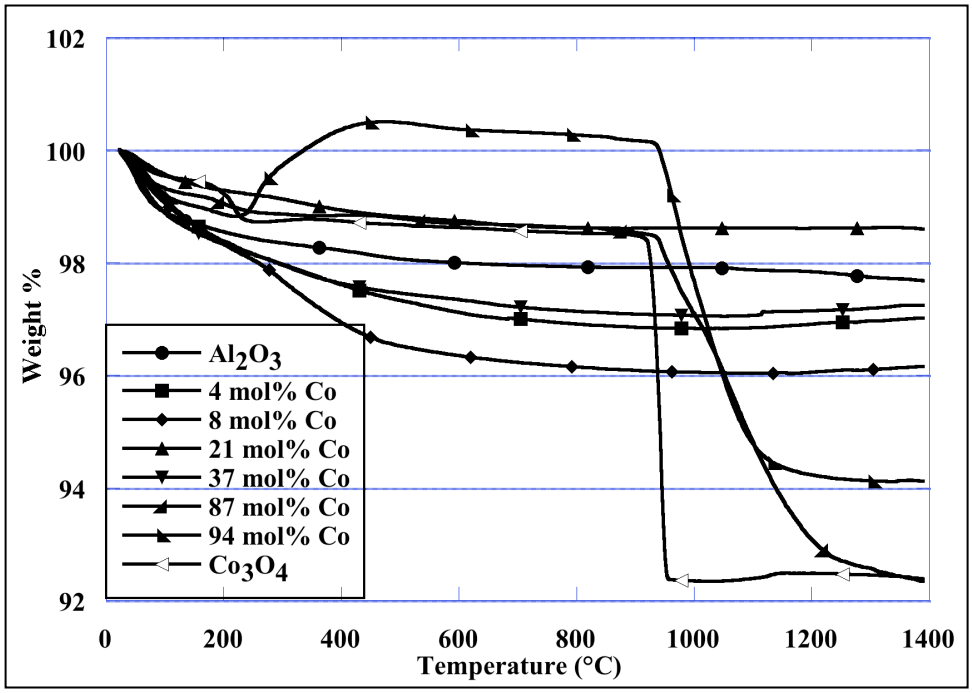

Figure 4-9. TGAs (10 °C/min, 60mL/min in air) for all as-prepared samples

There is a small mass increase (0.5 wt. %) between 240 and 450 °C in the 94 mol % Co sample, this increase is believed to result from oxidation of some

CoO to Co_3O_4. Such an oxidation might be expected for Co^{2+} ions substituted for octahedral Co^{3+} ions in the as-prepared material. These ions occupy traditional "B" sites in spinels that require a 3^+ charge to be stoichiometric.

The other 5 samples (low Co content) exhibit typical 1-4 % mass losses (for nanopowders produced via LF-FSP) over the 1400 °C range. This loss is expected and associated with loss of physi-and chemi-sorbed water resulting from the combustion process and atmosphere due to their relatively high surface areas, although they exhibit far less hydration than microporous powders.[36] The only sample that has a sharp mass loss event is Co_3O_4 at ~250 °C, this event can be associated with loss of carbonates.[33] Diffuse reflectance infrared Fourier transform (DRIFTS) data discussed below, confirms the presence of these organic species.

4.3.2.6. Fourier transform infrared spectroscopy

DRIFTS for all samples are presented in Figure 4-10. All spectra above 1200 cm^{-1} were normalized by taking the highest count in this range of any particular spectrum and normalizing this value to 1, this is done so that a fair comparison can be made among all spectra.

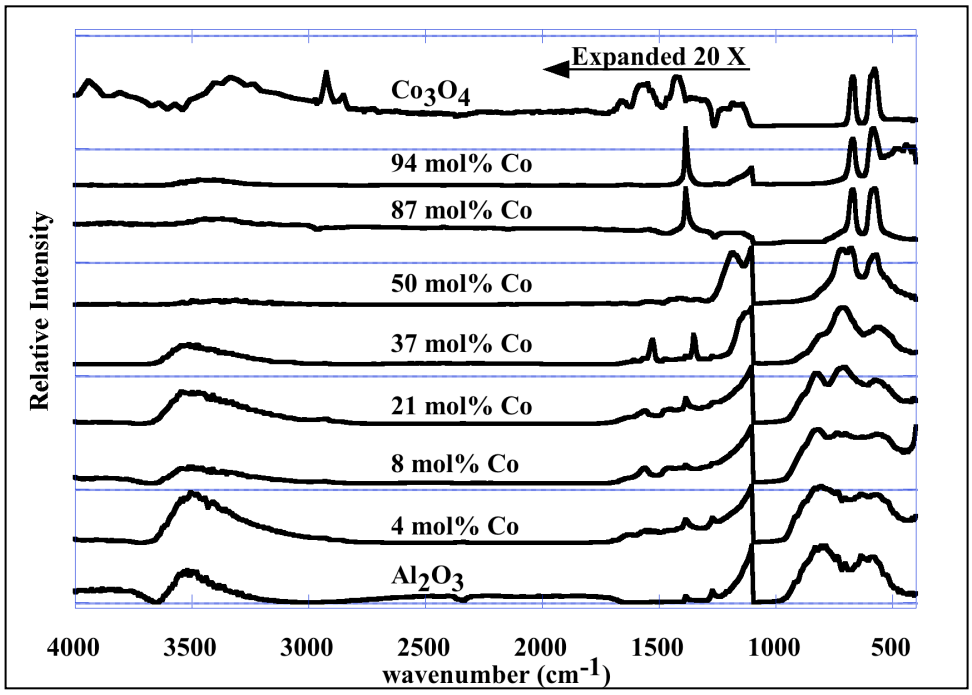

Figure 4-10. Full FTIR spectra of all as-prepared samples

There are two main regions of interest, 4000 to 2800 cm^{-1} and 1100 to 400 cm^{-1}. The first region, expanded in Figure 4-11, reveals a series of overlapping ν-OH bands arising from both physi- and chemi-sorbed water. The higher ν-OH vibrations (3700–3200 cm^{-1}) are typical of overlapping hydroxyl groups on alumina surfaces.[37,38] There are no sharp peaks in this region only broad bands. Furthermore, the ν-OH bands fall off with increases in Co content suggesting that the surface hydroxyls are only associated with the alumina species. With the exception of cobalt oxide, no significant organic species are observed as evidenced by the absence of νC-H bands in the 2900–2700 cm^{-1} region. These bands are associated with a 2 % mass loss seen at > 250 °C in the TGA trace and could be a result incomplete combustion of the precursor. However, this seems unlikely as they are not normally observed in any other nanopowders

previously made and may be better explained as resulting from some steam reforming in the flame. But this conclusion remains speculative.

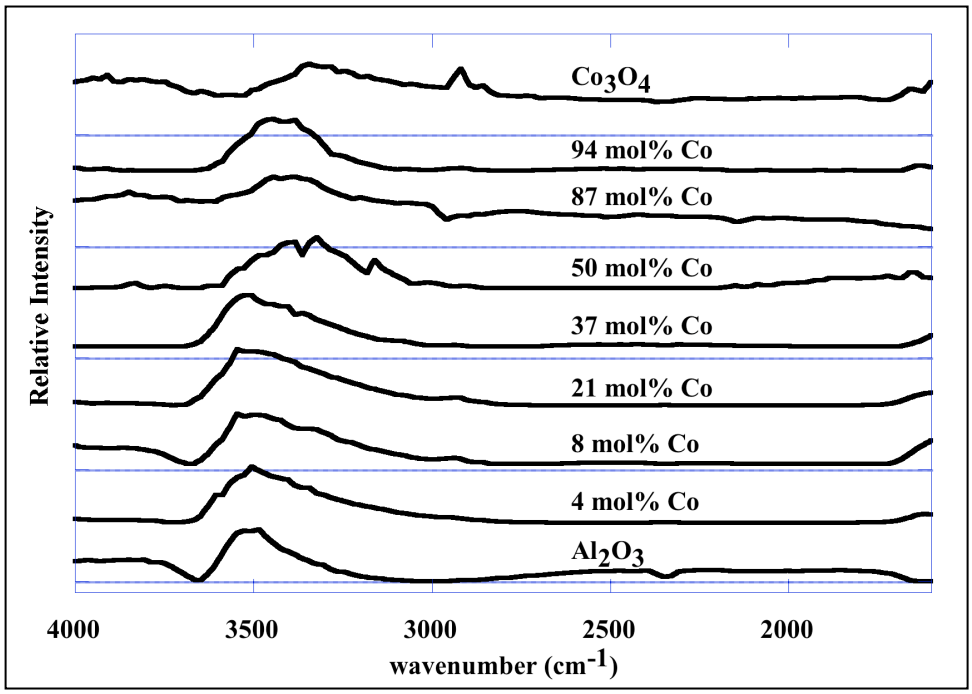

Figure 4-11. FTIR spectra of all samples in the 4000–1600 cm^{-1} region

The lower wavenumber region exhibits typical νM-O bands. Delta alumina has two νAl-O bands at 810 and 610 cm^{-1},[39] associated with the tetrahedral and octahedral Al-O vibrations respectively. Cobalt oxide (Co_3O_4) has two well-defined νM-O bands, 690 cm^{-1} and 605 cm^{-1},[40] which can emerge clearly in the higher Co content samples. These sharp bands become visible in the sample 87 mol % Co, and are associated with the high degree of crystallinity of these samples.

4.4. Conclusions

Liquid-feed flame spray pyrolysis offers the opportunity to produce mixed-metal oxide nanopowders with exceptional control of stoichiometry, phase and phase purity.

This chapter demonstrates the use of LF-FSP to systematically produce a series of nine powders along the CoO_x-Al_2O_3 tie-line with well-defined stoichiometries. The precursors used to synthesize these nanopowders are inexpensive and easily made.

The addition of CoO to Al_2O_3 reduces the SSAs by as much as 65% (from 60 to 20 m^2/g), likely as a consequence of the formation of the cobalt spinel phase. Primary crystallite sizes (from XRD data) vary very little, the BET derived APS values are slightly higher most likely because of miscalculations in the true particle densities. The unexpected SSA increase observed for the end-member cobalt oxide is attributed to the formation of Co_3O_4 instead of CoO. The most probable explanation for this result is that the excess oxygen favors the formation of Co^{3+} which in turn, favors the formation of a spinel ($Co^{2+}{}_1Co^{3+}{}_2O_4$) structure. A cobalt aluminate was also detected, spinel phases that should only stable at high temperatures, but these are meta-stable at lower temperatures. Therefore I can conclude that LF-FSP appears to offer access kinetic phases rather than thermodynamic phases accessible by standard processing techniques.

For the most part TGA and FTIR studies provide results that correspond to typical nanopowders produced via LF-FSP. These materials exhibit typical 1-4 % mass losses over the 1400 °C range, with only physi- and chemisorbed water as a surface species. Carbonate species have also been detected on surfaces of these materials, the Co_3O_4 sample, with a mass loss event at ~250 °C can be attributed to either CO_2 or CO_3^{2-}. There is a sharp mass loss event of the high cobalt content samples that is attributed to the decomposition of Co_3O_4 to CoO, although speculative and may be left as a question for future studies or other scientists. Likewise the oxidation or mass gain of the 94 mol % sample is only the most reasonable explanation of my observations.

4.5. Bibliography

1. C. O. Arean, M. P. Mentruit, E. E. Platero, F. X. L. Xamena, J. B. Parra "Sol-Gel Method for Preparing High Surface Area $CoAl_2O_4$ and Al_2O_3-$CoAl_2O_4$ Spinels," *Mater. Lett.,* 39 22-27 (1999).
2. L. B. Backman, A. Rautiainen, M. Lindblad, A. O. I. Krause "Effect of Support and Calcination on the Properties of Cobalt Catalysts Prepared by Gas Phase Deposition," *Appl. Catal., A,* 191 [1-2] 55-68 (2000).
3. Z.-Z. Chen, E.-W. Shi, W.-J. Li, Y.-Q. Zheng, J.-Y. Zhuang, B. Xiao, L.-A. Tang "Preparation of Nanosized Cobalt Aluminate Powders by a Hydrothermal Method," *Mater. Sci. Eng. B,* 107 [2] 217-223 (2004).
4. Z. Z. Chen, E. W. Shi, W. J. Li, Y. Q. Zheng, W. Z. Zhong "Hydrothermal Synthesis and Optical Property of Nano-Sized $CoAl_2O_4$ Pigment," *Mater. Lett.,* 55 [5] 281-284 (2002).
5. W.-S. Cho, M. Kakihana "Crystallization of Ceramic Pigment $CoAl_2O_4$ Nanocrystals From Co-Al Metal Organic Precursor," *J. Alloys Compd.,* 287 [1-2] 87-90 (1999).
6. S. Chokkaram, R. Srinivasan, D. R. Milburn, B. H. Davis "Conversion of 2-Octanol Over Nickel-alumina, Cobalt-alumina, and Alumina Catalysts," *J. Mol. Catal. A: Chem.,* 121 157-169 (1997).
7. P. Colomban "Lapis Lazuli as Unexpected Blue Pigment in Iranian Lajvardina Ceramics," *J. Raman Spectrosc.,* 34 [6] 420–423 (2003).
8. S. Djambazov, Y. Ivanova, A. Yoleva, N. Nedelchev "Ceramic Pigments on the Base of the CoO-ZnO-SiO_2 System Obtained by a Sol-Gel Method," *Ceram. Int.,* 24 [4] 281-284 (1998).
9. V. Dureuil, C. Ricolleau, M. Gandais, C. Grigis, J. P. Lacharme, A. Naudon "Growth and Morphology of Cobalt Nanoparticles on Alumina," *J. Cryst. Growth,* 233 737–748 (2001).
10. F. Grillo, M. M. Natile, A. Glisenti "Low Temperature Oxidation of Carbon Monoxide: the Influence of Water and Oxygen on the Reactivity of a Co_3O_4 Powder Surface," *Appl. Catal. B-Environ.,* 48 267–274 (2004).
11. T. Junru, H. Yunfang, H. Wenxiang, C. Xiuzeng, F. Xiansong "The Preparation and Characteristics of Cobalt Blue Mica Coated Titania Pearlescent Pigment," *Dyes and Pigments,* 52 [3] 215-222 (2002).
12. S. Karagoz, T. Karayildirim, S. Ucar, M. Yukselc, J. Yanikb "Liquefaction of Municipal Waste Plastics in VGO Over Acidic and Non-acidic Catalysts," *Fuel,* 82 415-423 (2003).
13. L. F. Koroleva "Synthesis of Spinel-based Ceramic Pigments From Hydroxycarbonates," *Glass Ceram+,* 61 [9-10] 299-302 (2004).
14. J. Llorca, P. D. Ramıirez de la Piscina, Jean-Alain, N. Homs "Transformation of Co_3O_4 During Ethanol Steam-re-forming. Activation Process for Hydrogen Production," *Chem. Mater.,* 16 3573-3578 (2004).
15. M. Llusar, A. Fores, J. A. Badenes, J. Calbo, M. A. Tena, G. Monros "Colour Analysis of Some Cobalt-Based Blue Pigments," *J. Eur. Ceram. Soc.,* 21 [8] 1121-1130 (2001).
16. J. Merikhi, H.-O. Jungk, C. Feldmann "Sub-Micrometer $CoAl_2O_4$ Pigment

Particles - Synthsis and Preparation of Coatings," *J. Mater. Chem.,* 10 1211-1314 (2000).
17. F. Meyer, A. Dierstein, C. Beck, W. Hartl, R. Hempelmann, S. Mathur, M. Veith "Size-Controlled Synthesis of Nanoscaled Aluminium Spinels Using Heterobimetallic Alkoxide Precursors via Water/Oil Microemulsions," *Nanostruct. Mater.,* 12 71-74 (1999).
18. M. P. Morales, S. A. Walton, L. S. Prichard, C. J. Serna, D. P. E. Dickson, K. O'Grady "Characterisation of Advanced Metal Particle Recording Media Pigments," *J. Magn. Magn. Mater.,* 190 357-370 (1998).
19. P. Nkeng, J.-F. Koenig, J. L. Gautier, P. Chartier, G. Poillerat "Enhancement of Surface Areas of Co_3O_4 and $NiCo_2O_4$ Electrocatalysts Prepared by Spray Pyrolysis," *J. Electroanal. Chem.,* 402 81-89 (1996).
20. N. Ouahdi, S. Guillemet, J. J. Demai, B. Durand, L. Er Rakho, R. Moussa, A. Samdi "Investigation of the Reactivity of $AlCl_3$ and $CoCl_2$ Toward Molten Alkali-metal Nitrates in Order to Synthesize $CoAl_2O_4$," *Mater. Lett.,* 59 [2-3] 334-340 (2005).
21. M. Richter, M. Langpape, S. Kolf, G. Grubert, R. Eckelt, J. Radnik, M. Schneider, M. M. Pohl, R. Fricke "Combinatorial Preparation and High-Throughput Catalytic Tests of Multi-Component deNOx Catalysts," *Appl. Catal. B-Environ.,* 36 [4] 261-277 (2002).
22. C. Roldan, J. Coll, J. L. Ferrero, D. Juanes "Identification of Overglaze and Underglaze Cobalt Decoration of Ceramics From Valencia (Spain) by Portable EDXRF Spectrometry," *X-Ray Spectrom.,* 33 [1] 28-32 (2004).
23. T. Mori "Phase Diagram of the System Cobalt(II) Oxide-Aluminum Oxide," *Yogyo Kyokaishi,* 90 [2] 100-101 (1982).
24. P. Thormahlen, E. Fridell, N. Cruise, M. Skoglundh, A. Palmqvist "The Influence of CO, C_3H_6, NO, H_2, H_2O or SO_2 on the Low-temperature Oxidation of Co on a Cobalt-Aluminate Spinel Catalyst ($Co_{1.66}Al_{1.34}O_4$)," *Appl. Catal. B-Environ.,* 31 [1] 1-12 (2001).
25. S. Ucar, S. Karagoz, T. Karayildirim, J. Yanik "Conversion of Polymers to Fuels in a Refinery Stream," *Polym. Degrad. Stab.,* 75 161-171 (2002).
26. W. J. Stark, L. Madler, M. Maciejewski, S. E. Pratsinis, A. Baiker "Flame Synthesis of Nanocrystalline Ceria-Zirconia: Effect of Carrier Liquid," *Chem. Commun.,* [5] 588-589 (2003).
27. L. S. Wang, Y. H. Zhou, Z. W. Quan, J. Lin "Formation Mechanisms and Morphology Dependent Luminescence Properties of Y_2O_3:Eu Phosphors Prepared by Spray Pyrolysis Process," *Mater. Lett.,* 59 [10] 1130-1133 (2005).
28. J. C. Rodriguez, C. Guimon, A. J. Marchi, A. Borgna, A. Monzon "Activity, Selectivity and Coking of Bimetallic Ni-Co-Spinel Catalysts in Selective Hydrogenation Reactions," *Stud. Surf. Sci. Catal.,* 111 183-190 (1997).
29. A. Hadi, I. Yaacob, I. "Synthesis of PdO/CeO_2 Mixed Oxides Catalyst for Automotive Exhaust Emissions Control," *Catal. Today,* 96 [3] 165-170 (2004).
30. T. Kanazawa "Development of Hydrocarbon Adsorbents, Oxygen Storage Materials for Three-way Catalysts and NOx Storage-Reduction Catalyst," *Catal. Today,* 96 [3] 171-177 (2004).
31. S. Matsumoto "Recent Advances in Automobile Exhaust Catalysts," *Catal.*

Today, 90 [3-4] 183-190 (2004).
32. J. Li, J. Hao, L. Fu, T. Zhu, Z. Liu, X. Cui "Cooperation of Pt/Al_2O_3 and In/Al_2O_3 Catalysts for NO Reduction by Propene in Lean Burn Condition," *Appl. Catal., A,* 265 [1] 43-52 (2004).
33. A. Camenzind, R. Strobel, S. E. Pratsinis "Cubic or Monoclinic $Y_2O_3:Eu^{3+}$ Nanoparticles by One Step Flame Spray Pyrolysis," *Chem. Phys. Lett.,* 416 [4-6] 193-197 (2005).
34. R. Mueller, R. Jossen, S. E. Pratsinis, M. Watson, M. K. Akhtar "Zirconia Nanoparticles Made in Spray Flames at High Production Rates," *J. Am. Ceram. Soc.,* 87 [2] 197-202 (2004).
35. R. Mueller, R. Jossen, H. K. Kammler, S. E. Pratsinis "Growth of Zirconia Particles Made by Flame Spray Pyrolysis," *AIChE J.,* 50 [12] 3085-3094 (2004).
36. K. F. Waldner, R. M. Laine, S. Dhumrongvaraporn, S. Tayaniphan, R. Narayanan "Synthesis of a Double Alkoxide Precursor to Spinel ($MgAl_2O_4$) Directly From $Al(OH)_3$, MgO, and Triethanolamine and Its Pyrolytic Transformation to Spinel," *Chem. Mater.,* 8 [12] 2850-2857 (1996).
37. J. M. McHale, A. Navrotsky, A. J. Perrotta "Effects of Increased Surface Area and Chemisorbed H_2O on the Relative Stability of Nanocrystalline γ-Al_2O_3 and α-Al_2O_3," *J. Phys. Chem. B,* 101 [4] 603-613. (1997).
38. D. H. Lee, S. Condrate, R. A. "An FTIR Spectral Investigation of the Structural Species Found on Alumina Surfaces," *Mater. Lett.,* 23 [4-6] 241-246 (1995).
39. J. M. Saniger "Al-O Infrared Vibrational Frequencies of γ-alumina," *Mater. Lett.,* 22 [1-2] 109-113 (1995).
40. P. Tarte "Infra-Red Spectra of Inorganic Aluminates and Characteristic Vibrational Frequencies of AlO_4 Tetrahedra and AlO_6 Octahedra," *Spectrochim. Acta A-M,* 23 [7] 2127-2143 (1967).

Chapter 5.

Systematic Synthesis of Mixed Metal Oxides in NiO-Co_3O_4, NiO-MoO_3, and NiO-CuO Systems via Liquid Feed-Flame Spray Pyrolysis

5.1. Introduction

Liquid feed flame spray pyrolysis, LF-FSP, has proven to be a versatile tool for the production of both well-known single and mixed-metal oxide nanopowders and as shown previously, sets of single and mixed phase powders for which there are no known examples in the current literature.[1-5]

The preceding chapters have focused on working with systems where the mixed-metal oxide components were miscible. This chapter explores the use of LF-FSP to study the production of nanopowders wherein the phases were immiscible. The previous oxide systems studied fall into three categories: production of nanopowders for (1) photonic applications, (2) structural applications, and (3) for catalyst applications. Efforts in the latter area focused on developing high specific surface area, easily dispersed alumina/transition metal oxide systems including NiO, CoO_x and CuO binary oxides. It is important to note that a number of other groups are also exploring the use of flame processes for the synthesis of novel nanopowders.[6-14]

It is well known that bi- and tri-metallic catalysts often offer properties much superior to single metal catalysts.[15-19] Thus, the goal of the work reported in this chapter is to develop an understanding of the gas phase behavior of three selected bimetallic transition metal systems as a prelude to exploring the potential utility of LF-FSP for producing

bimetallic catalysts while coincidentally introducing alumina as a possible support. Another goal of the work reported here is to demonstrate the utility of LF-FSP as a means of systematically producing sets of mixed-metal oxide nanopowders in selected phase space.

This chapter reports on the systematic synthesis of three nanopowder series along the $NiO\text{-}Co_3O_4$, $NiO\text{-}MoO_3$, and NiO-CuO tie lines. Sixteen individual samples were produced via liquid-feed flame spray pyrolysis (LF-FSP) and analyzed by SSA, SEM, EDX, FTIR, TGA-DTA, and XRD.

The powders typically consist of single crystal particles <35 nm diameter and specific surface areas (SSAs) of 20–50 m^2/g. X-ray powder diffraction studies (XRDs) show a gradual change in their patterns from pure NiO to pure MO_x (M = Co, Mo, Cu). Most compositions yielded single-phase materials but mixed phase materials where also detected.

The partial pressure of O_2 in LF-FSP affects the formation of particular oxide phases and controls to a certain degree the morphologies of the as-produced materials. In the $NiO\text{-}MoO_3$ system preferential growth of certain crystallographic planes in MoO_3, due to the relatively high vapor pressure of MoO_3 is observed. Unusual particle morphologies seen in the $NiO\text{-}Co_3O_4$ system are attributed to some phase separation in the as-produced materials. TGA studies combined with diffuse reflectance FTIR spectroscopic (DRIFTS) studies indicate that both physi- and chemi-sorbed H_2O are the principal surface species present in the as-processed nanopowders.

5.2. Experimental

5.2.1. Materials

Nickel nitrate hexahydrate [$Ni(NO_3)_2 \cdot 6H_2O$, 99.9%], copper nitrate hydrate [$Cu(NO_3)_2 \cdot 2.5H_2O$, 99.9%], cobalt nitrate hexahydrate [$Co(NO_3)_2 \cdot 6H_2O$, 99.97%], propionic acid [$CH_3CH_2CO_2H$, 99%], and anhydrous ethanol [CH_3CH_2OH, 99%] were purchased from Sigma-Aldrich and used as received.

Ammonium molybdate [$(NH_4)_6Mo_7O_{24} \cdot 4H_2O$, 98%] was purchased from MCB Reagents and used as received. An aqueous solution (85%) of DL-lactic acid [$C_3H_6O_3$, 99^+%] was purchased from Alfa-Aesar and also used as received.

5.2.2. Precursor Synthesis

All of the metal nitrates were reacted to produce high quality precursors using similar reaction routes. First the nitrate powders (see below for precise amounts) were placed in a 500 mL flask equipped with a still head, addition funnel, and a N_2 sparge to help agitate the solution, then de-ionized water (50.0 mL 2.78 mol) was added to dissolve the powders, after which propionic acid (400.0 mL, 5.36 mol) was rapidly added. The resulting solution was heated to ~150 °C for 6 h to distill off ~160 mL of liquid (water/propionic acid), coincidentally concurrently removing byproduct NO_x gas. The amount of nitrate powder used per batch was 200.0 g, which are 0.688, 0.860 and 0.687 moles respectively, for nickel, cobalt and copper nitrate hydrates. The resulting solutions were reduced in volume using a rotary evaporator until the total volume was less than ~180 mL. The solutions form viscous green (Ni^{2+}), deep purple (Co^{3+}) and blue (Cu^{2+}) liquids, respectively. The ceramic loading of these viscous liquids was determined by thermo gravimetric analysis (TGA), wherein a 10

mg sample was heated in air to 1000 °C at 10 °C/min, with the final mass being recorded. The loadings for these solutions were typically 10–14 wt. %.

The molybdenum precursor was synthesized by dissolving 50.0 g (0.040 mol) of ammonium molybdate in ~800 mL of boiling DI water containing 150 mL of lactic acid. The solubility of the solution was greatly enhanced by adding lactic acid at solution temperatures above 100 °C. Once all of the solid dissolved, the solution was stirred mechanically for 2 h until a light blue hue was detected. The solution was then distilled to remove excess H_2O and acid. A rotary evaporator was used to further remove solvent and reduce the volume to less than 300 mL, yielding ~210 g of dark brown viscous precursor. The ceramic loading determined by TGA was 23.7 wt. %.

5.2.3. Precursor Formulations

Sixteen different precursor formulations were used to produce nanopowders with specific stoichiometries to explore the NiO-Co_3O_4, NiO-MoO_3 and NiO-CuO oxide systems. Forty g samples of all nanopowders at ~80 g/h rates were produced. Precise amounts of the specific precursor solutions were diluted with EtOH and mixed by mechanical stirring prior to use for LF-FSP processing. Solutions used to produce the nanopowders typically contained 3 wt. % ceramic in precursor form by TGA. Dilute solutions not only minimize rheological complications with the LF-FSP process but also give access to smaller, more uniform particles. The compositions for the NiO-Co_3O_4, NiO-MoO_3 and NiO-CuO are shown in Table 5-1, Table 5-2 and Table 5-3, respectively. All sixteen different composition were produced systematically over a 15 d period. The LF-FSP apparatus required minimal maintenance and cleaning during the synthesis of any one particular oxide system.

Table 5-1. Precursor compositions for the NiO-Co_3O_4 system

Sample	Mol % Ni	Mol % Co
1	0	100
2	5	95
3	15	85
4	30	70
5	50	50
6	70	30
7	90	10
8	100	0

Table 5-2. Precursor compositions for the NiO-MoO_3 system

Sample	Mol % Ni	Mol % Mo
1	0	100
2	25	75
3	50	50
4	75	25
5	100	0

Table 5-3. Precursor compositions for the NiO-CuO system

Sample	Mol % Ni	Mol % Cu
1	0	100
2	25	75
3	50	50
4	75	25
5	100	0

Three different compositions per day could be synthesized because of the ease of collecting the nanopowders and the relatively large production rates. The apparatus was thoroughly cleaned in between each nanopowder oxide system production to prevent any cross-contamination.

5.3. Results and Discussion

The $NiO-Al_2O_3$ system described previously is of particular interest because of the continuing interest in the use of $NiO-Al_2O_3$ materials for multiple catalyst applications as well as for fuel cell electrodes.[20-22] Furthermore, NiMo, NiCo, and NiCu systems are already well-known for their utility as hydrotreating catalysts, [23-27] and other catalytic reactions.[28-30] All three systems discussed here have NiO as the end member and also permit comparison with previous work on the $NiO-Al_2O_3$ system, which serves for baseline comparisons with the current work.

Altogether, 16 samples (see Tables 5-1 through 5-3) with specific stoichiometries were produced separately from inexpensive, easily synthesized metal carboxylate precursors (see experimental) using methods reported above.[2-5] Thereafter, all of the nanopowders produced were characterized using a variety of techniques, including SSA, SEM, FTIR, TGA-DTA, and XRD. The results presented start with a discussion on particle morphologies in terms of specific surface areas, morphologies, size and size distributions, and the presence of surface species, for each of the systems studied. The thermal behavior of each of the nanopowders, is then discussed, followed by a study of the phases present and their gradual transitions with changing stoichiometries for each of the systems.

5.3.1. Powder Characterization.

5.3.1.1. Surface areas analyses

Specific surface area analyses of all as-produced samples are shown in Table 5-4. Microporosity was neither expected nor detected in any sample. The surface area values for all samples are between 18 and 48 m^2/g. These values

are quite low compared to those seen in the NiO-Al_2O_3 binary system[4] which start at 78 m^2/g for pure δ-Al_2O_3 and drop slowly to 45 m^2/g for the sample that is 78 mol % NiO and then precipitously to 7 m^2/g for pure NiO. It is important to note that the improvements to our system have led to better synthesis conditions now giving pure NiO SSAs of 32 m^2/g.

Table 5-4. Specific surface areas (SSA) and average particle sizes (APS)

Sample	SSA (m^2/g) ± 0.5	APS nm (BET)
100 Al	70	20
100 Ni	32	27
100 Co	43	23
100 Cu	18	53
100 Mo	32	40
5Ni 95Al	77	21
22Ni 78Al	60	24
43Ni 57Al	69	18
78Ni 22Al	45	23
5Ni 95Co	37	26
15Ni 85Co	36	27
30Ni 70Co	35	27
50Ni 50Co	30	30
70Ni 30Co	26	33
90Ni 10Co	26	34
25Ni 75Mo	35	34
50Ni 50Mo	30	35
75Ni 25Mo	38	25
25Ni 75Cu	36	25
50Ni 50Cu	36	25
75Ni 25Cu	48	19

In order to explain the lower surface areas observed in these studies a potential mechanism for particle formation that involves condensation from the gas phase wherein the materials with the lowest vapor pressures (highest boiling

points) condense most rapidly, forming critical nuclei that grow as long as the gas phase temperatures remain above the condensation temperatures of the oxides. The melt temperatures for Al_2O_3, NiO, CoO and CuO and are listed in Table 5-5.

Table 5-5. Metal oxide melting temperatures

Metal oxide	T_m (°C)	Density g/cc	Comments (ref)
Al_2O_3	2050	3.6	δ-phase
NiO	1935	7.45	(31)
CoO	1830	6.45	(31)
CuO	1450	6.31	(31)
Co_3O_4	900	6.07	Decomposes (31)
MoO_3	801	4.69	Sublimes 1155°C (31)

As can be seen, the melting temperatures (T_m) for the transition metal oxides in this study are all lower than that of Al_2O_3: ~2050 °C.[32] It is also important to note that T_m of the oxides are often determined in pure O_2 rather than an air atmosphere to prevent reductive decomposition, as seen for Co_3O_4 and CoO.[33-35] One can assume that the T_m values for these materials relate directly to their vapor pressures in the flame, then Al_2O_3 is most likely to condense and solidify long before the other metal oxides do.

Nucleation of Al_2O_3 in the gas phase can therefore be expected to proceed, but growth and/or coalescence to form larger particles will be limited by the anticipated low vapor pressures for residual Al_2O_3 vapor. It can be proposed that in the same time frame, NiO, CoO, and CuO will remain in the vapor phase for a longer period of time. Consequently, particle growth and/or coalescence can be expected to occur for relatively longer periods of time, leading to larger particles and correspondingly lower SSAs. For mixed metal systems, particle

nucleation can lead to single phase mixed-metal oxides if the reaction occurs in the gas phase prior to nucleation. For immiscible materials, sequential nucleation leading to core-shell or mixtures of two types of nanopowder products based solely on vapor pressures might be anticipated.

It is important to note here that the melting points of nanoparticles can be 100s of °C less than those of the bulk materials because of the substantially higher surface energies that facilitate solidification and/or crystallization.[36-37]

On the basis of the above arguments, one expects to find that the particle sizes and corresponding SSAs can be directly related to the T_m values such that NiO and CoO should behave much as Al_2O_3 and MoO_3 forming the largest particles. However, this does not seem to be the case, as the particle sizes seem to follow no discernable pattern. The kinetics for nucleation and particle growth processes under LF-FSP conditions are not known at present, but assuming the processing conditions used in these studies are uniform throughout, it seems reasonable to assert that there are significant differences arising from the particular ions present and O_2 partial pressures. A further complication results because in some instances two or more phases form under the synthesis conditions. These phases can result from the same elements, e.g. CoO and Co_3O_4 or from different elements resulting in segregated phases as observed for MoO_3 and NiO (see below). In the latter case, product formation is greatly affected by the fact that MoO_3 sublimes very easily and will stay in the gas phase the longest of all the oxides produced.

Still other complications that affect the data reported in Table 5-4 originate from BET derived APSs, which are average values that do not account for the formation of two separate phases. Furthermore, BET data will emphasize very fine particles over large particles and thus the SSAs will be heavily weighted towards the finer sized particles. An additional issue is that, as seen in the SEM micrograph studies that follow, some particle systems are necked, and as such, although SSA values suggest certain particle sizes, the true aggregate sizes can be much larger.

5.3.2. Scanning electron microscopy

Scanning electron micrographs (SEMs) were taken to assess the particle size distributions and morphologies of all the materials produced. Most of the nanopowders observed exhibit spherical morphologies. A very few large (0.5–1.2 μm) spherical particles in some samples (e.g. 15 mol % Co; 25 mol %Cu) can be attributed to residual impurities from the precursors. These micrographs suggest relatively narrow particle size distributions and small APSs. The SEMs show some electrostatically agglomerated, and very small soft aggregated particles. Support for this statement comes from the fact that these particles disperse easily in liquid media. The SEMs also suggest the presence of a some partially sintered aggregates based on what appears to be extensive necking, particularly in the high Ni loaded samples. Some of the necking is also attributed as being an artifact of the Au-Pd overcoat used to enhance contrast and prevent charging when the images are recorded.

Figure 5-1 through Figure 5-4 provide representative micrographs for particles in the NiO-Co_3O_4 system. One likely explanation for the formation of these aggregates may be that some Co_3O_4 decomposes (T_d = 900 °C) in the time frame that the gases are of sufficient temperature and this process leads to particle coalescence. Samples ≥50 mol % NiO exhibit a reasonable fraction of particles with cubic morphologies, as a result of the formation of NiO-CoO solid solutions, see XRD analyses as discussed below.

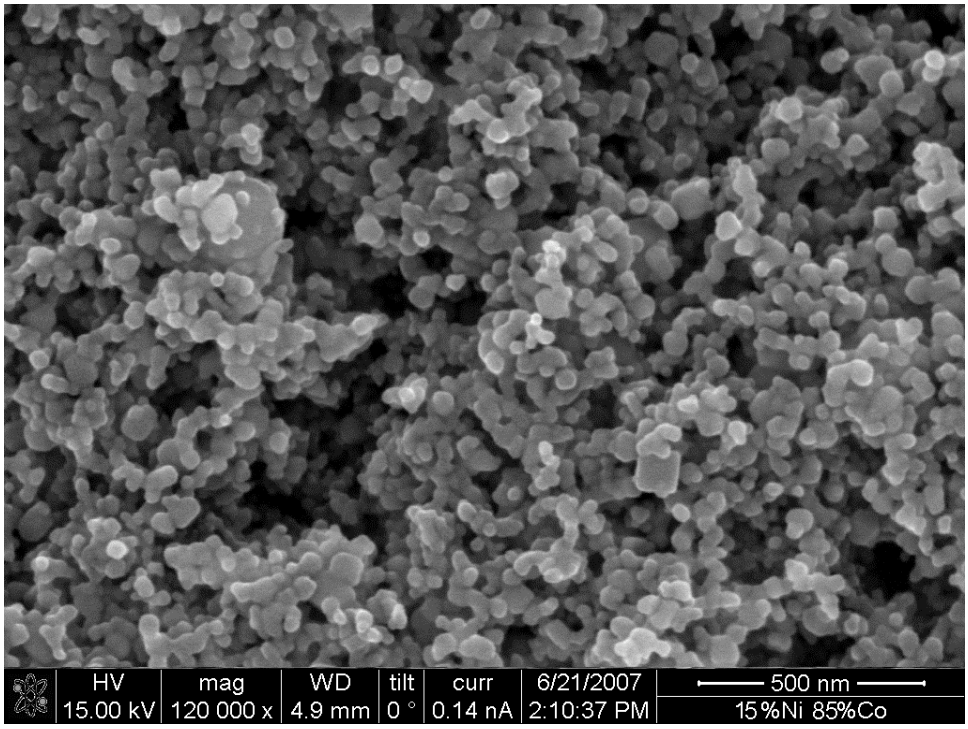

Figure 5-1. SEM micrograph for 15 mol % NiO 85 mol % Co_3O_4

Figure 5-5 and Figure 5-6 show representative examples of faceted MoO_3 particles that are "dusted" by much smaller, spherical NiO particles. It is well known that certain crystallographic planes in MoO_3 crystal structure exhibit preferential growth along the <100> directions.[38] This preferential growth is due

to the low vapor pressure of MoO_3 and high mobility of the Mo^{+3} ion along the diagonal directions of the MoO_3 tetrahedron.

The preferential growth of these planes in MoO_3 is the cause of their unusual morphology. The relative composition of these particles where ascertained using energy dispersive X-ray spectroscopy (EDX).

The large particles are unequivocally MoO_3 particles and the smaller spherical ones, NiO particles. Similar to other work NiMo hydrotreating catalysts often consist of Ni particles at the edges of larger molybdenum oxide crystallites.[30]

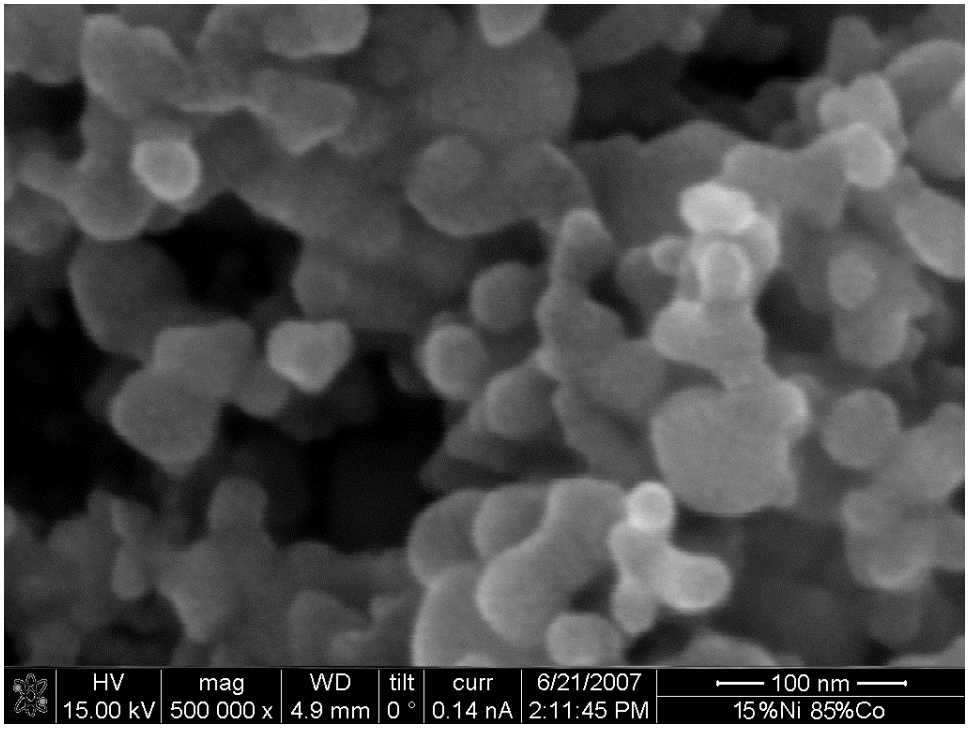

Figure 5-2. Hi-mag SEM micrograph of 15 mol % NiO 85 mol % Co_3O_4

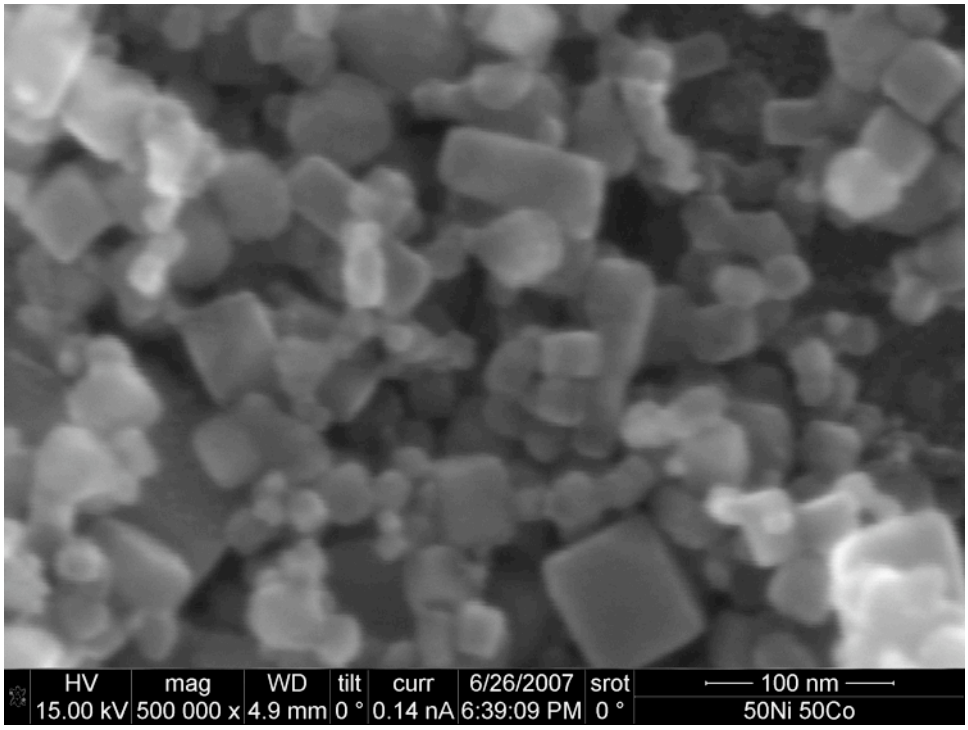

Figure 5-3. Hi-mag SEM micrograph of 50 mol % NiO 50 mol % Co_3O_4

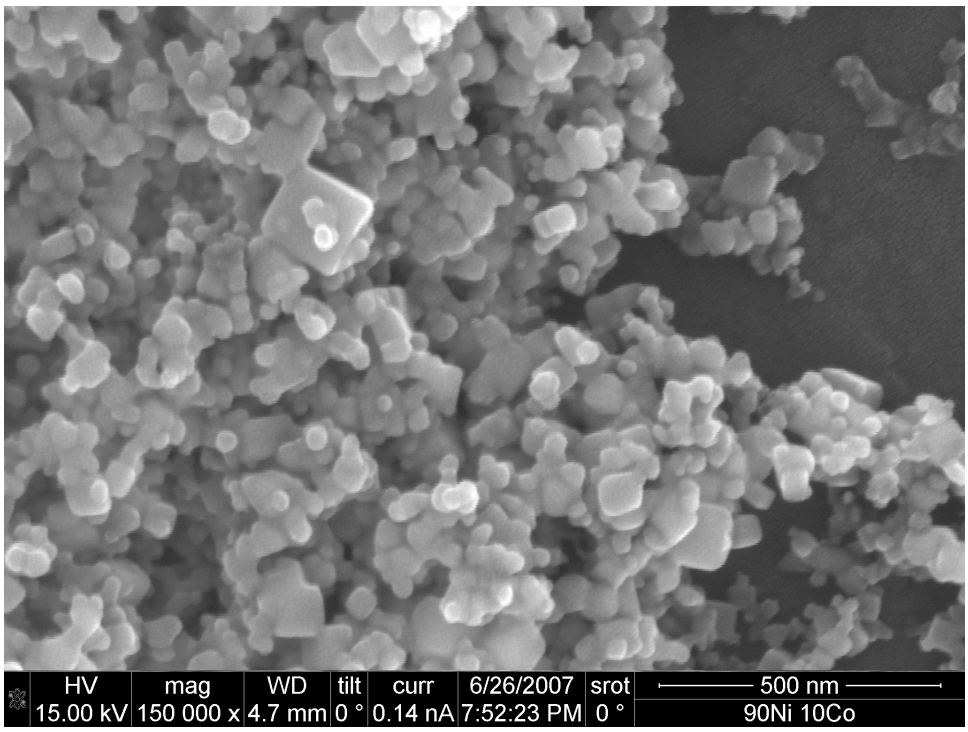

Figure 5-4. SEM micrograph of 90 mol % NiO 10 mol % Co_3O_4

Figure 5-7 is an SEM micrograph of 25 mol NiO 75 mol % CuO sample and is representative of all other compositions in the system. The particles in the NiO-CuO system are visibly indistinguishable from each other.

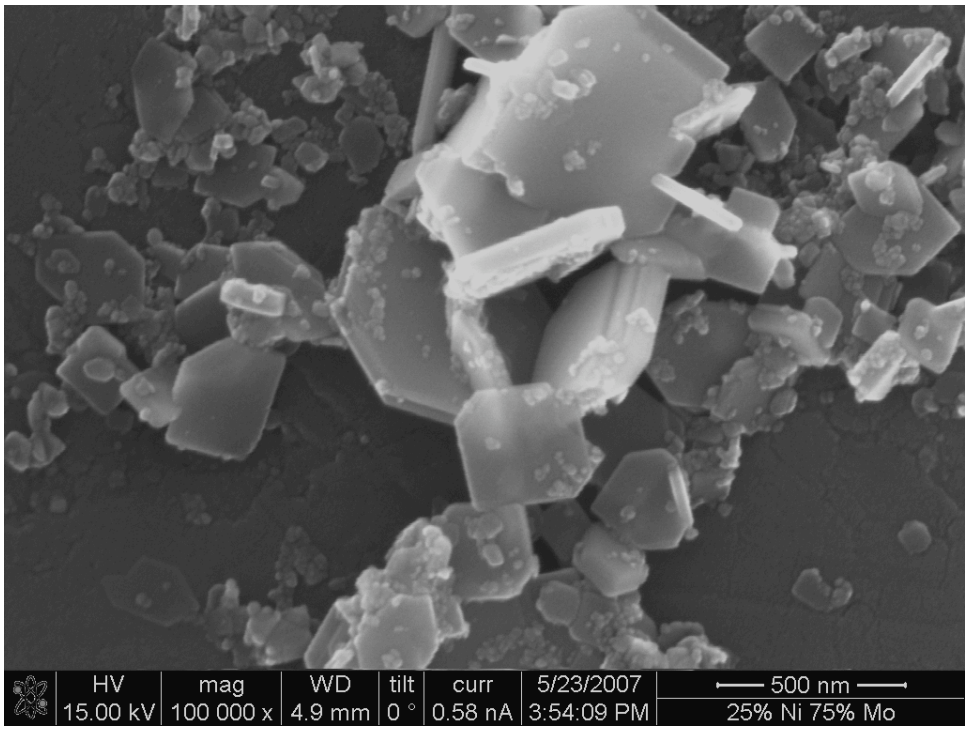

Figure 5-5. SEM micrographs of 25 mol % NiO 75 mol % MoO_3

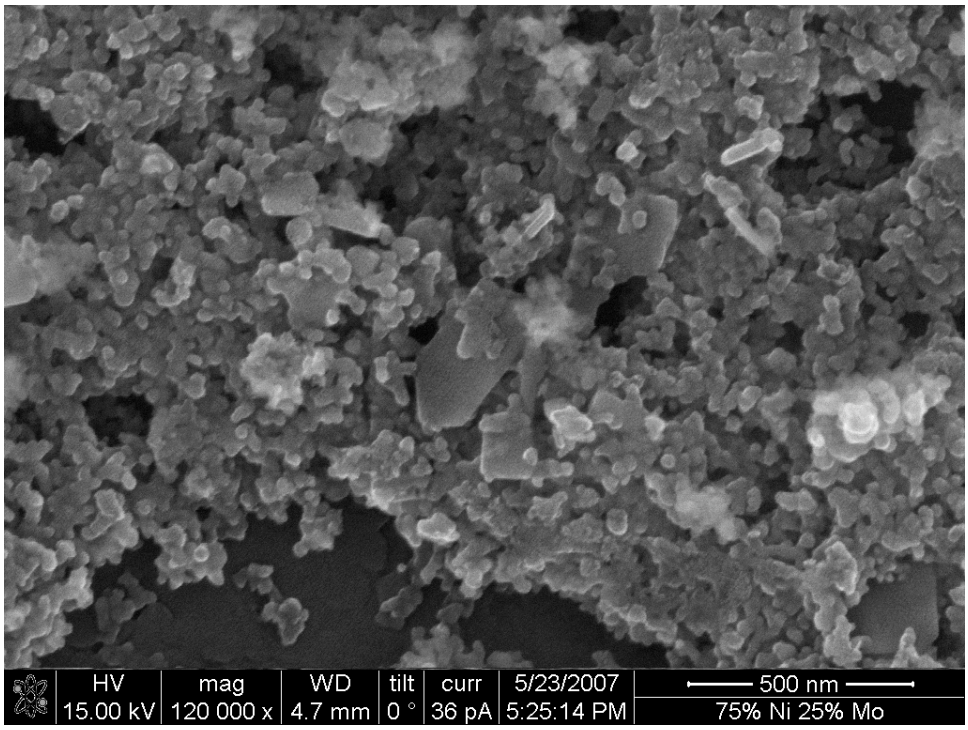

Figure 5-6. SEM micrographs of 75 mol % NiO 25 mol % MoO_3

The particle size distributions of these materials are the narrowest of the three systems studied, all of the samples exhibit an extremely homogeneous particle population. These narrow particle distributions arise most likely from intimate mixing in the low mol. % CuO materials, forming a solid solution and possible layering (core-shell formation) in the higher mol % CuO materials. The layering is likely due to CuO remaining in the vapor phase longer and depositing onto NiO particles that form earlier in the process. A detailed discussion of the particle formation behavior seen for the NiO-CuO system is left for future experiments and other researchers.

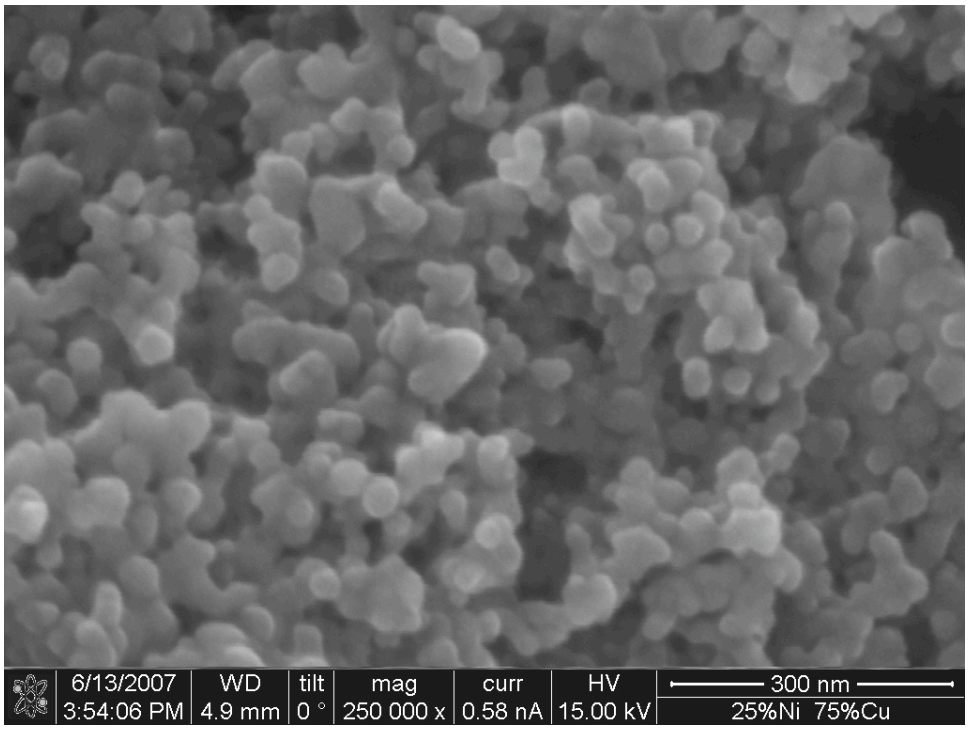

Figure 5-7. SEM micrograph of 25 mol % NiO 75 mol % CuO representative of all samples in this oxide system

The images above show mostly agglomerated or slightly aggregated homogeneous particles with very few outliers. The pure NiO nanopowder micrograph shows a small fraction of aggregated particles and possibly some necked particles. Neck formation may cause some particles to appear faceted, but the primary spherical morphology is still clearly visible.

5.3.2.1. Thermal gravimetric analyses

TGAs were performed on all as-prepared samples to determine their thermal behavior and relative amounts of adsorbed surface species (H_2O and CO_3^{2-}). Most samples exhibit initial 1-3 % mass losses, typical for nanopowders produced via LF-FSP. This loss is expected and associated with desorption of physi- and chemi-sorbed water resulting from the combustion process and

atmosphere due to their relatively high surface areas, as seen prevopusly.[1-6] A specific discussion on the thermal behavior after these typical losses of each system follows.

Figure 5-8 presents TGA traces for the NiO-Co_3O_4 system. Four of the samples show substantial mass gains of 1–3 wt. % in the 200 to 700 °C. Samples with 95% CoO_x to 50 % CoO_x exhibit mass gains starting ≈ 200 °C, resulting from oxidation of CoO to Co_3O_4. This mass increase is attributed wholly to oxidation per the following chemical reaction:

$$6CoO + O_2 \rightarrow 2Co_3O_4 \qquad (1)$$

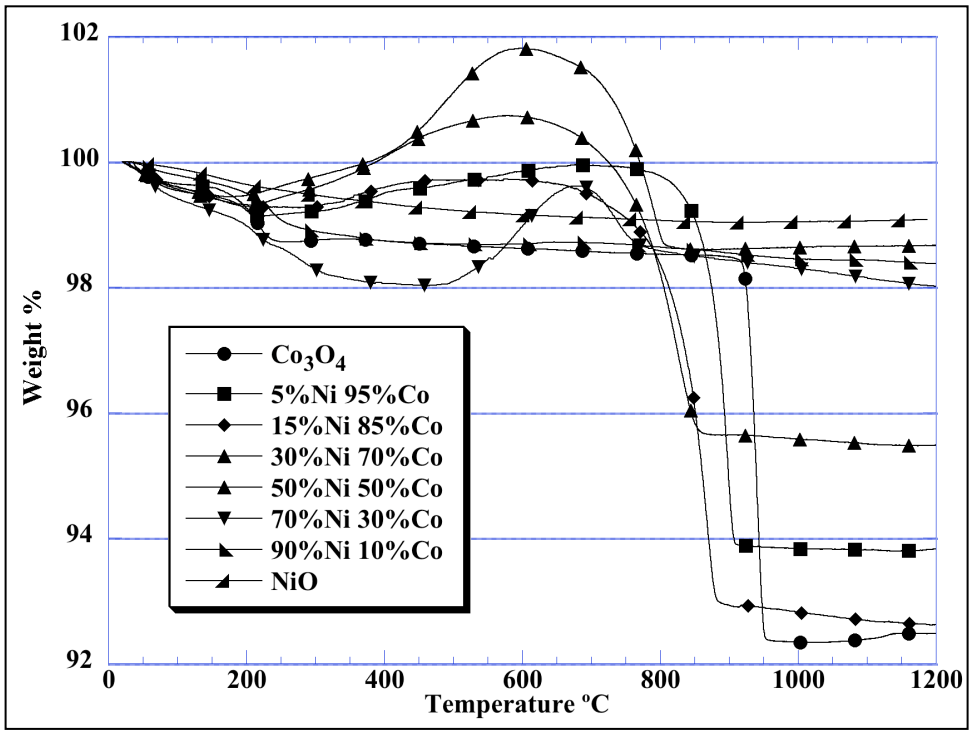

Figure 5-8. TGA traces for the NiO-Co_3O_4 system

The initial weight percent NiO and CoO_x in these materials was calculated from the observed mass increase. The values are presented in Table 5-6, along

with the values obtained from XRD phase simulations, for the high CoO_x contents samples agree very well. The values for the two higher NiO samples deviate substantially from one another because the simulation algorithm is only an intensity matching one (see XRD results for further discussion).

The formation of CoO in these samples in the synthesis process is due mainly to slight variations of O_2 partial pressure in the reaction chamber. It is well known that very slight variations in O_2 partial pressure will affect the stoichiometry of CoO.[39] Another factor that may contribute to the formation of CoO is the presence of NiO. The Ni^{2+} ions stabilize Co^{2+} ions through formation of a cubic NiO-CoO solid solution.[40]

Table 5-6. Comparison of calculated and theoretical NiO wt. % in five samples of the NiO-Co_3O_4 system

	Wt. % NiO ±2	
	XRD	TGA
5Ni95Co	10%	9%
15Ni85Co	19%	16%
30Ni70Co	49%	31%
50Ni50Co	62%	56%
70Ni30Co	94%	66%

With the exceptions of pure NiO and 90 mol % NiO, all of the samples exhibit a sharp mass loss attributed to the reverse of reaction (2) around 800 °C. The theoretical mass loss for such a reduction is 6.64 %, the observed loses are 6.06, 6.01, 5.23 and 3.12 % respectively for 5, 15, 30 and 50 % NiO. These values are within experimental error for the calculated ones after the respective wt. % NiO of each samples is taken into account. The slight mass gain observed

above 1100 °C in the pure Co_3O_4 sample is attributed to defect rearrangement to achieve correct stoichiometry.

The TGA traces for the NiO-MoO_3 system are presented in Figure 5-9. This set of nanopowders presents two very distinct behaviors, depending on composition. Samples with up to 25 mol % MoO_3 exhibit only ~2 % mass losses attributed to moisture and other surface species (absorbed CO_2) but otherwise are very stable to 1200 °C. The 50 mol % MoO_3 sample gradually loses 12 % of its mass up to 500 °C, then remains stable, losing only 1 % up to 1200 °C. This sample forms the known high temperature compound, $NiMoO_4$ upon heating.[41] This phase is not detected by XRD in the "as-produced" nanopowders because the synthesis process frequently leads to kinetic rather than thermodynamic products due to the very fast quench rate (>1000 °C/ms). It is likely that re-passing these powders through the LF-FSP system will convert them to the high temperature phase, but such studies are left for a later time.[42]

The high percent MoO_3 samples have very sharp mass losses starting at ~790 °C, attributable to vaporization of MoO_3. The subsequent change in rate in the mass loss seen ~1000 °C is due to the formation and then decomposition of MoO_2. The residue on both of the high molybdenum content samples is a mixture of NiO and/or amorphous molybdenum oxide phase.

The TGA traces for the NiO-CuO system are presented in Figure 5-10. This system presents a series of similar curves with materials stable up to 1040 °C followed by a very obvious mass loss. The only exception is the pure NiO sample which only exhibits the typical 1–2 wt. % loss from surface species. The

major mass losses are attributed to the reduction of CuO to Cu_2O from the following reaction:

$$4CuO \rightarrow 2Cu_2O + O_2 \qquad (2)$$

The theoretical mass loss for this reaction is 10.0 wt. %, the observed values are 9.8 wt. % for pure CuO, 4.8 wt. % for the 75 CuO mol %, and 2.2 wt. % for the 50 CuO mol % samples. The values for the mixed phase samples are somewhat lower than expected 8.6 and 5.2 wt. % respectively for 75 and 50 mol % CuO. This is due to the fact that these samples have nearly half of their initial copper oxide in the Cu_2O phase from the original synthesis conditions (see XRD analyses below). Taking into account the Cu_2O that is already present, the mass losses values obtain from TGA agree very well with the calculated loss amounts.

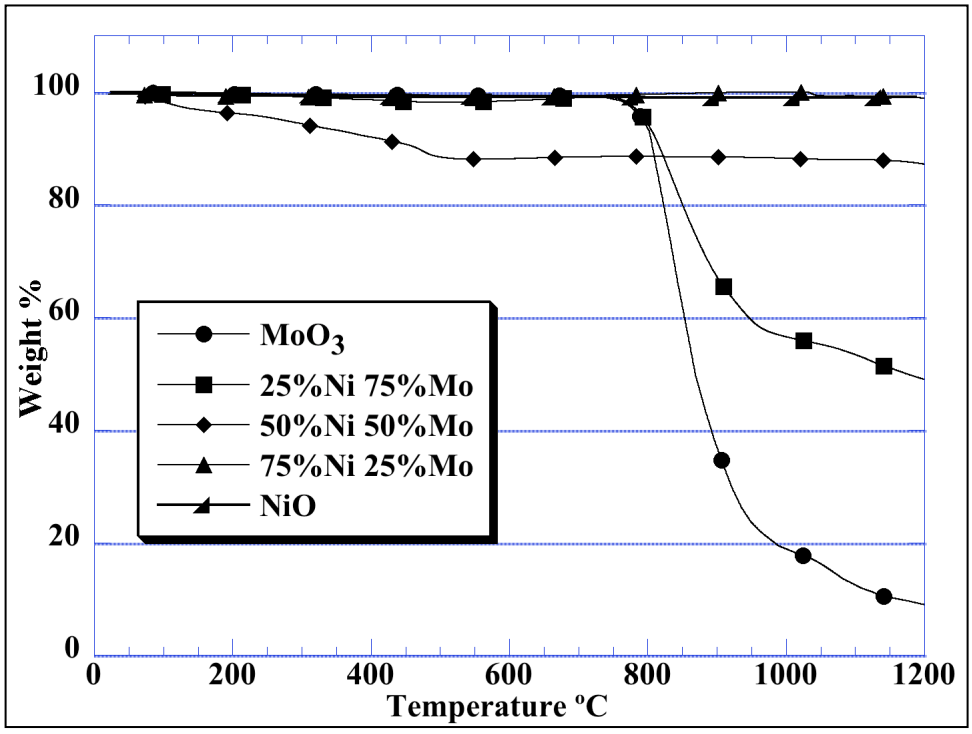

Figure 5-9. TGA traces for the NiO-MoO_3 system

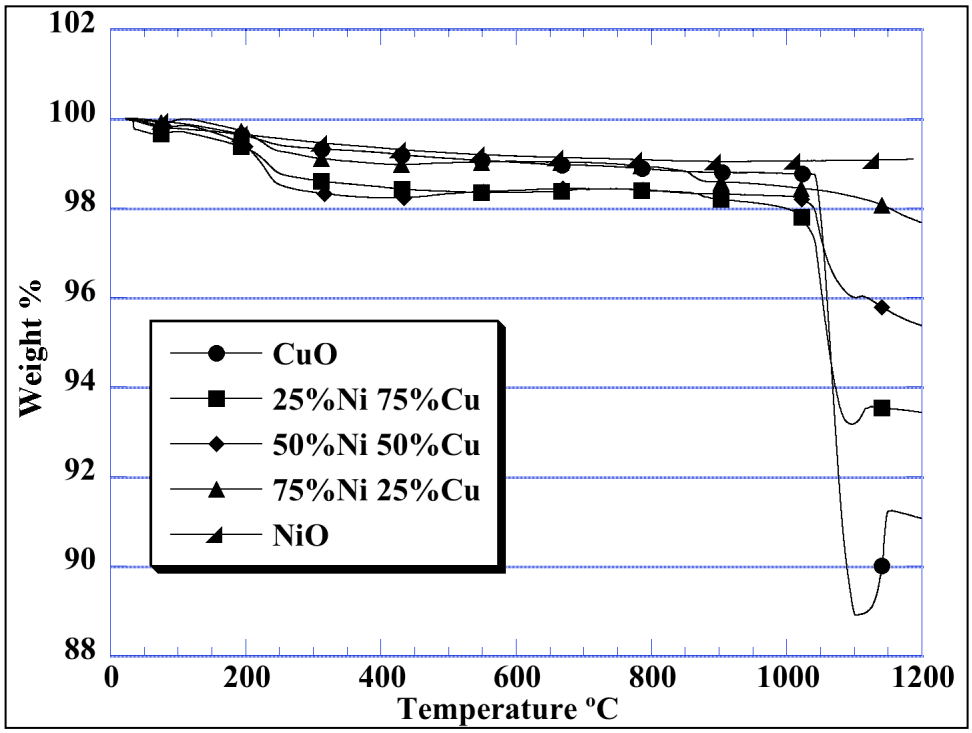

Figure 5-10. TGA traces for the NiO-CuO system

These materials then exhibit a small mass gain at ~1100 °C due to the formation of Cu_4O_3. The oxidation reaction:

$$4Cu_2O + O_2 \rightarrow 2Cu_4O_3 \qquad (3)$$

Reaction (3) has a theoretical mass gain of 5.29 wt. %, nearly twice the observed values. These materials do not gain the expected calculated mass because of the transient conditions, as the TGA thereafter reaches the decomposition temperature of Cu_4O_3 at ~1160 °C.

5.3.2.2. Fourier transform infrared spectroscopy

Diffuse reflectance infrared Fourier transform spectra (DRIFTS) for all samples are presented in Figure 5-11 through Figure 5-13. All values in the spectra above 1000 cm^{-1} are expanded and then normalized in the full spectral range; this is done so that a fair comparison can be made. In general there are

two main regions of interest, 4000–2700 cm^{-1} and 1400–400 cm^{-1}. The first region reveals a weak set of overlapping νOH bands arising from both physi- and chemi-sorbed water, typical for high surface nanopowders. In the second region, typical νM-O bands are observed.

The spectra of all the as-prepared NiO-Co_3O_4 samples are shown in Figure 5-11. In the 3700–2500 cm^{-1} region, weak νOH bands, attributable to surface hydroxyls, are observed. In the 2900–2700 cm^{-1} region, small νCH bands appear, indicating some surface organic species, particularly for the samples between 15 and 50 mol % NiO. These species could be from incomplete combustion of the precursor, but most likely result from some steam reforming in the flame. This conclusion still remains provisional, as similar results have been discussed in the other Co containing nanopowders presented previously.

The 1800–1200 cm^{-1} region exhibits bands associated with surface carbonate species. The 1000–400 cm^{-1} bands are typical for νM-O bonds. This well-defined νNi-O band appears at ca. 500 cm^{-1}.[43] Cobalt oxide (Co_3O_4) has two well-defined νCo-O bands at 690 cm^{-1} and 605 cm^{-1},[44] which emerge in the higher Co content samples. The FTIR spectra of the NiO-Co_3O_4 reveal a steady decrease and broadening in the single νNi-O band with a simultaneous increase in intensities of the two well-defined νCo-O bands.

Figure 5-12 shows the DRIFT spectra for the NiO-MoO_3 system. These samples exhibit the typical series of overlapping νOH bands suggesting surface hydroxyls arising from moisture absorbed from the environment. With the exception of MoO_3, no significant organic species are observed as evidenced by

the absence of νCH bands in the 2900–2700 cm^{-1} region. These materials have some carbonate present, as evidenced by the broad band centered approximately at 1600 cm^{-1}, particularly the samples containing molybdenum.

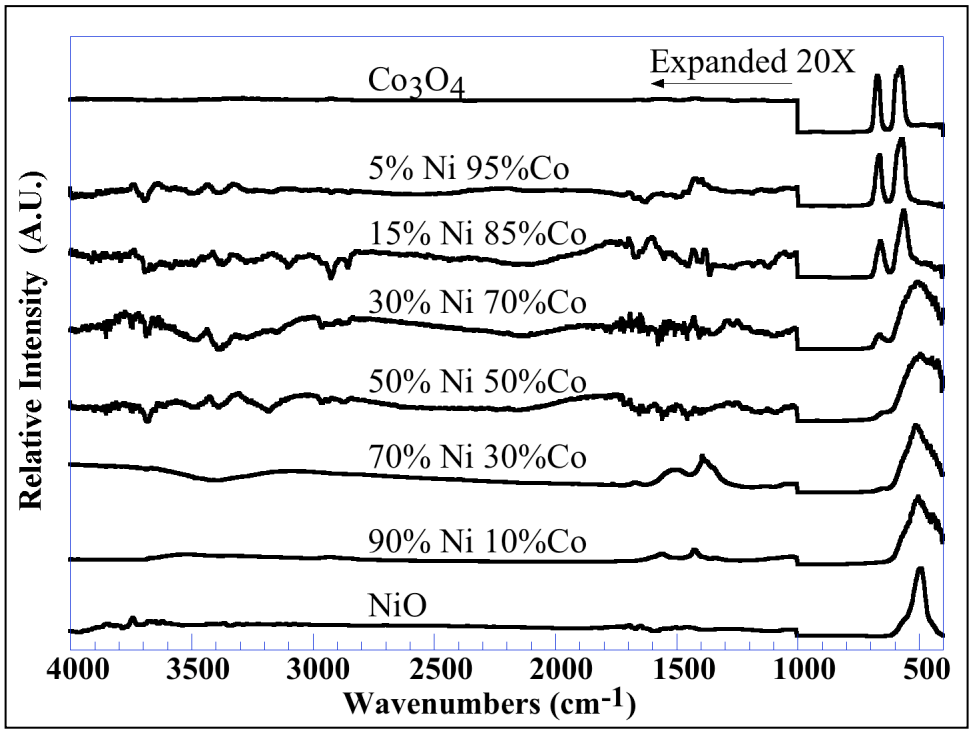

Figure 5-11. DRIFT spectra for the NiO-Co_3O_4 system

MoO_3 has three very well defined νMo-O bands, 585, 865 and 995 cm^{-1}.[45-46] These bands correspond respectively to symmetric and anti-symmetric νMo-O-Mo vibrations and surface terminated νMo-O. As with the previous system, there is a gradual intensity decrease of the well defined νNi-O and a gradual emergence of the three νMoO_3 bands.

Figure 5-13 presents spectra for the NiO-CuO system. These materials also have a series of weak overlapping νOH bands in the 3900–2500 cm^{-1} region, attributed to surface hydroxyl species. There are appreciable amounts of carbonates indicated by the band in the 1700– 1200 cm^{-1} region. These species

are most likely absorbed in the flame synthesis process from incomplete combustion. The typical νM-O bands found in the 1000 – 400 cm^{-1} region are only well defined for NiO, and only barely visible for CuO.

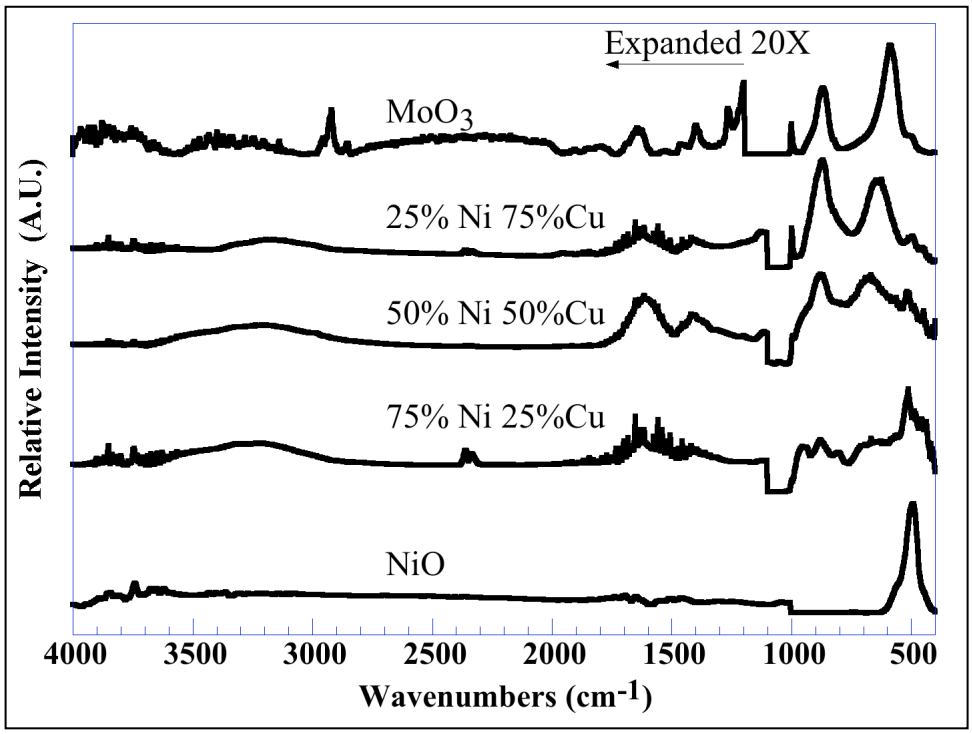

Figure 5-12. DRIFT spectra for the NiO-MoO_3 system.

Copper oxide has a very broad band with three distinct shoulders or small peaks in the 550 – 400 cm^{-1} region.[47] The pure CuO sample exhibits three peaks (487, 533, and 587 cm^{-1}), corresponding to the different stretching modes of Cu-O, and the vibration of Cu-Cu. The emergence of these peaks shows the transition from pure NiO to pure CuO.

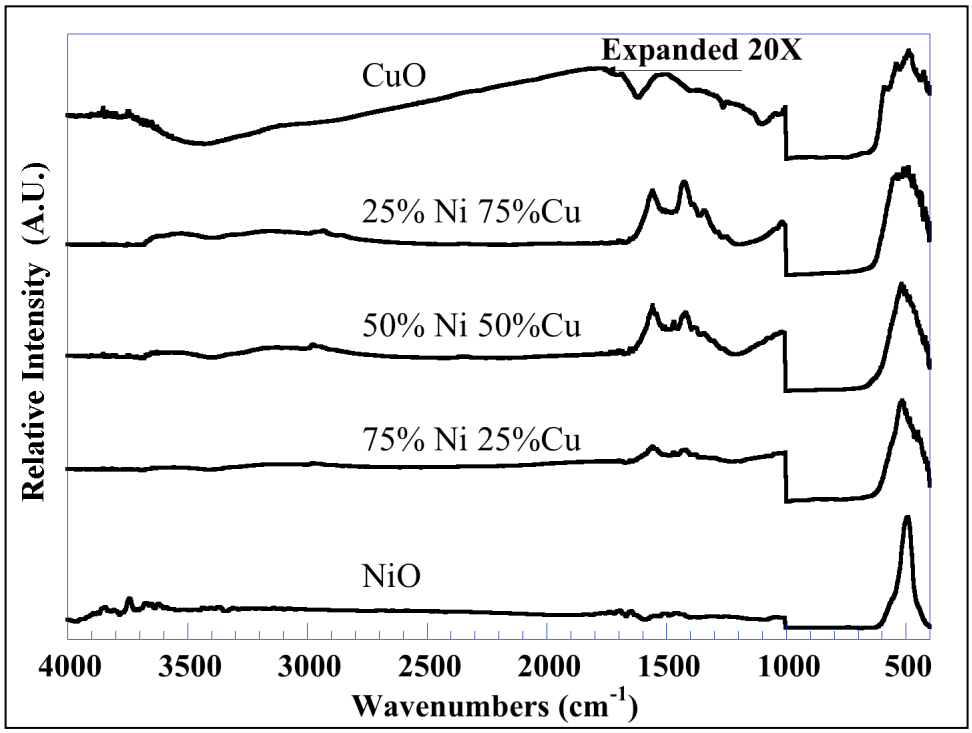

Figure 5-13. DRIFT spectra for the NiO-CuO system.

5.3.2.3. X-ray powder diffraction

XRDs patterns for all samples are shown in Figure 5-14 through Figure 5-16. The average crystallite sizes (XSs), from Debye-Scherrer XRD line-broadening analyses, and a phase analysis from simulations using Jade 7.5 are presented in Table 5-7 through Table 5-9. The three sets of spectra present some similarities such as phase pure samples for the pure oxides and a gradual transition from one pure sample to the other. All oxide systems exhibit broad peaks indicative of the small crystallite sizes. The phase compositions were calculated using a built in pattern simulation algorithm that matches the spectrum intensity at particular 2θ° values. The algorithm determines phase compositions using a least-squares fit procedure and compares these values to user determined PDF phase cards.

The XRD patterns for the NiO-Co_3O_4 system are presented in Figure 5-14. The figure clearly shows how the phase composition changes gradually from pure Co_3O_4 spinel (PDF# 00-043-1003) through a solid solution to pure cubic NiO (PDF# 01-075-0197). Samples with up to 15 mol % nickel show no crystalline NiO phases.

Table 5-7. Crystallite size and phase composition in the NiO-Co_3O_4 system from Jade 7.5 calculations

	Crystallite size (nm)			Simulation Mol % ±1.0		
	NiO	CoO	Co_3O_4	NiO	CoO	Co_3O_4
100 Co		17	36		23.7	76.3
5Ni 95Co	20	11	18	23	18	59
15Ni 85Co	16	20	16	41	6	53
30Ni 70Co	21	21	17	58	33	9
50Ni 50Co	29	29		62	38	
70Ni 30Co	23	23		93	7	
90Ni 10Co	48			100		
100 Ni	35			100		

This is probably because Ni^{2+} ions substitute for Co^{2+} ions in the cubic CoO (PDF: 00-043-1004) structure. The XRD patterns for these samples show the Co_3O_4 spinel phase and also the cubic CoO phase.

At higher nickel compositions the well-known NiO-CoO solid solution forms. The solid solution is clearly evident by the emergence of the peaks at 42.7° and 62.2° 2θ, which correspond to the CoO 200 and 220 reflections or the NiO 111 and 200 reflections.

The 50 mol % Ni sample shows only the NiO-CoO solid solution, with no evidence of Co_3O_4. This sample has five predominant peaks that form from overlapping reflections of both NiO and CoO. None of these peaks match any

single phase reflection exactly; they are negatively shifted for the NiO reflections and positively shifted for the CoO reflections. The cell parameters for this sample are α=β=γ=90°, a= 4.219 Å, which is the average value of the cell parameters of NiO and CoO.

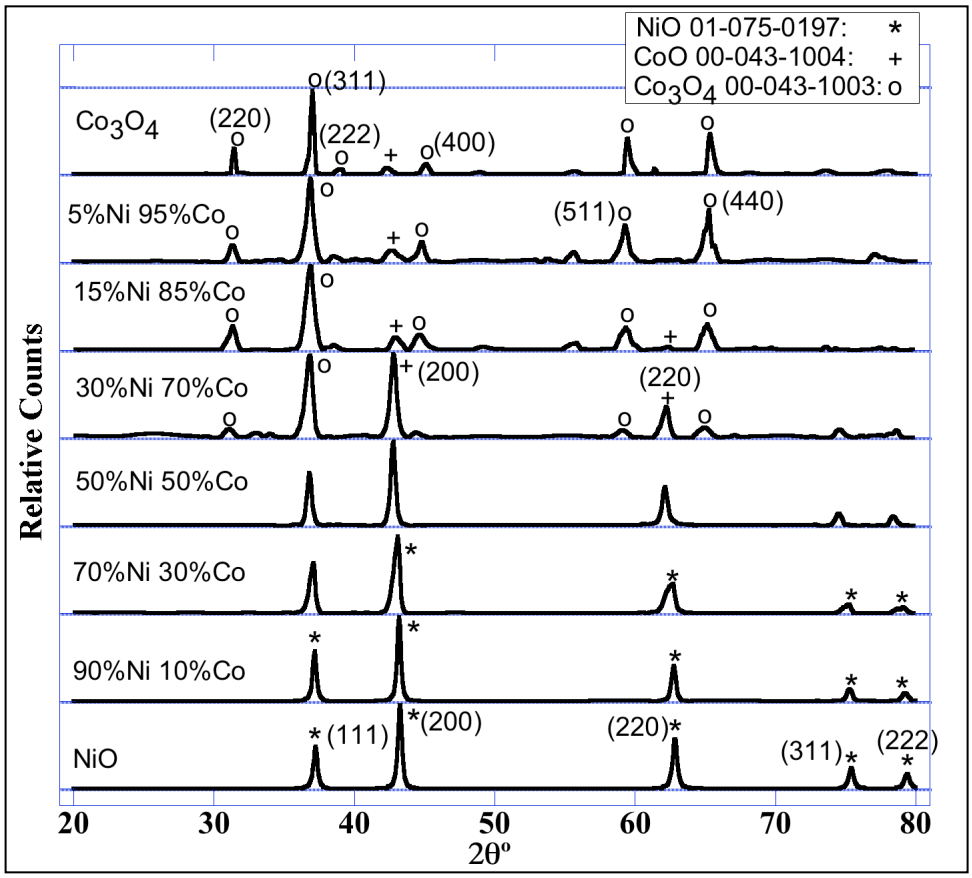

Figure 5-14. XRD patterns for the NiO-Co_3O_4 system.

The 70 mol % Ni sample is also a solid solution material with no peak exactly matching any reflection; most of these peak are slightly (~0.2θ°) shifted negatively. The two peaks at higher 2θ° values show some phase separation, both of them have two clear summits, each of which belongs to CoO and NiO respectively. Therefore phase separation occurs as the sample reaches its solubility limit.

The XRD patterns for the NiO-MoO_3 are shown in Figure 5-15. This graph is similar to Figure 5-14 in that it shows a gradual transition from pure orthorhombic MoO_3 (PDF# 98-000-0080) to pure cubic NiO. The spectra for the 75, 50, and 25 mol % MoO_3 show a mixture of two phases from the pure oxides.

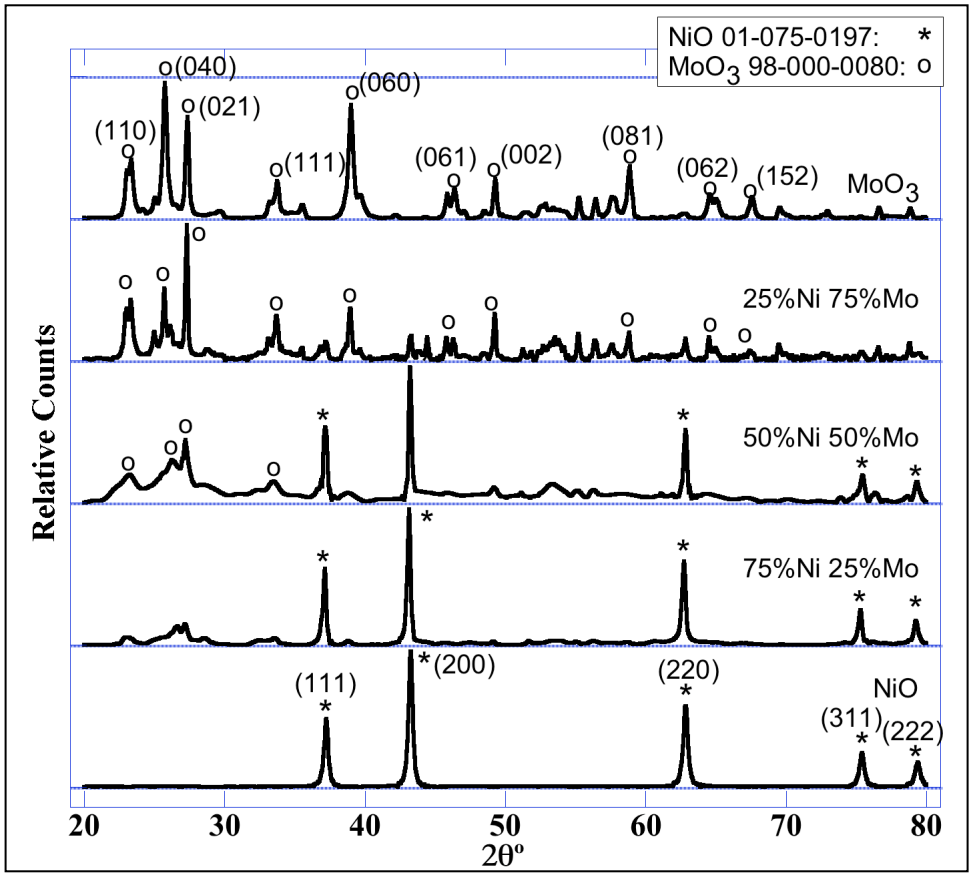

Figure 5-15. XRD spectra for the NiO-MoO_3 nanopowder system.

At higher NiO compositions, there is an obvious emergence of the five major NiO reflections (see above for 2θ° values) with a concomitant decrease in all the MoO_3 reflections.

Table 5-8 compares the theoretical mol % values and the values from phase simulation for the NiO-MoO_3 system. The values from phase simulations for the

NiO rich samples are higher than the expected theoretical ones. In particular, the 50 mol % NiO reveals a 66.4 mol % NiO, this is more than 30 % higher than the theoretical value. This difference is justified because the algorithm used to simulate phases is not a full Rietveld refinement but only an intensity-matching algorithm. The fact that there are crystallographic planes that have preferential growth in MoO_3 (see SEM images above) results in intensities in the powder diffraction patterns that do not match any reference cards used in the simulation. These uncharacteristic intensities skew the phase simulation results.

Table 5-8. Crystallite size and phase composition in the NiO-MoO_3 system from Jade calculations

Theoretical Mol %	Crystallite size (nm)		Simulation Mol % ±1.0	
	NiO	MoO_3	NiO	MoO_3
100 Mo		50		100
25Ni 75Mo	40	84	25	75
50Ni 50Mo	39	31	66	34
75Ni 25Mo	44	12	83	17
100 Ni	35		100	

Figure 5-16 presents the XRD spectra for the NiO-CuO. These samples with the exception of pure CuO (PDF: 04-004-4916) and pure NiO are either a series of mixed phases, or a solid solution. In the 75 mol % CuO sample, four distinct phases can be detected by de-convoluting the region between 34° and 46° 2θ of the spectrum. These phases are pure cubic CuO and cubic NiO and two polymorphs of Cu_2O (PDFs: 98-000-0041 and 00-035-1091). The reflections at 37° and 43° 2θ in the 75 and 50 mol % CuO have very broad shoulders from overlapping reflections of Cu_2O and NiO. The formation of the Cu_2O polymorphs is most probably due to the synthesis conditions of these materials.

In our experience sometimes the fast quench rates in the system do not allow the most stable oxide to form, giving rise to phases that are unknown or very rarely encountered.

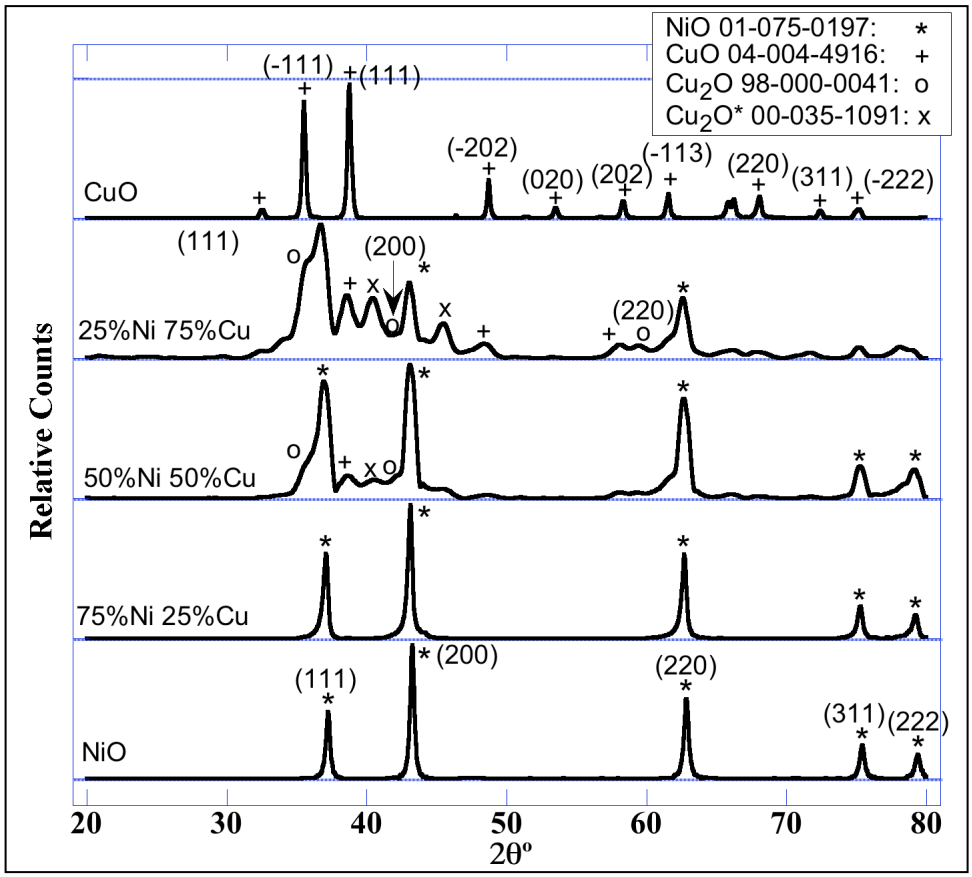

Figure 5-16. XRD spectra for the NiO-CuO nanopowder system

Table 5-9. Crystallite size and phase composition in the NiO-CuO system from Jade calculations

	Crystallite size (nm)			Simulation Mol % ±1.0		
	NiO	CuO	Cu_2O	NiO	CuO	Cu_2O
100 Cu		29			100	
25Ni 75Cu	28	14	19	38	40	22
50Ni 50Cu	25	17	22	63	16	11
75Ni 25Cu	26	29	30	96	2	2
100 Ni	35			100		

Samples with up to 25 mol % Cu show no crystalline CuO phases. This is probably because the Cu^{2+} ions substitute for Ni^{2+} ions in the NiO phase, forming the well-known solid solution.[48] Although it does form other phases; this system also exhibits the gradual transition of one pure phase to the other observed in the previous two systems discussed.

5.4. Conclusions

As with previous studies in our labs and others,[1-18] LF-FSP continues to offer the opportunity to produce single and mixed-metal oxide nanopowders with exceptional control of stoichiometry. The development of precursors and precise stoichiometric control has allowed us to systematically access any composition along any oxide phase space; albeit not always leading to single phase materials. The precursors used to synthesize these nanopowders are inexpensive and easily made. LF-FSP also offers the potential to access entirely new phases, typically kinetic phases rather than thermodynamic phases not accessible by standard synthesis and processing techniques.

This chapter demonstrates the use of LF-FSP to produce a series of nanopowders along the NiO-Co_3O_4, NiO-MoO_3, and NiO-CuO tie lines. Sixteen different samples were separately produced and analyzed by SSA, SEM, FTIR, TGA-DTA, and XRD.

The SSA of the NiO-Co_3O_4 decreases in the NiO rich samples while the opposite trend is observed in the NiO-CuO system. These results are likely a consequence of the formation of the high surface area Co_3O_4 spinel and the very low surface are Cu_2O phase. In general all 16 samples have SSAs about a third lower than those typically seen in other nanopowders containing NiO. Higher vapor pressures of the ions produced for the

transition metals studied in this chapter cause slightly larger particles leading to the lower SSA observed.

The unusual particle morphology seen in the NiO-MoO_3 system is attributed to the preferential growth of certain crystallographic planes in MoO_3. Along with some cubic particles seen in the NiO-Co_3O_4 system there is some phase separation in the as-produced materials, as evidenced by the dissimilar morphologies of the nanoparticles. These distinct phases are detected using XRD analysis and with corroboration from TGA events the original phase compositions can be ascertained. Finally, it is well known that the partial pressure of O_2 will affect the formation of a particular oxide as in the case of the NiO-CuO system.

5.5. Bibliography

1. C. R. Bickmore, K. F. Waldner, D. R. Treadwell, R. M. Laine "Ultrafine Spinel Powders by Flame Spray Pyrolysis of a Magnesium Aluminum Double Alkoxide," *J. Am. Ceram. Soc.,* 79 [5] 1419-1423 (1996).
2. A. C. Sutorik, S. S. Neo, D. R. Treadwell, R. M. Laine "Synthesis of Ultrafine β"-Alumina Powders via Flame Spray Pyrolysis of Polymeric Precursors," *Thermochim. Acta,* 81 [6] 1477-1486 (1998).
3. C. R. Bickmore, K. F. Waldner, R. Baranwal, T. Hinklin, D. R. Treadwell, R. M. Laine "Ultrafine Titania by Flame Spray Pyrolysis of a Titanatrane Complex," *J. Eur. Ceram. Soc.,* 18 [4] 287-297 (1998).
4. J. A. Azurdia, J. Marchal, P. Shea, H. Sun, X. Q. Pan, R. M. Laine "Liquid-Feed Flame Spray Pyrolysis as a Method of Producing Mixed-metal Oxide Nanopowders of Potential Interest as Catalytic Materials. Nanopowders Along the $NiO\text{-}Al_2O_3$ Tie Line Including $(NiO)_{0.22}(Al_2O_3)_{0.78}$, a New Inverse Spinel Composition," *Chem. Mater.,* 18 [3] 731-739 (2006).
5. J. A. Azurdia, J. Marchal, R. M. Laine "Synthesis and Characterization of Mixed-Metal Oxide Nanopowders Along the $CoOx\text{-}Al_2O_3$ Tie Line Using Liquid-Feed Flame Spray Pyrolysis," *J. Am. Ceram. Soc.,* 89 [9] 2749-2756 (2006).
6. W. J. Stark, R. Strobel, D. Gunther, S. E. Pratsinis, A. Baiker "Titania-Silica Doped with Transition Metals via Flame Synthesis: Structural Properties and Catalytic Behavior in Epoxidation," *J. Mater. Chem.,* 12 [12] 3620-3625 (2002).
7. K. K. Akurati, A. Vital, U. E. Klotz, B. Bommer, T. Graule, M. Winterer "Synthesis of Non-Aggregated Titania Nanoparticles in Atmospheric Pressure Diffusion Flames," *Powder Technol.,* 165 [2] 73-82 (2006).
8. L. Madler, A. Roessler, S. E. Pratsinis, T. Sahm, A. Gurlo, N. Barsan, U. Weimar "Direct Formation of Highly Porous Gas-sensing Films by in Situ Thermophoretic Deposition of Flame-Made Pt/SnO_2 Nanoparticles," *Sens. Actuators, B,* 114 [1] 283-295 (2006).
9. R. Jossen, M. C. Heine, S. E. Pratsinis, S. M. Augustine, M. K. Akhtar "Thermal Stability and Catalytic Activity of Flame-Made Silica-Vanadia-Tungsten Oxide-Titania," *Appl. Catal., B,* 69 [3-4] 181-188 (2007).
10. V. V. Srdic, M. Winterer "Comparison of Nanosized Zirconia Synthesized by Gas and Liquid Phase Methods," *J. Eur. Ceram. Soc.,* 26 [15] 3145-3151 (2006).
11. G. R. Patzke, A. Michailovski, F. Krumeich, R. Nesper, J. D. Grunwaldt, A. Baiker "One-Step Synthesis of Submicrometer Fibers of MoO_3," *Chem. Mater.,* 16 [6] 1126-1134 (2004).
12. H. Schulz, W. J. Stark, M. Maciejewski, S. E. Pratsinis, A. Baiker "Flame-Made Nanocrystalline Ceria/Zirconia Doped With Alumina Or Silica: Structural Properties and Enhanced Oxygen Exchange Capacity," *J. Mater. Chem.,* 13 [12] 2979-2984 (2003).
13. A. Teleki, S. E. Pratsinis, K. Kalyanasundaram, P. I. Gouma "Sensing of Organic Vapors by Flame-Made TiO_2 Nanoparticles," *Sens. Actuators, B,* 119 [2] 683-690 (2006).
14. M. T. Swihart "Vapor-Phase Synthesis of Nanoparticles," *Curr. Opin. Colloid Interface Sci.,* 8 [1] 127-133 (2003).

15. R. Burch, A. Collins "Characterization of Sulphided Ni/Mo/Alumina Hydrotreating Catalysts by Temperature Programmed Desorption and Reduction," *Applied Catalysis,* 18 [2] 373-387 (1985).
16. E. J. Albenze, A. Shamsi "Density Functional Theory Study of Hydrogen Sulfide Dissociation on Bi-metallic Ni-Mo Catalysts," *Surf. Sci.,* 600 [16] 3202-3216 (2006).
17. H. Jiang, H. Yang, R. Hawkins, Z. Ring "Effect of Palladium on Sulfur Resistance in Pt-Pd Bimetallic Catalysts," *Catal. Today,* 125 [3-4] 282-290 (2007).
18. J. R. Gonzalez-Velasco, J. A. Botas, R. Ferret, G.-M. Pilar, M., J.-L. Marc, M. A. Gutierrez-Ortiz "Thermal Aging of Pd/Pt/Rh Automotive Catalysts Under a Cycled Oxidizing-Reducing Environment," *Catal. Today,* 59 [3-4] 395-402 (2000).
19. W. J. Zhou, W. Z. Li, S. Q. Song, Z. H. Zhou, L. H. Jiang, G. Q. Sun, Q. Xin, K. Poulianitis, S. Kontou, P. Tsiakaras "Bi- and Tri-metallic Pt-based Anode Catalysts for Direct Ethanol Fuel Cells," *J. Power Sources,* 131 [1-2] 217-223 (2004).
20. P. Biedenkopf, M. M. Bischoff, T. Wochner "Corrosion Phenomena of Alloys and Electrode Materials in Molten Carbonate Fuel Cells," *Mater. Corros.,* 51 [5] 287-302 (2000).
21. E. Shinova, E. Zhecheva, R. Stoyanova, G. D. Bromiley, R. Alcantara, J. L. Tirado "High-Pressure Synthesis and Electrochemical Behavior of Layered (1-*a*)$LiNi_{1-y}Al_yO_2$•*a*$Li[Li_{1/3}Ni_{2/3}]O_2$ Oxides," *J. Solid State Chem.,* 178 [9] 2692-2700 (2005).
22. S. H. Ju, H. C. Jang, Y. C. Kang "Al-doped Ni-rich Cathode Powders Prepared From the Precursor Powders with Fine Size and Spherical Shape," *Electrochim. Acta,* 52 [25] 7286-7292 (2007).
23. F. GarcÌa-Ochoa, A. Santos "Coke Effect in Mass Transport and Morphology of Pt-Al_2O_3 and Ni-Mo-Al_2O_3 Catalysts," *AIChE J.,* 42 [2] 524-531 (1996).
24. J. R. Grzechowiak, I. Wereszczako-Zielinska, K. Mrozinska "HDS and HDN Activity of Molybdenum and Nickel-Molybdenum Catalysts Supported on Alumina-Titania Carriers," *Catal. Today,* 119 [1-4] 23-30 (2007).
25. M. A. Dominguez-Crespo, E. M. Arce-Estrada, A. M. Torres-Huerta, L. Diaz-Garcia, M. T. Cortez de la Paz "Support Effects on Hydrotreating Activity of NiMo Catalysts," *Materials Characterization,* 58 [10] 864-873 (2007).
26. A. C. W. Koh, L. Chen, L. Kee, Weng, B. F. G. Johnson, T. Khimyak, J. Lin "Hydrogen or Synthesis Gas Production via the Partial Oxidation of Methane Over Supported Nickel-Cobalt Catalysts," *Int. J. Hydrogen Energy,* 32 [6] 725-730 (2007).
27. J. Laine, J. L. Brito, F. Severino "Structure and Activity of NiCo-Mo/SiO_2 Hydrodesulfurization Catalysts," *J. Catal.,* 131 [2] 385-393 (1991).
28. L. Kaluza, M. Zdrazil "Preparation of Zirconia-Supported Hydrodesulphurisation Catalysts by Water-Assisted Spreading," *Applied Catalysis A,* 329 58-67 (2007).
29. C. M. C. Romero, J. W. Thybaut, G. B. Marin "Naphthalene Hydrogenation Over a NiMo/γ-Al_2O_3 Catalyst: Experimental Study and Kinetic Modelling," *Catal. Today,* 130 [1] 231-242 (2008).

30. M. J. Illan-Gomez, S. Brandan, d. L. Salinas-Martinez, C., A. Linares-Solano "Improvements in NOx Reduction by Carbon Using Bimetallic Catalysts," *Fuel,* 80 [14] 2001-2005 (2001).
31. *"Table 3.2 Physical Constants of Inorganic Compounds", Lange's Handbook of Chemistry*; McGraw-Hill: New York, 1999.
32. Schlesinger,M. E. *"Melting Points, Crystallographic Transformation, and Thermodynamic Values," Engineered Materials Handbook*; ASM International: Metals Park, Ohio, 1991; pp 883-891.
33. H. W. Foote, E. K. Smith "On the Dissociation Pressures of Certain Oxides of Copper, Cobalt, Nickel and Antimony," *J. Am. Chem. Soc.,* 30 [9] 1344-1350 (1908).
34. M. Oku, Y. Sato "In-Situ X-Ray Photoelectron Spectroscopic Study of the Reversible Phase Transition Between CoO and Co_3O_4 in Oxygen of 10^{-3} Pa," *Appl. Surf. Sci.,* 55 [1] 37-41 (1992).
35. E. J. Grimsey, K. A. Reynolds "Equilibrium Oxygen Pressure of (Co_3O_4 + CoO) From 1173 to 1228 K," *J. Chem. Thermodyn.,* 18 [5] 473-476 (1986).
36. J. Sun, S. L. Simon "The Melting Behavior of Aluminum Nanoparticles," *Thermochim. Acta,* 463 [1-2] 32-40 (2007).
37. P. Zeng, S. Zajac, P. C. Clapp, J. A. Rifkin "Nanoparticle Sintering Simulations," *Mater. Sci. Eng. A,* 252 [2] 301-306 (1998).
38. N. Floquet, O. Bertrand, J. J. Heizmann "Structural and Morphological Studies of the Growth of MoO_3 Scales During High-temperature Oxidation of Molybdenum," *Oxid. Met.,* 37 [3] 253-280 (1992).
39. J. Nowotny, M. Rekas "Defect Structure of Cobalt Monoxide: I, The Ideal Defect Model," *J. Am. Ceram. Soc.,* 72 [7] 1199-1207 (1989).
40. M. Kinoshita, W. D. Kingery, H. K. Bowen "Phase Separation in NiO-CoO Solid-Solution Single-Crystals," *J. Am. Ceram. Soc.,* 56 [7] 398-399 (1973).
41. G. W. Smith "The Crystal Structures of Cobalt Molybdate $CoMoO_4$ and Nickel Molybdate $NiMoO_4$," *Acta Crystallogr.,* 15 [10] 1054-1057 (1962).
42. R. M. Laine, J. C. Marchal, H. P. Sun, X. Q. Pan "Nano-α-Al_2O_3 by Liquid-Feed Flame Spray Pyrolysis," *Nat. Mater.,* 5 [9] 710-712 (2006).
43. V. Biju, M. A. Khadar "Fourier Transform Infrared Spectroscopy Study of Nanostructured Nickel Oxide," *Spectrochim. Acta A-M,* 59 121-134(14) (2003).
44. P. Nkeng, J. F. Koenig, J. L. Gautier, P. Chartier, G. Poillerat "Enhancement of Surface Areas of Co_3O_4 and $NiCo_2O_4$ Electrocatalysts Prepared by Spray Pyrolysis," *J. Electroanal. Chem.,* 402 [1-2] 81-89 (1996).
45. C. Rocchiccioli-Deltcheff, M. Amirouche, M. Che, J.-M. Tatibouet, M. Fournier "Structure and Catalytic Properties of Silica-Supported Polyoxomolybdates I. Mo/SiO_2 Catalysts Prepared From Hexamolybdate," *J. Catal.,* 125 [2] 292-310 (1990).
46. M. M. Mohamed, G. M. S. E. Shafei "Fourier-Transform Infrared/Photoacoustic Study of Pyridine Adsorbed on Silica Supported Copper-Molybdenum Catalysts," *Spectrochim. Acta A-M,* 51 [9] 1525-1531 (1995).
47. G. Kliche, Z. V. Popovic "Far-Infrared Spectroscopic Investigations on CuO," *Phys. Rev. B: Condens. Matter,* 42 [16] 10060-10066 (1990).

48. A. D. Kulkarni, R. E. Johnson "Thermodynamic Properties of Liquid Cu-O, Cu-O-Ni, and Cu-O-Fe Systems," *JOM-J. Mim. Met. Mat. S.,* 22 [12] A27 (1970).

Chapter 6.

Comparative Study of Two Routes to Bi-Phasic Nano Composites of Y_2O_3 and MgO Nanopowders

6.1. Introduction

The materials and processes needed to develop transparent submicron grained, or even nano crystalline ceramics are of great commercial and academic research interest for applications such as ceramic lasers, radomes, envelopes for high intensity discharge lamps, and heat-resistant windows.[1-4] Currently available mid-IR transparent materials used for infrared windows and radomes (radar domes) face increasing performance demands in terms of their transparency (theoretical transmission of ~85% at all wavelengths) and mechanical strength (compressive strength of α-A_2O_3 at room temperature ~2.0 GPa).[5]

The primary transparent ceramic materials commercialized thus far for IR domes are: sapphire (α-A_2O_3), spinel ($MgAl_2O_4$), AlON, and yttria (c-Y_2O_3).[6-9] Sapphire is the currently material of choice because of its high strength and acceptable but not optimal transparency window. Sapphire loses mechanical strength at temperatures >600 °C (down to ~60 MPa).[10] Polycrystalline sapphire has limited inline transmission due to birefringence of individual grains (up to ~83% at 4.5 μm, but droping precipitously to 0% at ~7.5 μm).[11] Birefringence is caused by a different index of refraction along the "a" and "c" crystallographic axes. These shortcomings have led researchers to explore other materials as alternatives to sapphire, including CVD diamond, ZnS and MgO-Y_2O_3

composites.[12-14] Yttria has a wide IR window from ~0.1 to 6.5 μm, but mechanical properties inferior to sapphire. The incorporation of a second phase (MgO), may result in better mechanical behavior, as discussed below. In order for MgO-Y_2O_3 composites to be used as transparent ceramics, the grain sizes of these materials must be much smaller than the wavelengths of the light of interest (~30 to 100 nm for IR).

The motivation for using composite materials comes from the fact that second phase particles in ceramics are known to improve mechanical properties.[15] For example, 5 vol. % nano-SiC in Al_2O_3 increases its compressive strength from 500 to 1000 MPa.[16] Al_2O_3:YAG 1:1 vol. % composites have much lower creep rates ($3E^{-8}$ sec^{-1}), than Al_2O_3 or YAG alone, respectively $1E^{-5}$ sec^{-1} and $4E^{-6}$ sec^{-1}.[17] Toughening of Al_2O_3 by ZrO_2, (ZTA) is a well know example of material property enhancement by a secondary phase, where values as high as 12.6 MPa $m^{1/2}$ have been reported.[18] Second phase particles also inhibit grain growth leading to relatively finer microstructures,[19] which provide higher strengths, hardness, toughness and improved transparency.[20]

6.2. Background

There is considerable literature on ceramic nano-composites but in reality most of these materials are only reinforced or modified by nano sized inclusions in a matrix with feature sizes >0.2 μm.[21-27] Few reports describe true ceramic "nano-nano" composites wherein both phases have grain sizes near or below 100 nm. For example Bhaduri et. al. describe Al_2O_3 and ZrO composites, with 44 and 14 nm average grain sizes (AGSs), from XRD and TEM analysis.[28] Duan et. al describe Al_2O_3 and TiO_2 nanocomposites formed via a high pressure sintering, with AGSs ~180 nm from HR-TEM images.[29] Liu et. al.

describe making nano α-Fe_2O_3 and α-Al_2O_3 composites with AGSs of 23 and 46 nm from XRD analyses.[30]

Kear et. al.[31] reported processing 50:50 and 20:80 mol % Y_2O_3:MgO samples using spray-dried, aggregated parent oxide powders and melting them via an Ar-10% H_2 plasma torch followed by a fast quench. These powders were consolidated by uniaxial pressing (25 MPa) followed by CIPping (200 MPa). The pellets were heat treated at 1600 °C for 5 h. in air followed by HIPping at 1400°C for 2 h. at 200 MPa of Ar to achieve 95–99% of theoretical density. The AGS for each phase is approximately 0.4 μm. The fracture toughness values reported range from 1.15 to 1.09 MPa•$m^{1/2}$ (range within error bars) an increase of ~20% above the fracture toughness of pure yttria. Most importantly, the in-line IR transmission is approximately 55% at 6 μm.

Stefanik et.al. described sets of MgO and Y_2O_3 nano composite materials with 200 nm AGSs and near theoretical transmissions of ~84% in the 3–5 μm mid-IR range.[32] These results were reportedly attained by "standard ceramic consolidation" of metastable powders synthesized by an undisclosed, proprietary method. The publication does not elaborate nor give any more experimental details regarding the synthesis of such nano composites.

6.3. LF-FSP

There appears to be considerable room for improvement, perhaps via LF-FSP derived nanopowders. Three main particle formation paths can be envisioned to occur in LF-FSP processing of mixed metal precursors. Particle formation in LF-FSP is follows a general pathway where the liquid feed produces fine droplets that vaporize and ignite. The organic ligands are expected to combust simultaneously with the fuel (EtOH), resulting in

metallo-oxy species in the gas phase. These species condense forming nanoparticles that grow until either the temperature drops, limiting diffusion for that particular species or its concentration in the gas phase falls below a limiting one. The distinction of particular pathways is dependent on this last step. The condensation temperature and particle growth rates of a particular species determine which oxide forms and also the relative time at which it forms. Different precursor chemistries have different energetic values per mole that lead to different combustion temperatures and/or decomposition rates, which in turn affect the particle formation pathways.

The simplest pathway should result in the formation of single phase individual particles, with no compositional differences. The single phase spinel materials studied in Chapters 3 and 4, show that multi metallic precursors indeed form single phase oxide nanoparticles. Particles formed following this pathway are single grains or crystallites.

A second path is the formation of a bi-phasic mixture, in which individual particles are a single phase but not all particles have the same composition. The NiO-MoO_3 system discussed earlier, where each particle is a distinct phase is an example of such a path. Each particle resulting form this pathway is also single grains or crystallites.

The third particle formation path also forms a bi-phasic mixture but this time in the form of a core-shell structure. Each individual particle consists of the two phases wherein there is a distinct intra-particle boundary. These particles contain multiple grains, typically two grains.

Work on ZrO_2-Al_2O_3 oxide system produced by LF-FSP, not presented in this dissertation, shows that because Al_2O_3 has a lower vaporization temperature (3000 °C) than ZrO_2 (5155 °C), ZrO_2 should condense and nucleate first from the gas phase

followed by Al_2O_3.[33] The ZrO_2 nanoparticles form first during quenching, then Al_2O_3 nucleates on the ZrO_2 nanoparticles forming the observed bi-phasic core-shell nanopowders in a single step.

The possibility of intimate mixing at nanometer length scales, observed in these bi-phasic materials, enables the formation of true nano-nano composites. This chapter continues work exploring the use of LF-FSP for the production of specific two-phase nanopowders in the phase space between Y_2O_3 and MgO.

Yttria and magnesia each have a cubic crystallographic phase that eliminates optical anisotropy, offering good prospects for creating transparent nano-nano composites. Each constituent phase MgO[34] and Y_2O_3[35,36] can be processed to transparency, an important goal of the intended work.[37] The three main reasons for choosing this binary oxide system are immiscibility, potential for transparency and mechanical characteristics suitable for structural applications.[38,39]

Yttria and magnesia have very limited solid miscibility, (~7 mol % MgO in Y_2O_3 and ~1 mol % Y_2O_3 in MgO) allowing a wide range of mixed compositions to be studied particularly below the solidus temperature (2110 °C). Figure 6-1 presents the published phase diagram of the pseudo eutectic oxide system.[40] It is evident from the phase diagram that the miscibility for either end-member is negligible below 1500 °C.

Thus, the overall goal of this work was to identify an optimal set of materials to produce transparent nano-nano composites. Additionally, this chapter compares and contrasts the nano powder characteristics from two different sets of materials, produced from two distinct routes. The first route is considered a mixing route, while the second one is a direct synthesis method. The mixing route involves ball-milling mixtures of the

parent nano oxides (Y_2O_3 and MgO) while the synthesis route co-dissolves the precursors for the individual components in a single ethanol solution which is then processed in LF-FSP.

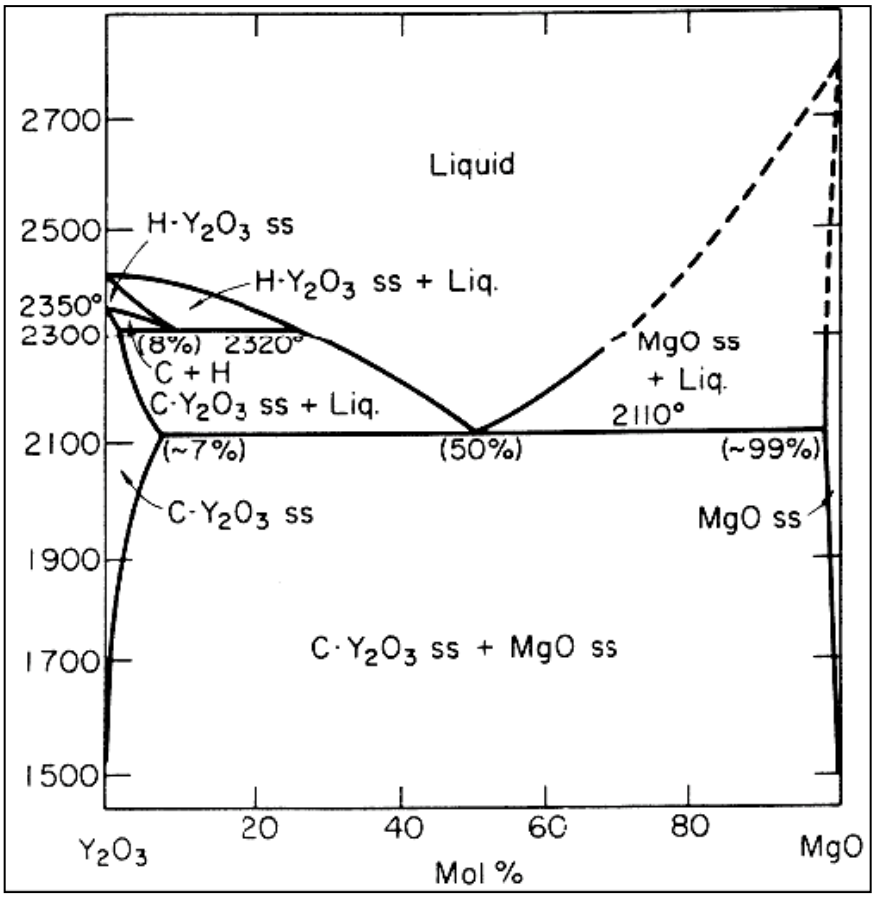

Figure 6-1. Published phase diagram of the Y_2O_3-MgO system

Ball milling is a simple, effective method of producing homogeneous mixtures. A low speed jar mill (60–80 rev./min) was chosen rather than high energy or planetary mills to minimize any solid state reactions of the parent oxides.[41,42] In the second synthesis route, different amounts of precursors to the single oxides are mixed thoroughly in solution before LF-FSP processing. The two routes permit a direct comparison of the effectiveness of LF-FSP to produce in a single step material similar to traditionally mixed

ones. Altogether sixteen individual samples were produced via liquid-feed flame spray pyrolysis (LF-FSP) and analyzed by XRD, SSA, SEM, FTIR, TGA and dilatometry.

6.4. Experimental

6.4.1. Materials

Magnesium chips [Mg, 99.98%], propionic acid [$CH_3CH_2CO_2H$, 99^+%], and anhydrous ethanol [CH_3CH_2OH, 99.99^+%] were purchased from Sigma-Aldrich and used as received. Yttrium nitrate hexahydrate [$Y(NO_3)_2 \bullet 6H_2O$, 99.99%], was purchased from PIDC (Ann Arbor, MI) dissolved in DI water and filtered to remove any insoluble impurities before using.

6.4.2. Precursor formulations

Yttrium precursor was prepared by dissolving 1.0 kg (2.98 moles) of $Y(NO_3)_2 \bullet 6H_2O$ in 200 mL of DI water and filtering through a 2 μm filter. The solution was placed in a 5000 mL flask equipped with a still head and an N_2 sparge. Propionic acid (3.0 L, 13.59 moles) was added and the resulting solution heated to ~150°C for 10 h, after which ~1.5 L of liquid (water/propionic acid) was distill off. The N_2 sparge was used to stir the reaction and coincidentally remove any evolved NOx gas. The volume of the remaining liquid product was reduced using a rotary evaporator until a viscous yellow liquid formed. The viscous liquid was placed in clean 500 ml Nalgene® bottles and allowed to cool to T_{Rm}, where it formed a white solid. The ceramic loading of the solid was determined by thermo gravimetric analysis (TGA), wherein a 10 mg sample was heated in air to 1000 °C at 10 °C/min, the final yield was 31.2 wt. %. This procedure was repeated three times to synthesize

enough precursor (~ 10 moles of yttrium) to produce all the samples (See Table 6-1 for compositions).

Table 6-1. Sample compositions for both ball milled and mixed routes

Sample	Mol % Y_2O_3	Mol % MgO
10Y	10	90
40Y	40	60
50Y	50	50
67Y	67	33
90Y	90	10
95Y	95	5
98Y	98	2

The magnesium precursor was synthesized by reacting 50 g (2.06 moles) of magnesium chips with 750 mL (3.40 moles) of propionic acid. The reaction was continuously sparged with N_2 to prevent H_2 build-up and to help stir the reactants. The resulting white precipitates where rinsed with excess propionic acid and collected in a 500 mL Nalgene. This procedure was repeated five times and the product of the reaction collected in the same jar. The excess propionic acid in the final solution was removed using a rotary evaporator, until a white solid formed. The ceramic yield of the solid was also determined by TGA and found to be 15.7 wt. %.

6.4.3. Ball mill processing

Precise amounts of the two parent oxides (Y_2O_3 and MgO) were measured and dispersed in ethanol using an ultrasonic horn, for example the 40Y ball-milled sample had 6.45 g of Y_2O_3 and 1.73 g of MgO (see Chapter 2 for processing details) The dispersions were then placed in 500 ml Nalgene jars and ball milled in a low speed jar mill for <24 h. The jars contained 150 ml (30 vol. %) of high purity, fully dense yttria stabilized zirconia (YSZ) spherical (dia. 3 mm) milling media. The dispersions were

removed from the jars and allowed to dry in a re-circulating air oven at 70–100 °C overnight. The dried powders were ground in an alumina mortar and pestle and then sieved using a -200 mesh nylon sieve.

6.5. Results and Discussion

The overall goal of this study is to produce optically and IR transparent nano-nano composite ceramics for applications in infrared windows and domes. The work reported here serves as a baseline study to identify an optimal set of nanopowders to produce nano-nano transparent monoliths. The results obtained demonstrate the ability of LF-FSP to produce controlled bi-phasic nanopowders along the MgO-Y_2O_3 tie-line.

The two sets of nanopowders produced were characterized using a variety of techniques, including XRD, SSA, SEM, FTIR, TGA and dilatometry. The work reported here starts with a study of the phases present and crystallite sizes observed followed by a discussion on specific surface areas, particle morphologies, size and size distributions, and the presence of surface species. The thermal behavior of each nanopowder set is then discussed. Finally some of the sintering characteristics of the nanopowders produced are discussed.

The two different routes examined provide materials with very similar properties, although some differences have been found primarily in the amount of surface species present in the ball-milled set. All of the nanopowders, regardless of which route they were produced from have no microporosity and are mostly spherical. Both sets of powders have some soft agglomerates but there are no microns sized primary

particles. Contrasting the thermal behavior of the two sets of different nanopowders, a clear difference in mass loss events is observed.

6.5.1. Powder Characterization

6.5.1.1. X-ray powder diffraction

XRDs patterns for all the ball-milled samples are presented in Figure 6-2. The average crystallite sizes (XSs), from Debye-Scherrer XRD line-broadening analyses, and a phase analysis from whole pattern refinement (WPR) using Jade 8.5 are presented in Table 6-2.

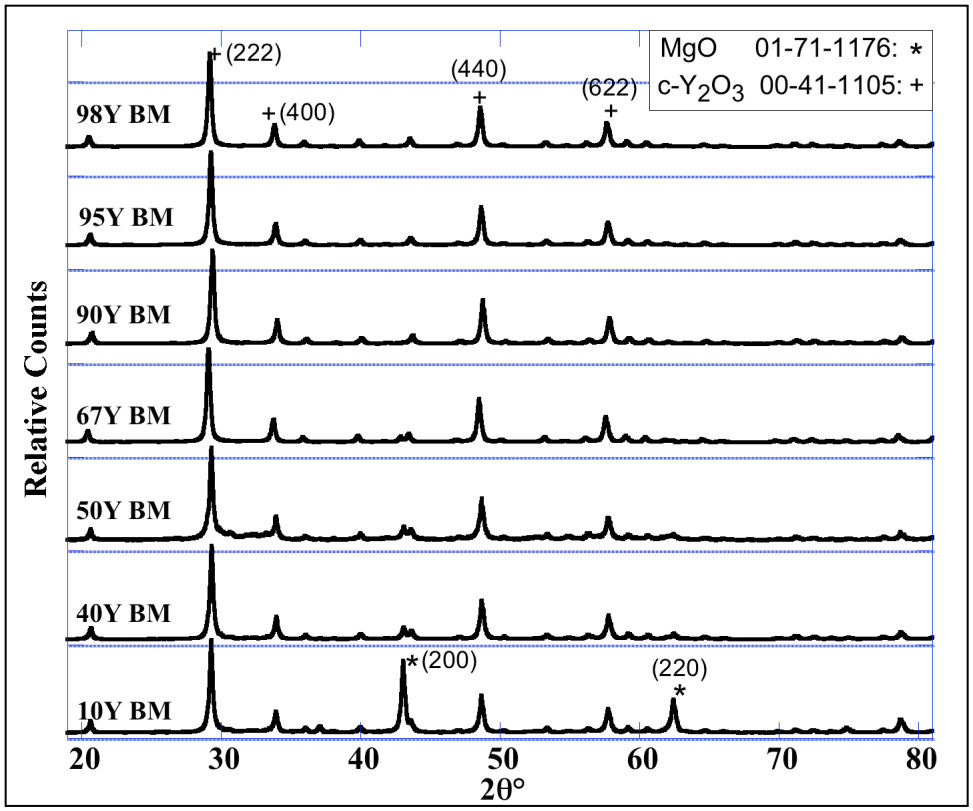

Figure 6-2. XRD patterns for all ball-milled nanopowders

Table 6-2. Phase composition and crystallite sizes of all ball-milled samples from whole pattern refinements using Jade 8.5

Ball-Milled Samples	Phase wt. % ±1		Crystallite Size (nm) ±2	
	c-Y_2O_3	MgO	c-Y_2O_3	MgO
10Y	55	45	51	80
40Y	78	22	48	71
50Y	85	15	42	49
67Y	90	10	51	71
90Y	96	4	45	20*
95Y	99	1	48	53*
98Y	100	0	52	

*The error in content phase fitting is ±1 % for the particular parameters chosen. Because the phase fitting algorithm has assigned a value to that phase, it must also assign it a crystallite size, therefore these values are unreliable.

Figure 6-3 shows the XRD patterns for all the mixed precursor nanopowders, their phase compositions and crystallite sizes are presented in Table 6-3.

Samples that have up to 10 mol % magnesia do not show any crystalline MgO reflections because of magnesias's low reference intensity ratio, RIR, also signified by I/I_c where *c* refers to corundum, the standard used currently),[43] when compared to that of yttria (RIR of MgO =3.28, and Y_2O_3 = 9.1). All of the other samples exhibit the expected MgO and Y_2O_3 two-phase mixed XRD patterns. There is a gradual increase in the intensity of all the MgO reflections, as more magnesia is added, but the Y_2O_3 peaks do not diminish in intensity due to the large difference (~5.8) in RIR between the two phases.

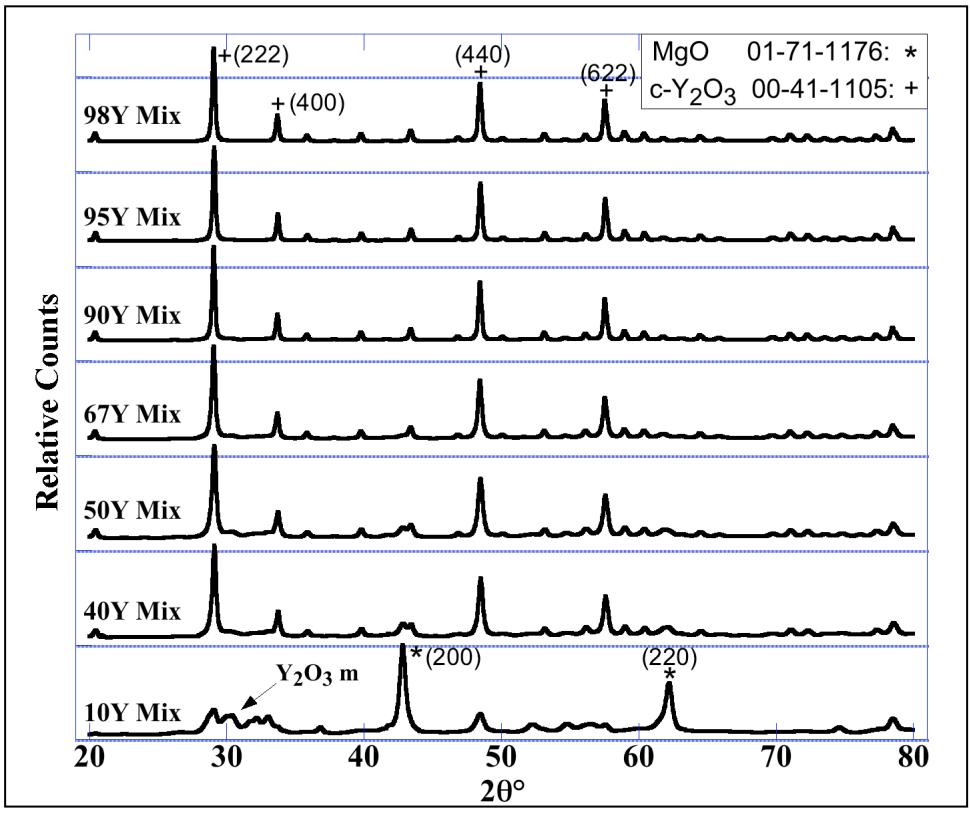

Figure 6-3. XRD patterns for all as-produce mixed precursor nanopowders

The high MgO content samples of the mixed precursor set, present a third phase assigned to monoclinic yttria, (PDF# 00-44-0399). The formation of this phase has been attributed to low temperature flames in similar flame synthesis methods or to high pressure atmospheres in plasma synthesis routes.[44-47]

Overall, the actual compositions from phase analysis of both synthesis routes agree well with the intended ones. Figure 6-4 compares the theoretical wt. % MgO and the calculated values (from XRD) for all the samples. The values from the mixed precursor sample are all slightly higher, perhaps due to a lower ceramic yield of the MgO precursor. The calculated values for the ball-milled materials agree well with the theoretical ones, with the exception of the

10 mol % Y_2O_3 sample which has considerable less MgO than what was intended.

Table 6-3. Phase composition and crystallite sizes of all mixed precursor samples from whole pattern refinements using Jade 8.5

Mixed Precursor Samples	Phase wt. % ±1			Crystallite Size (nm) ±2		
	c-Y_2O_3	MgO	m-Y_2O_3	c-Y_2O_3	MgO	m-Y_2O_3
10Y	5	67	28	21	19	12
40Y	54	30	16	32	16	14
50Y	65	23	12	33	15	20
67Y	78	14	8	51	9	19
90Y	85	11	4	110	5	32
95Y	96	4		120	5	
98Y	100			84		

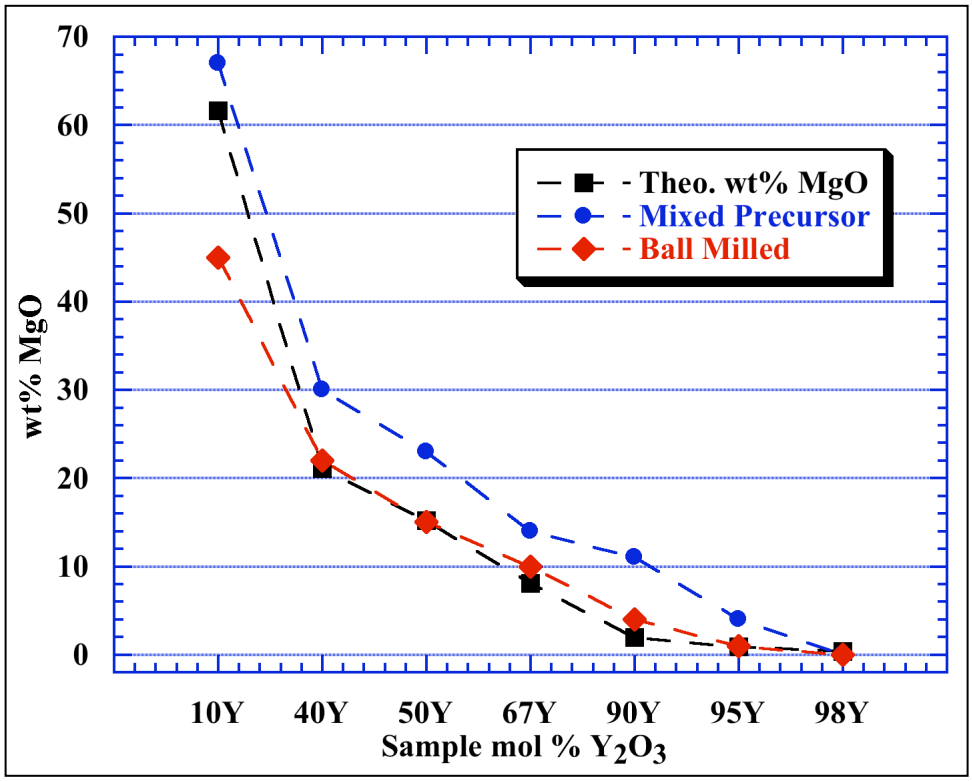

Figure 6-4. Comparison of wt. % MgO calculated from phase analysis for all samples

6.5.1.2. Surface areas analyses

Specific surface area analyses of all ball-milled and mixed precursor samples are shown in Table 6-4. Microporosity was not expected nor detected from T-plot isotherm analyses for any of the samples, scanning electron micrographs (SEMs) corroborate that all of the samples regardless of preparation route consist of solid primary nanoparticles (see below). The specific surface areas for all samples are between 16 and 49 m^2/g, which correspond to average particle sizes (APS) between 30 and 73 nm.

Table 6-4. Specific surface areas and average particle sizes of all samples

Sample	Ball Milled		Mixed Precursor	
	SSA (m^2/g) ±1.0	APS (nm)	SSA (m^2/g) ±0.5	APS (nm)
10Y	22	68	49	30
40Y	25	52	33	39
50Y	26	48	32	40
67Y	32	39	29	42
90Y	29	42	20	61
95Y	28	43	16	73
98Y	35	34	16	73

The SSAs for the mixed precursor samples decrease towards the Y_2O_3 rich samples, while no clear trend is seen for the ball-milled samples. The lack of a trend for the ball-milled samples is most likely due to the MgO being reactive because of its relatively high surface area.[48-50] As FTIR and TGA results show (see below), these samples all absorb up to 10 wt. % of carbonates, indicating that their surfaces are more active than the mixed precursor samples. The surface areas for pure MgO and Y_2O_3 are 42 and 22 m^2/g, respectively.

The mixed precursor samples follow an expected trend, from a simple rule of mixtures, with the MgO rich samples having higher surface areas than the

Y_2O_3 rich ones. The slightly decreased surface areas observed for the 95 and 98 mol % Y_2O_3 are a result of larger particles (see XSs sizes above). The larger particles are likely caused be inevitable variations in the gas flow of the LF-FSP reaction chamber and powder collection system (see Chapter 2).

6.5.1.3. Scanning electron microscopy

Scanning electron micrographs (SEMs) were taken to assess the particle size distributions and morphologies of both sets of nanopowders produced. All of the nanopowders observed mostly exhibit spherical morphologies and very uniform primary powder sizes. The SEMs show that the primary particle populations of the produced materials do not include any obvious micron size particles. Figure 6-5 through Figure 6-8 show SEM images for the ball-milled samples.

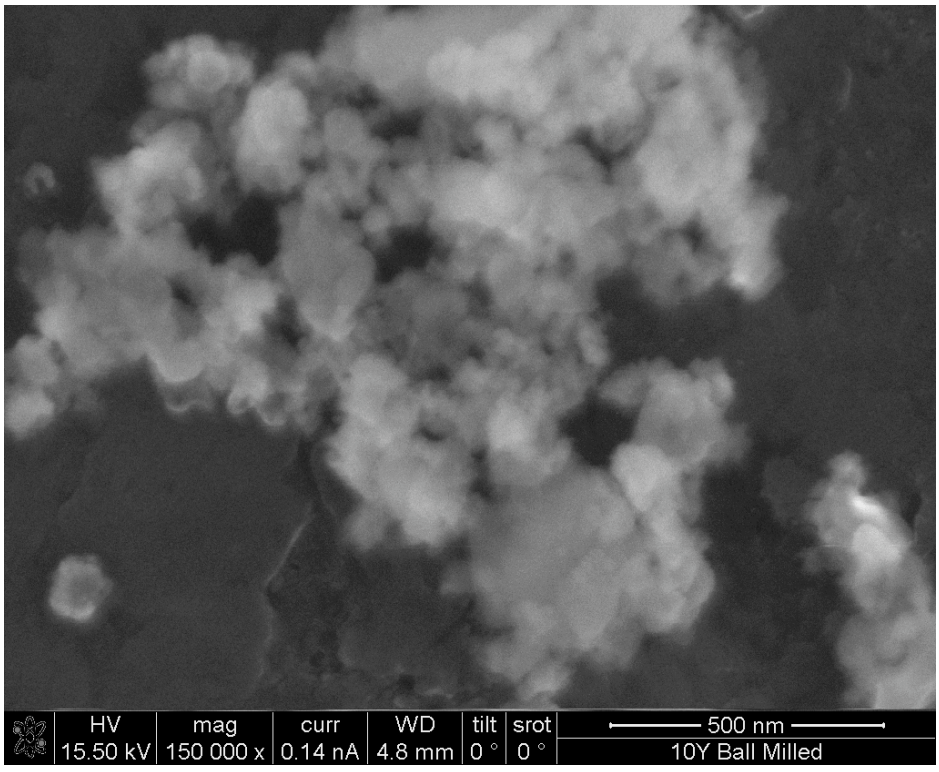

Figure 6-5. SEM image of the 10Y ball milled sample

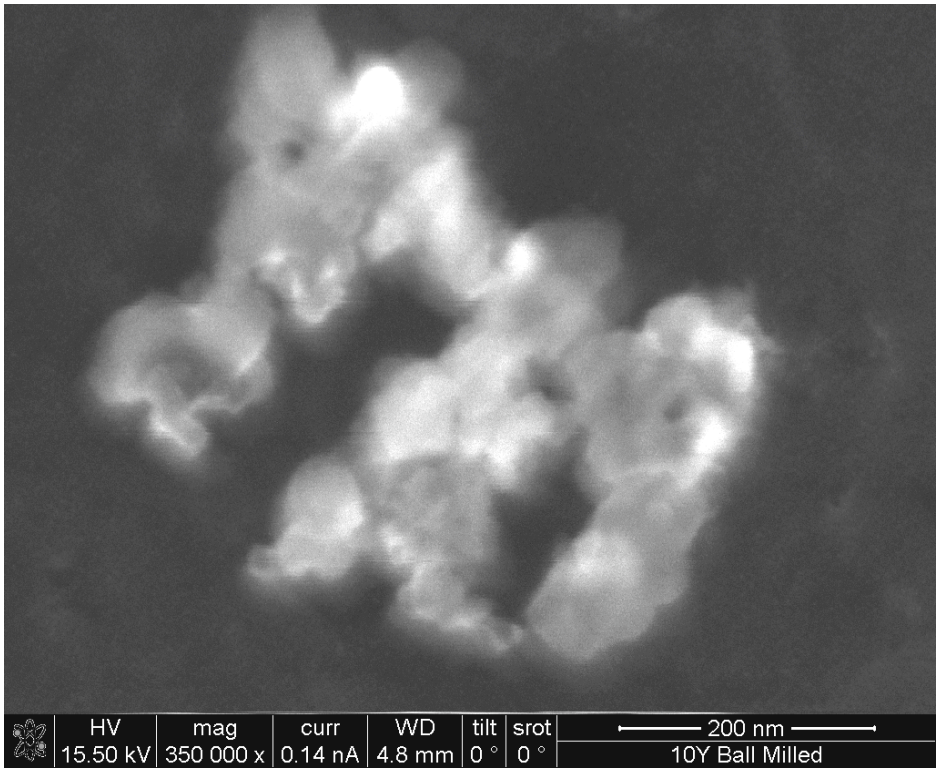

Figure 6-6. SEM image showing primary nanoparticles in the 10Y sample

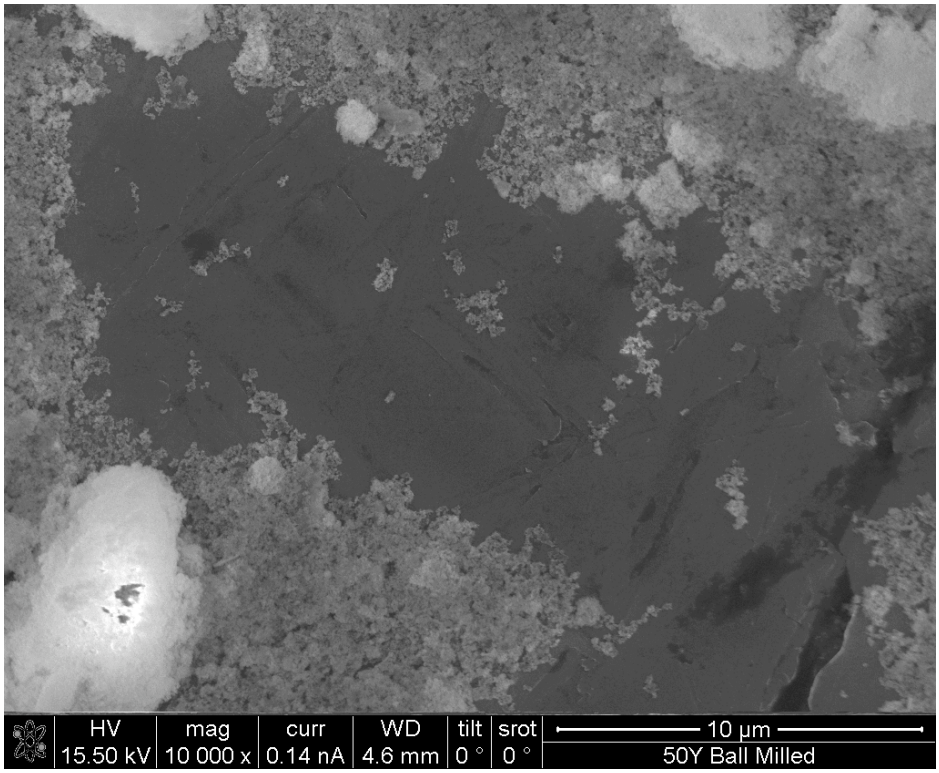

Figure 6-7. SEM image of the 50Y ball-milled sample showing large aggregates

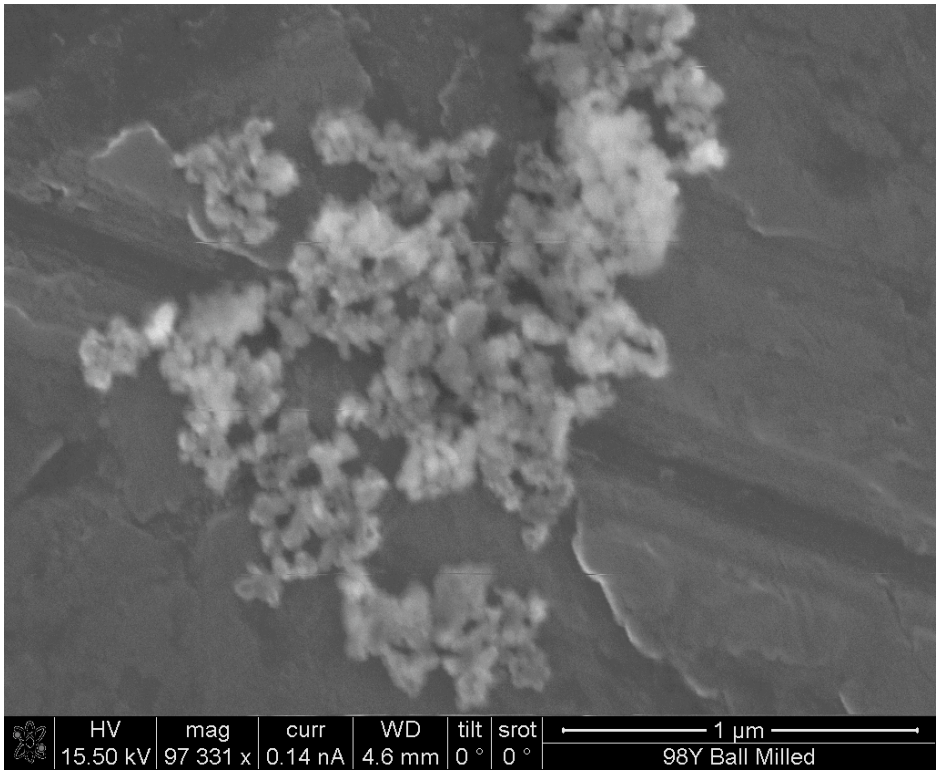

Figure 6-8. SEM image of the 98Y ball-milled sample

The SEM images for the mixed precursor set of powders are presented in Figure 6-9 through Figure 6-11. These images are representative for all other compositions in this set of materials and show particle size homogeneity and morphology. The images below show mostly agglomerated or slightly aggregated particles with very few outliers

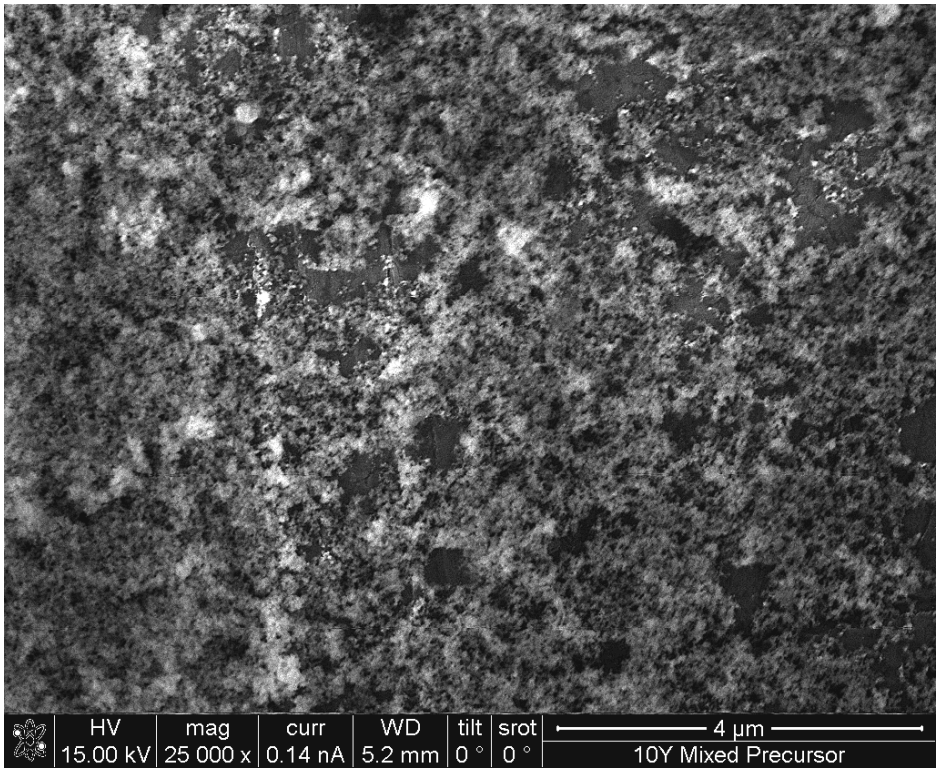

Figure 6-9. SEM image of 10Y as-produced mixed precursor sample

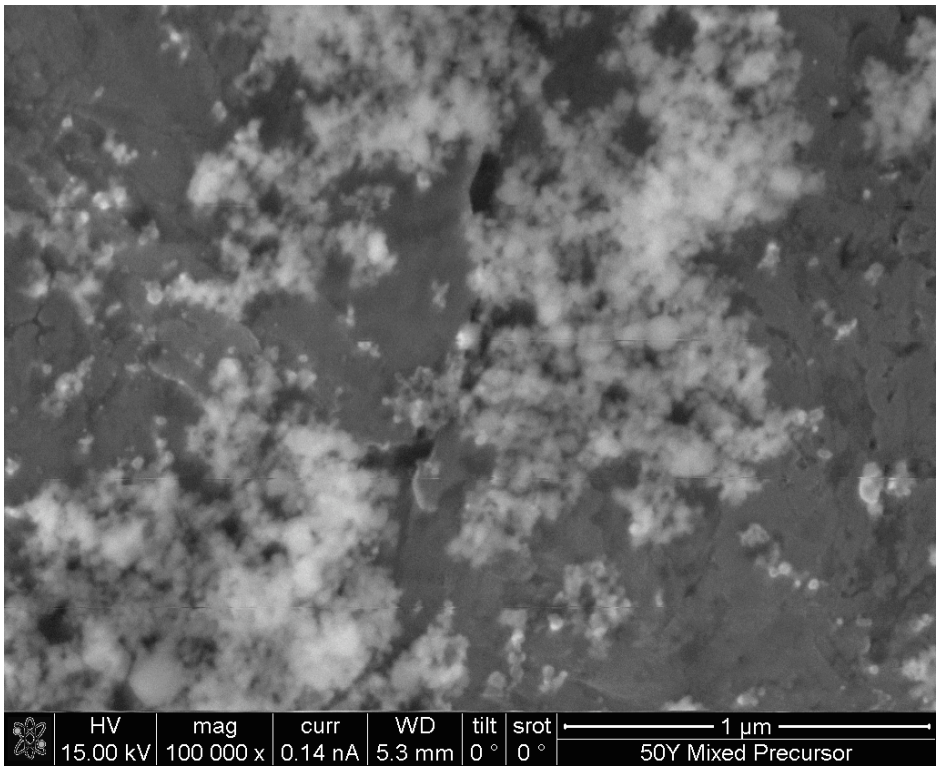

Figure 6-10. SEM image of 50Y mixed precursor sample

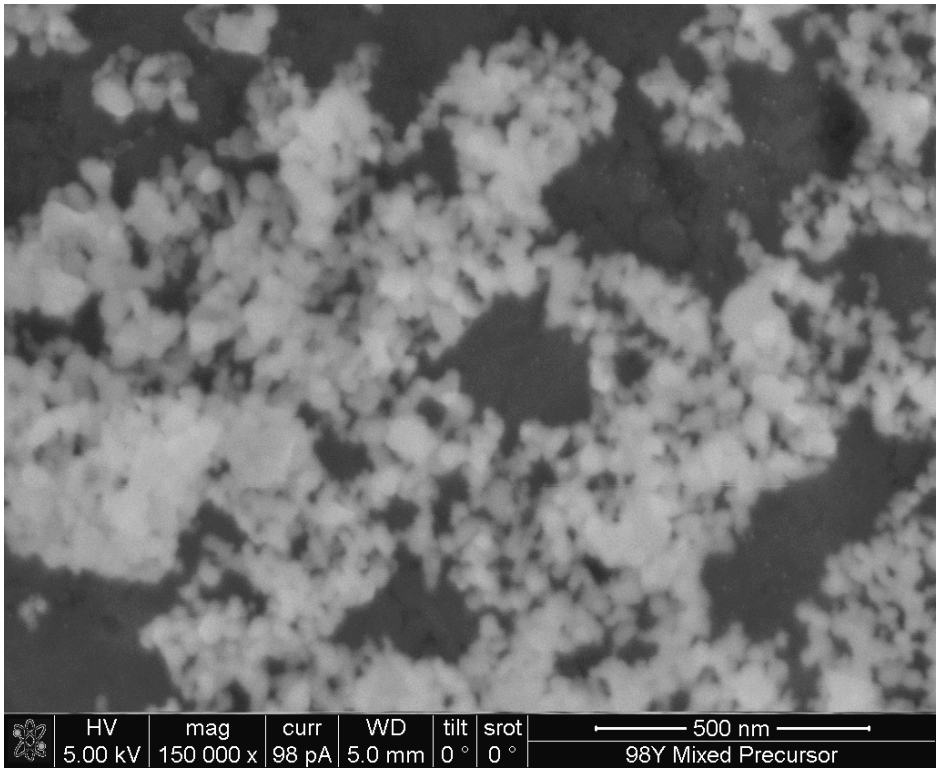

Figure 6-11. SEM image of 98Y mixed precursor sample

6.5.1.4. Fourier transform infrared spectroscopy

Diffuse reflectance infrared Fourier transform spectra (DRIFTS) for the ball-milled samples are presented in Figure 6-12 while the spectra corresponding to the mixed precursor samples are shown in Figure 6-13. The spectra above 1200 cm^{-1} were normalized and expanded in the full spectral range so that a fair comparison can be made between the two different sets. All spectra have three regions of interest 3900 to 2700 cm^{-1}, 1700 to 1300 cm^{-1} and 750 to 400 cm^{-1}.

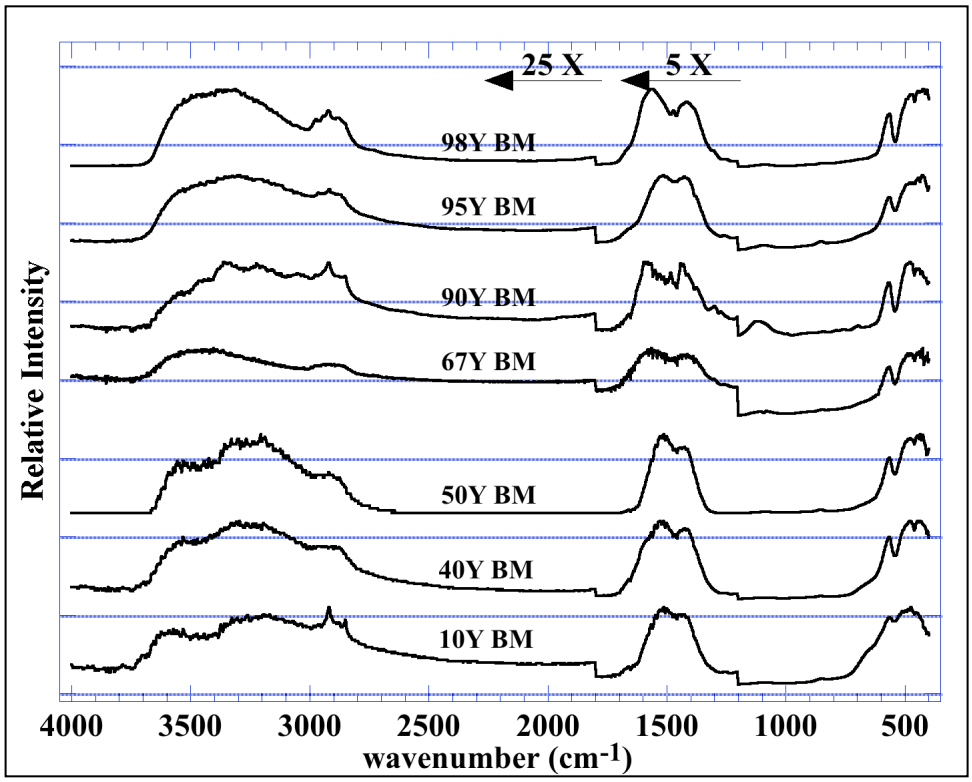

Figure 6-12. DRIFT spectra for all the ball-milled samples

All of the materials exhibit weak νOH absorptions in the first region, (3700 to 3000 cm^{-1}) attributable to surface hydroxyls arising from both physi- and chemi-sorbed water typical for LF-FSP nanopowders.

These hydroxyl bands are associated with the 1–4 % mass losses seen at ≤ 400 °C in the TGA studies below. The 2900–2700 cm^{-1} vibrations on some of the ball-milled samples are attributed to organic species (νC-H vibrations). The 98, 90 and 10 mol % Y_2O_3 ball-milled samples show the most organic species, contamination likely from the milling media. The 40 mol % Y_2O_3 mixed precursor sample also shows some organic species attributed to contamination from the collection process.

The second region of interest, 1700 to 1300 cm^{-1} contains peaks attributable to surface carbonates.[51,52] There are two clearly observed broad bands on centered at 1530 and 1400 cm^{-1} for the Y_2O_3 rich materials and 1502 and 1425 cm^{-1} for the MgO rich materials. The carbonate is present as a monodentate species bound to a metal surface atom.[53] The differences in the peak positions arises from the different metal sites in the oxides' crystal structure, MgO has only one site for the Mg atom, while Y_2O_3 has two distinct sites for yttrium.[54,55]

The carbonates species are much more prominent in the ball-milled materials, corroborated by TGA studies (see below). These carbonate species interact with surface basic centers which are enhanced in magnesia by the addition of lanthanide elements.[56]

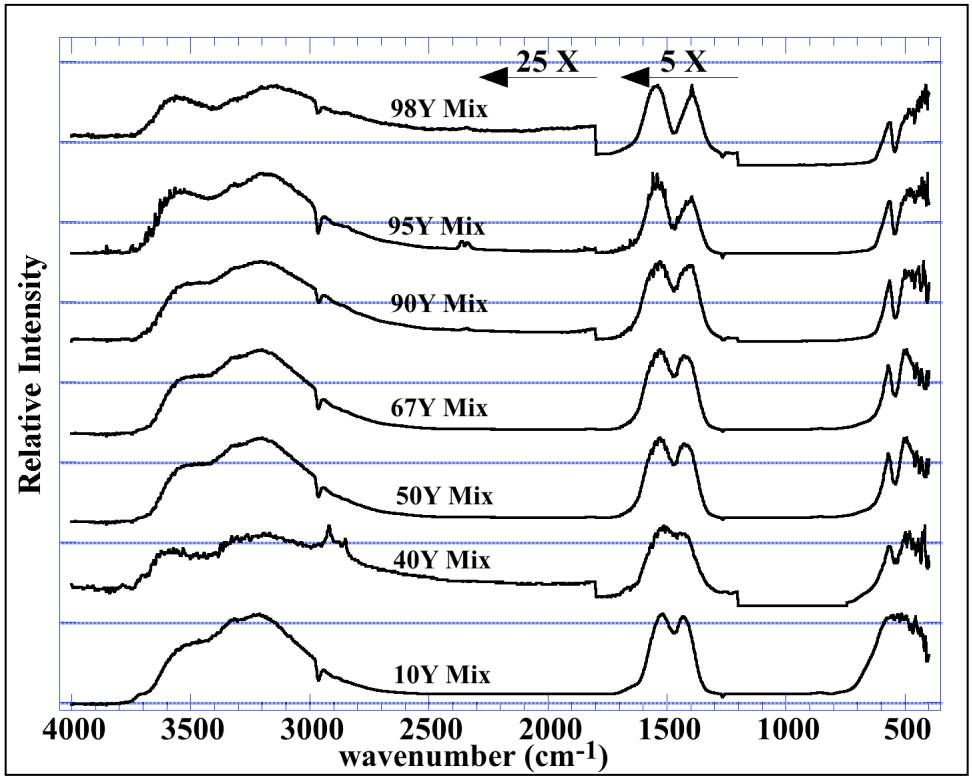

Figure 6-13. DRIFT spectra for all mixed precursor samples

The last region is where typical νM-O bands are observed, between 1000 – 400 cm^{-1}. The Y_2O_3 rich materials exhibit a characteristic sharp peak at 574 cm^{-1} from the symmetric Y-O octahedral vibrations and a broad band that spans the rest of the lower wavenumber region.[57,58] With an increase in MgO content, the characteristic Y_2O_3 spectrum gives rise to a very broad band characteristic of MgO. This broad band centered around 440 cm^{-1} arises from the Mg-O vibrational mode of symmetric MgO_6 octahedra.[59,60]

6.5.1.5. Thermal gravimetric analyses

TGAs were performed on all ball-milled samples and mixed precursor samples to determine their thermal behavior and relative amounts of adsorbed surface species (H_2O and CO_3^{2-}). All samples exhibit initial 1-4 wt % mass losses, typical for nanopowders produced via LF-FSP. Figure 6-14 presents the TGA traces for all ball-milled samples and also for pure Y_2O_3 and MgO.

All of the samples, regardless of their processing route show the characteristic loss of water (up to 225 °C) from the combustion process. All of the materials then continue to lose another up to 10 wt. % which is ascribed to the carbonate species present in these samples.

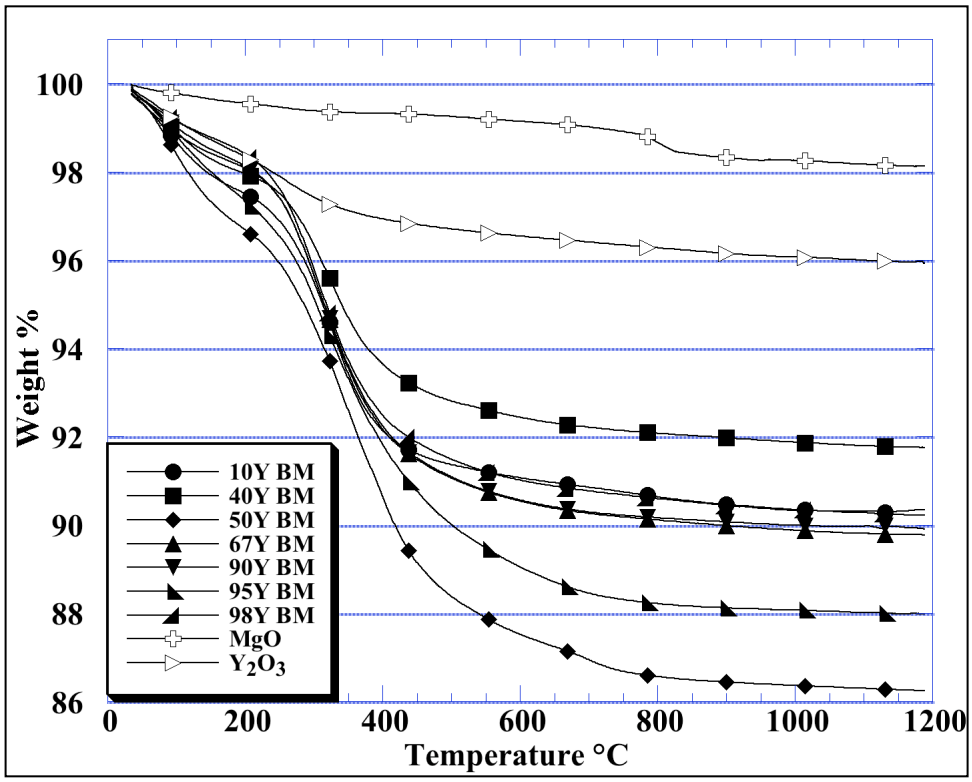

Figure 6-14. TGA traces of all ball-milled samples

The ball-milled materials differ substantially from the mixed precursor ones in the second mass loss event. The relative amount of carbonate species is substantially different for the two sets of materials. The ball-milled samples lose between 5 and 10 wt. %, which is not typical of any LF-FSP made nanopowders. The most likely source for this unexpected result is that ball milling modifies the surfaces of the nanopowders making it more reactive, thus promoting adsorption of the carbonate species.

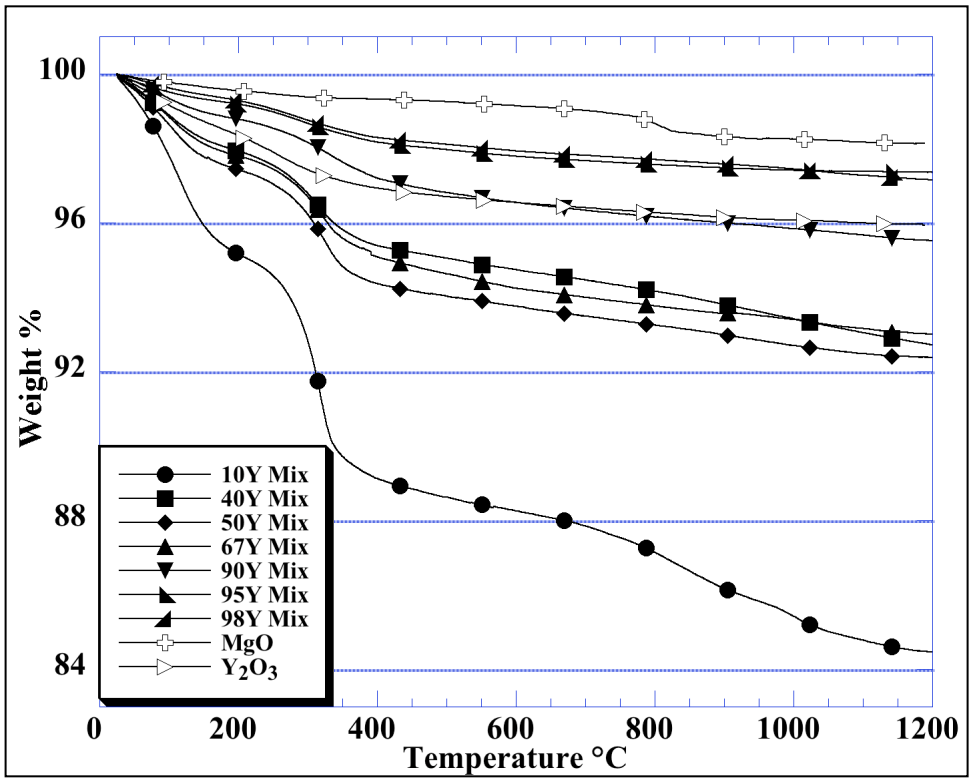

Figure 6-15. TGA traces of all as-produced mixed precursor samples

As seen in Figure 6-15, the mixed precursor materials after the typical 1–4 wt. % water loses lose only 3 wt. % more from carbonates. The obvious exception is for the 10Y sample, which loses another 9 wt. %. The reason behind this much larger loss is two-fold, this sample has the most amount of MgO and the highest surface area of any sample, and therefore the surface is the more reactive, adsorbing the most carbonate.

6.5.1.6. Dilatometry studies

Constant heating rate experiments for all samples were done in air and vacuum at three different heating rates: 2, 5 and 10 °C/min. The experiments done in air had a maximum temperature of 1600 °C, while those run in vacuum

1450 °C to prevent sagging of the alumina furnace tube. Figure 6-16 is a series of representative curves generated from the dilatometry studies of all samples.

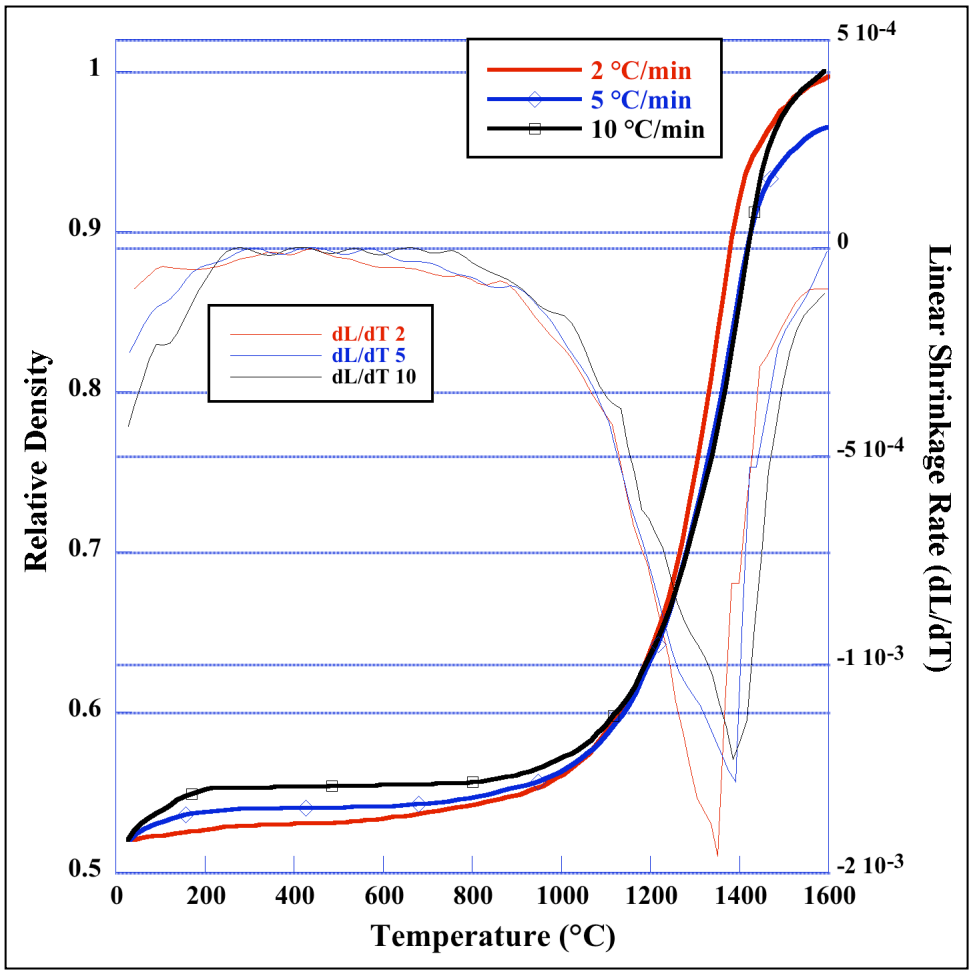

Figure 6-16. Representative dilatometry curve, showing different heating rates and shrinkage rate curves

The temperature of maximum shrinkage rate is very important in densification mechanics because it is indicative of a change between stage II and III of sintering.[61] In stage III, most grain growth occurs, while in stage II there grain coarsening and some pore annihilation are the dominant events. Figure 6-17 presents the relative densities at maximum shrinkage rate of all samples, as expected the densities for all samples are between 69 and 82 % of

theoretical. The data does not suggest any correlation between composition and density, nor does the sintering atmosphere affect densities at maximum rate of shrinkage. The green density of the samples does not affect the amount of densification nor the highest density at maximum shrinkage rate.

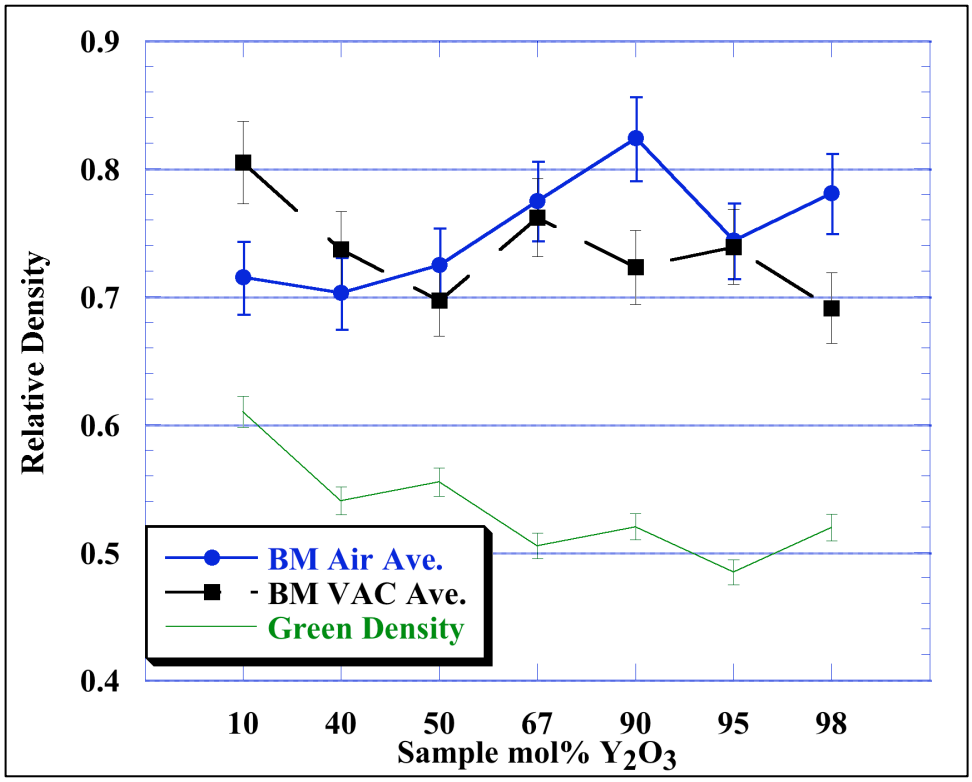

Figure 6-17. Relative density of all samples at maximum shrinkage rate

The choice of atmosphere (or lack thereof) can lower the by ≤ 80 °C the temperature at which the maximum shrinkage rate is observed, seen in Figure 6-18. The figure also shows that ball milling decreases the temperatures of maximum shrinkage between 20 and 40 °C. This result is expected because the more reactive particle surfaces from ball-milling as evidenced by FTIR and TGA, lower the required energy needed for particle reorganization and repacking.

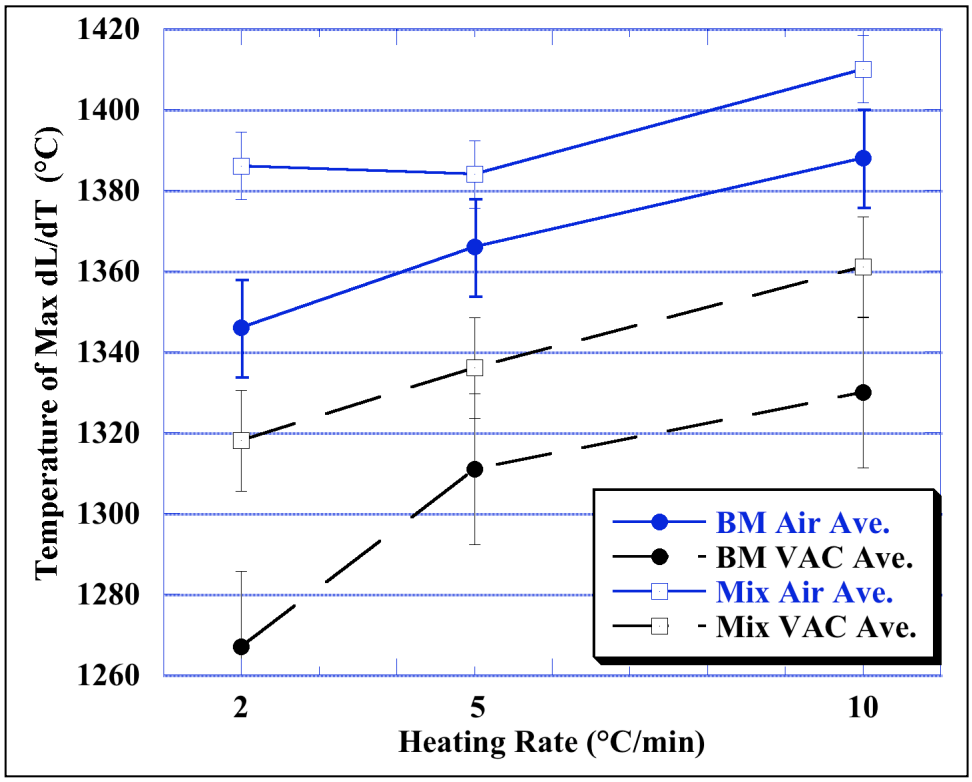

Figure 6-18. Heating rate and atmosphere effect on temperature of maximum linear shrinkage

The data points presented on the figure are the average of all the values for that particular rate at the given conditions. The overall trends observed show that vacuum and ball milling lower the maximum temperature needed to achieve the highest shrinkage rate for any sample.

6.6. Conclusions

This chapter demonstrates the use of LF-FSP to produce a series of mixed phase nanopowders in the MgO-Y_2O_3 phase space. This chapter compared the resulting materials form two distinct routes: traditional ball milling of parent oxides and a mixed precursor route. All of the precursors used to make these nanopowders were readily synthesized from inexpensive starting materials.

Ball milling modifies the surface causing it to interact more easily with atmospheric moisture and carbonates. This increased activity of the nanopowders surfaces has led to much higher adsorption of surface species as evidenced by FTIR studies, and confirmed by TGA losses. The SSAs of these materials also are affected although a clear trend was not established. The mixed precursor route showed that bi-phasic materials are possible via LF-FSP, but some unexpected phases may form if the kinetics of the particular system are not fully understood. From the dilatometric study, ball milling lowers the temperatures of maximum shrinkage rate on average by 25 °C, and vacuum has the largest effect on lowering the temperature of maximum shrinkage rate by up to 80 °C. Finally the two routes contrasted here; ball milling and mixed precursor synthesis, provide access to similar materials but have some distinctions with regards to surface chemistries, bulk morphologies and densification temperatures.

6.7. Bibliography

1. A. Kaminskii "Modern Developments in the Physics of Crystalline Laser Materials," *Phys. Status Solidi A,* 200 [2] 215-296 (2003).
2. M. J. Mayo "Processing of Nanocrystalline Ceramics From Ultrafine Particles," *Int. Mater. Rev.,* 41 [3] 85-115 (1996).
3. T. Ikegami, J.-G. Li, T. Mori, Y. Moriyoshi "Fabrication of Transparent Yttria Ceramics by the Low-Temperature Synthesis of Yttrium Hydroxide," *J. Am. Ceram. Soc.,* 85 [7] 1725-1729 (2002).
4. K.-I. Shibata, H. Nakamura, A. Fujii "Nondoped Y_2O_3 for 3-5 μm IP Transmission," *Window and Dome Technologies and Materials II Proc. SPIE,* 1326(1) [1] 48-53 (1990).
5. R. H. Au "Optical Window Systems," *Window and Dome Technologies and Materials II Porc. SPIE,* 1326(1) [1] 243-253 (1990).
6. R. M. Sova, M. J. Linevsky, M. E. Thomas, F. F. Mark "High-Temperature Optical Properties of Oxide Dome Materials," *Window and Dome Technologies and Materials III Proc. SPIE,* 1760(1) [1] 27-40 (1992).
7. D. C. Harris "History of Development of Polycrystalline Optical Spinel in the U.S," *Window and Dome Technologies and Materials IX Proc. SPIE,* 5786(1) [1] 1-22 (2005).
8. J. M. Wahl, T. M. Hartnett, L. M. Goldman, R. Twedt, C. Warner "Recent Advances in AlON Optical Ceramic," *Window and Dome Technologies and Materials IX Proc. SPIE,* 5786(1) [1] 71-82 (2005).
9. G. C. Wei, A. Hecker, W. H. Rhodes "Scattering in Lanthana-Strengthened-Yttria Infrared Transmitting Material," *Window and Dome Technologies and Materials III Proc. SPIE,* 1760(1) [1] 14-26 (1992).
10. D. C. Harris "Frontiers in Infrared Window and Dome Materials," *Infrared Technology XXI Proc. SPIE,* 2552(1) [1] 325-335 (1995).
11. Krell, J. Klimke, T. Hutzler "Advanced Spinel and Sub-μm Al_2O_3 for Transparent Armour Applications," *J. Eur. Ceram. Soc.,* 29 [2] 275-281 (2009).
12. M. P. Harmer, H. M. Chan, G. A. Miller "Unique Opportunities for Microstructural Engineering With Duplex and Laminar Ceramic Composites," *J. Am. Ceram. Soc.,* 75 [7] 1715-1728 (1992).
13. T. Suzuki, K. Itatani, M. Aizawa, F. S. Howell, A. Kishioka "Sinterability of Spinel ($MgAl_2O4$)-Zirconia Composite Powder Prepared by Double Nozzle Ultrasonic Spray Pyrolysis," *J. Eur. Ceram. Soc.,* 16 [11] 1171-1178 (1996).
14. E. J. Coad, J. E. Field "Liquid Impact Resistance of CVD Diamond and Other Infrared Materials," *Window and Dome Technologies and Materials V Proc. SPIE,* 3060(1) [1] 169-180 (1997).
15. M. Sternitzke "Structural Ceramic Nanocomposites," *J. Eur. Ceram. Soc.,* 17 [9] 1061-1082 (1997).
16. Sawaguchi, K. Toda, K. Niihara "Mechanical and Electrical Properties of Al_2O_3/SiC Nano-Composites," *Nippon Seram. Kyo. Gak.,* 99 [6] 523-526 (1991).

17. J. D. French, J. Zhao, M. P. Harmer, H. M. Chan, G. A. Miller "Creep of Duplex Microstructures," *J. Am. Ceram. Soc.,* 77 [11] 2857-2865 (1994).
18. Z. Zhao, L. Zhang, J. Zheng, H. Bai, S. Zhang, B. Xu "Microstructures and Mechanical Properties of $Al_2O_3/ZrO2$ Composite Produced by Combustion Synthesis," *Scripta Mater.,* 53 [8] 995-1000 (2005).
19. N. Padture, B. R. Lawn "Contact Fatigue of a Silicon Carbide With a Heterogeneous Grain Structure," *J. Am. Ceram. Soc.,* 78 [6] 1431-1438 (1995).
20. M. J. Mayo, D. C. Hague, D. J. Chen "Processing Nanocrystallin Ceramics for Applicaitons in Superplasticity," *Mater. Sci. Eng. A,* 166 [1-2] 145-159 (1993).
21. H. Kear, J. Colaizzi, W. E. Mayo, S. C. Liao "On the Processing of Nanocrystalline and Nanocomposite Ceramics," *Scripta Mater.,* 44 [8-9] 2065-2068 (2001).
22. X. Z. Zhou, V. Shukla, W. R. Cannon, B. H. Kear "Metastable Phase Formation in Plasma-sprayed ZrO_2 (Y_2O_3)-Al_2O_3," *J. Am. Ceram. Soc.,* 86 [8] 1415-1420 (2003).
23. B.-K. Jang "Microstructure of Nano SiC Dispersed Al_2O_3-ZrO_2 Composites," *Mater. Chem. Phys.,* 93 [2-3] 337-341 (2005).
24. G.-D. Zhan, J. Kuntz, J. Wan, J. Garay, A. K. Mukherjee "A Novel Processing Route to Develop a Dense Nanocrystalline Alumina Matrix (<100 nm) Nanocomposite Material," *J. Am. Ceram. Soc.,* 86 [1] 200–202 (2002).
25. S. Bhaduri, S. B. Bhaduri "Enhanced Low Temperature Toughness of Al_2O_3-ZrO_2 Nano/Nano Composites," *Nanostruct. Mater.,* 8 [6] 755-763 (1997).
26. H. Kear, Z. Kalman, R. K. Sadangi, G. Skandan, J. Colaizzi, W. E. Mayo "Plasma-sprayed Nanostructured Al_2O_3/TiO_2 Powders and Coatings," *J. Therm. Spray Techn.,* 9 [4] 483-487 (2000).
27. H. Z. Wang, L. Gao, J. K. Guo "Fabrication and Microstructure of Al_2O_3-ZrO_2(3Y)-SiC Nanocomposites," *J. Eur. Ceram. Soc.,* 19 2125-2131 (1999).
28. S. Bhaduri, S. B. Bhaduri, E. Zhou "Auto Ignition Synthesis and Consolidation of Al_2O_3–ZrO_2 Nano/Nano Composite Powders," *J. Mater. Res.,* 13 [1] 156-165 (1998).
29. R. G. Duan, G. D. Zhan, J. D. Kuntz, B. H. Kear, A. K. Mukherjee "Processing and Microstructure of High-Pressure Consolidated Ceramic Nanocomposites," *Scripta Mater.,* 51 [12] 1135-1139 (2004).
30. M. Liu, H. Li, L. Xiao, W. Yu, Y. Lu, Z. Zhao, G. A. Miller "XRD and Mössbauer Spectroscopy Investigation of Fe_2O_3-Al_2O_3 Nano-composite," *J. Magn. Magn. Mater.,* 294 [3] 294-297 (2005).
31. H. Kear, R. Sadangi, V. Shukla, T. Stefanik, R. Gentilman "Submicron-Grained Transparent Yttria Composites," *Window and Dome Technologies and Materials IX Proc. SPIE,* 5786(1) [1] 227-233 (2005).
32. T. Stefanik, R. Gentilman, P. Hogan "Nanocomposite Optical Ceramics for Infrared Windows and Domes," *Window and Dome Technologies and Materials X Proc. SPIE,* 6545(1) [1] 65450A-654505 (2007).
33. M. Kim, T. R. Hinklin, R. M. Laine "Core-Shell Nanostructure Nanopowders Along $(CeOx)_x(Al_2O_3)_{1-x}$ Tie-Line by Liquid-Feed Flame Spray Pyrolysis (LF-FSP)," *Chem. Mater.,* 20 [16] 5154-5162 (2008).

34. K. Itatani, T. Tsujimoto, A. Kishimoto "Thermal and Optical Properties of Transparent Magnesium Oxide Ceramics Fabricated by Post Hot-Isostatic Pressing," *J. Eur. Ceram. Soc.,* 26 [4-5] 639-645 (2006).
35. H. Eilers "Synthesis and Consolidation of Nanophase Yttria (Y_2O_3)," *Window and Dome Technologies and Materials IX Proc. SPIE,* 5786(1) [1] 234-241 (2005).
36. B. Willingham, J. M. Wahl, P. K. Hogan, L. C. Kupferberg, T. Y. Wong, D. A. M. "Densification of Nano-Yttria Powders for IR Window Applications," *Window and Dome Technologies VIII Proc. SPIE,* 5078(1) [1] 179-188 (2003).
37. F. Dericioglu, Y. Kagawa "Effect of Grain Boundary Microcracking on the Light Transmittance of Sintered Transparent $MgAl_2O_4$," *J. Eur. Ceram. Soc.,* 23 [6] 951-959 (2003).
38. R. Raj "Fundamental Research in Structural Ceramics for Service Near 2000°C," *J. Am. Ceram. Soc.,* 76 [9] 2147-2174 (1993).
39. P. Greil "Advanced Engineering Ceramics," *Adv. Mater.,* 14 [10] 709-716 (2002).
40. Y. Du, Z. Jin "Thermodynamic Assessment of the $YO_{1.5}$-MgO System," *J. Alloys Compd.,* 176 [1] L1-L4 (1991).
41. L. B. Kong, J. Ma, H. Huang "Low Temperature Formation of Yttrium Aluminum Garnet From Oxides via a High-energy Ball Milling Process," *Mater. Lett.,* 56 [3] 344-348 (2002).
42. Z. Zhihui, L. I. Nan "Influence of Mechanical Activation of Al_2O_3 on Synthesis of Magnesium Aluminate Spinel," *Sci. Sinter.,* 32 (2) [2] 73-79 (2004).
43. Q. Johnson, R. S. Zhou "Cheking and Estimating RIR Values," *Adv. X-Ray Anal.,* 42 287-296 (2000).
44. Camenzind, R. Strobel, S. E. Pratsinis "Cubic Or Monoclinic Y_2O_3:Eu^{3+} Nanoparticles by One Step Flame Spray Pyrolysis," *Chem. Phys. Lett.,* 415 [4-6] 193-197 (2005).
45. H. Chang, I. W. Lenggoro, K. Okuyama, T.-O. Kim "Continuous Single-Step Fabrication of Nonaggregated, Size-controlled and Cubic Nanocrystalline Y_2O:Eu^{3+} Phosphors Using Flame Spray Pyrolysis," *Jpn. J. Appl. Phys.,* 43 [6A] 3535-3539 (2004).
46. Y. C. Kang, D. J. Seo, S. B. Park, H. D. Park "Morphological and Optical Characteristics of Y_2O_3:Eu Phosphor Particles Prepared by Flame Spray Pyrolysis," *Jpn. J. Appl. Phys.,* 40 [6A] 4083-4086 (2001).
47. P. Zhang, A. Navrotsky, B. Guo, I. Kennedy, A. N. Clark, C. Lesher, Q. Liu "Energetics of Cubic and Monoclinic Yttrium Oxide Polymorphs: Phase Transitions, Surface Enthalpies, and Stability at the Nanoscale," *J. Phys. Chem. C,* 112 [4] 932-938 (2008).
48. S. Ivanova, B. L. Moroz, E. M. Moroz, Y. Larichev, E. A. Paukshtis, V. I. Bukhtiyarov "New Binary Systems Mg-M-O (M=Y, La, Ce): Synthesis and Physico-Chemical Characterization," *J. Solid State Chem.,* 178 [11] 3265-3274 (2005).
49. Ruckenstein, A. Z. Khan "Effects of Superbasic Catalysts Prepared by Promoting MgO with Bialkali Metal Compounds on the Oxidative Coupling of Methane," *J. Catal.,* 141 [2] 628-647 (1993).

50. H. Vinek, H. Noller, M. Ebel, K. Schwarz "X-Ray Photoelectron Spectroscopy and Heterogeneous Catalysis, with Elimination Reactions as an Example," *J. Chem. Soc. Fara. T. 1,* 73 734-746 (1977).
51. A. Davydov, M. L. Shepotko, A. A. Budneva "Basic Sites on the Oxide Surfaces: Their Effect on the Catalytic Methane Coupling," *Catal. Today,* 24 [3] 225-230 (1995).
52. J. V. Evans, T. L. Whateley "Infra-Red Study of Adsorption of Carbon Dioxide and Water on Magnesium Oxide," *T. Faraday Soc.,* 63 2769-2777 (1967).
53. C. Traina, J. Schwartz "Surface Modification of Y_2O_3 Nanoparticles," *Langmuir,* 23 [18] 9158-9161 (2007).
54. S. Sasaki, K. Fujino, Y. Takeguchi "X-Ray Determination of Electron-Density Distributions in Oxides, MgO, MnO, CoO, and NiO, and Atomic Scattering Factors of Their Constituent Atoms," *Proc. Jpn. Acad., Ser. B.,* 55 [2] 43-48 (1979).
55. Santos, K. Strecker, P. A. Suzuki, S. Kycia, O. M. M. Silva, C. R. M. Silva "Stabilization of α-SiAlONs Using a Rare-Earth Mixed Oxide ($RE_2O_{3)}$ As Sintering Additive," *Mater. Res. Bull.,* 40 [7] 1094-1103 (2005).
56. P. Thomasson, O. S. Tyagi, H. Knözinger "Characterisation of the Basicity of Modified MgO-Catalysts," *Appl. Catal., A,* 181 [1] 181-188 (1999).
57. S. Kinugasa, K. Tanabe, T. Tamura "Spectral Database for Organic Compounds # 40494," National Institure of Advanced Industiral Technologies, 2008.
58. K. A. Wikersheim, R. A. Lefevrer "Infrared Transmittance of Crystalline Yttrium Oxide and Related Compounds," *J. Opt. Soc. Am.,* 51 [10] 1147–1148 (1961).
59. Gu, C. Li, H. Cao, W. Shao, Y. Hu, J. Chen, A. Chen "Crystallinity of Li-Doped MgO:Dy^{3+} Nanocrystals via Combustion Process and Their Photoluminescence Properties," *J. Alloys Compd.,* 453 [1-2] 361-365 (2008).
60. T. López, R. Gómez, J. Navarrete, E. López-Salinas "Evidence for Lewis and Brosted Acid Sites on MgO Obtained by Sol-Gel," *J. Sol-Gel Sci. Techn.,* 13 [1] 1043-1047 (1998).
61. P.-L. Chen, I.-W. Chen "Sintering of Fine Oxide Powders: II, Sintering Mechanisms," *J. Am. Ceram. Soc.,* 80 [3] 637-645 (1997).

Chapter 7.

General Conclusions and Future Work

7.1. Introduction

The intention of the last chapter of this dissertation is to be able to draw general conclusions about liquid-feed flame spray pyrolysis (LF-FSP) as currently practiced by the Laine group. The general conclusions encompass a larger scope than those drawn at the end of the individual chapters, and tie together the general theme of the dissertation. It closes with some suggestions for further developing and understand LF-FSP processing and some future directions research with LF-FSP might go.

7.2. Conclusions

The work presented here demonstrates the versatility of liquid-feed flame spray pyrolysis to produce oxide nanoparticles in essentially any mixed metal system. The ceramic oxides produced by LF-FSP can be used in several catalytic, photonic, structural, electrical and biomedical applications. In addition LF-FSP has proved a valuable combinatorial synthesis technique for mixed metal oxide nanopowders, and it imparts exceptional control of stoichiometry and phase purity for any chosen oxide nanopowder system. Because LF-FSP offers rapid quenching of the combustion species, it provides access to new, kinetic materials not accessible by any other conventional processing method.

Chapter 3 established the ability of LF-FSP to access kinetic metastable phase materials with the observation spinel phase at a composition of $(NiO)_{0.22}(Al_2O_3)_{0.78}$ which

lies far outside the currently accepted phase diagram for this system. The stability of this unexpected phase proved to be remarkable as it survived heating in air to 1400 °C for 12h with minimal particle coarsening. These robust nanopowders may prove to be instrumental in developing general methods of preparing high surface area sinter-resistant catalysts. It is a well known fact that spinel materials have much higher T_m than its constitutive end members, therefore the observed resistance to sintering comes mainly from the spinel structure which is now accessible at stoichiometries more favorable to catalytic activity.

In Chapter 4, a systematic approach to a series of nine nanopowders along the CoO_x-Al_2O_3 tie-line is presented. Here one of the advantages of LF-FSP over other synthesis techniques is presented; it allows production of up to 15 different compositions (50g samples) in the time span of a single week. The versatility of LF-FSP to allow such a rapid tailoring of compositions provides valuable access to a very wide range of materials. The formations of off-stoichiometric spinels (21 and 37 mol % Co samples) again corroborate the findings of the previous chapter. LF-FSP provides access to kinetic phases due to the extremely fast quench rates, rather than the thermodynamically favored ones. The formation of Co_3O_4 instead of CoO allows elucidation on the influence of oxygen partial pressures on the oxidation state of the resulting metal oxides. It is speculated that excess oxygen favors the formation of Co^{3+} which in turn, favors the formation of a spinel ($Co^{2+}{}_1Co^{3+}{}_2O_4$) structure that is detected.

The work of Chapter 5 shows the ease with which a large number of completely different powders can be synthesized in a relatively short period of time, building on the above premise of rapidly tailor-able compositions, the work is expanded to include three

completely different oxide systems. The work reports on the systematic synthesis of three bimetallic transition metal systems, nanopowder series along the NiO-Co_3O_4, NiO-MoO_3, and NiO-CuO tie lines. There is some evidence to suggest that the partial pressures of all species involved in the synthesis process have an effect on the resulting materials. As seen previously the partial pressure of O_2 affects the formation of particular oxide phases. The higher vapor pressures of the transition metal ions studied in this chapter cause larger particles leading to the lower SSA observed, conversely the relatively low vapor pressure of Mo^{3+} leads to observed preferential growth of certain crystallographic planes in the NiO-MoO_3 system. Chapter 6 shows the ability of LF-FSP to produce bi-phase materials with intended stoichiometries.

7.3. Future work

7.3.1. LF-FSP Processing

LF-FSP is a highly dynamic process to make oxide nanopowders with many variables that allow the development of unique and novel compositions, crystal structures and morphologies. However there are some difficulties associated with understanding the inherent kinetics of the particular oxide system, limiting the certainty of expected results.

The current level of understanding of the parameters in the LF-FSP apparatus and general particle formation process needs to be expanded, to truly gain control of the resulting materials and a definite understanding of particle evolution. Specifically, a parametric study on the gas flow characteristics of the inlet and exhaust system needs to be conducted so that a better understanding of the overall particle paths and residence times is obtained. Further modification of the apparatus with regards to a

more suitable metering and material monitoring system is indispensible to generate a reliable data bank of parameters. A detailed study on the flame dynamics of the LF-FSP system would provide valuable insight into particle nucleation and growth; it would also complete the overall flow dynamics of the system.

7.3.2. General Directions

The vast possibility of materials that can be synthesized by LF-FSP make suggesting a definite future work a daunting task. The two areas of highest impact for scientific and technological advance would be: catalytic, and optical/transparent applications. The relatively high surface areas and resistance to sintering of LF-FSP produced nanoparticles makes them ideal candidates for catalytic applications. Recent work by the group, in collaboration with the Maier group in Saarbrucken, suggests that some of our nanopowders can be as efficient as noble metal based catalyst. Therefore, exploratory work in other catalytic fields, such as fuel-cell and de-NOx applications is warranted. Relatively high activity in both of these areas has already been shown using $NiO:(CeZr)O_2$ and $BaO:Al_2O_3$ nanopowders.

Having successfully produced bi-phase materials further studies on sintering and densification should be undertaken to achieve structural transparent ceramics. Continued nanograined ceramic development using LF-FSP produced materials, particularly Y_2O_3–MgO, should yield a reproducible route to optically transparent materials. Achieving the ideal transparent ceramic (laser quality) although plausible is really not a feasible goal with the current facilities. The LF-FSP apparatus does not lend itself to producing the extremely demanding purities necessary to achieve such materials. Effort should be put forth towards developing other more complex bi-phase

material, such as $MgAl_2O_4$–YAG nano-nano composites, as in increase in any of their mechanical properties would be technologically significant.